Tampere University

SHUBIN MA

Far-Field Backscattering Brain Implant Communications

Antenna Design Methodologies and Performance Validation

Tampere University Dissertations 367

Tampere University Dissertations 367

SHUBIN MA

Far-Field Backscattering Brain Implant Communications

Antenna Design Methodologies and Performance Validation

ACADEMIC DISSERTATION
To be presented, with the permission of
the Faculty of Medicine and Health Technology
of Tampere University,
for online public discussion
on 29 January 2021, at 12 o'clock.

ACADEMIC DISSERTATION
Tampere University, Faculty of Medicine and Health Technology
Finland

Responsible supervisor and Custos	Professor Leena Ukkonen Tampere University Finland	
Supervisor	Dr. Toni Björninen Tampere University Finland	
Pre-examiners	Professor Heli Jantunen University of Oulu Finland	Professor Asimina Kiourti The Ohio State University United States of America
Opponent	Professor Hendrik Rogier Ghent University Belgium	

The originality of this thesis has been checked using the Turnitin Originality Check service.

Cover design: Roihu Inc.

ISBN 978-952-03-1829-1 (print)
ISBN 978-952-03-1830-7 (pdf)
ISSN 2489-9860 (print)
ISSN 2490-0028 (pdf)
http://urn.fi/URN:ISBN:978-952-03-1830-7

PunaMusta Oy – Yliopistopaino
Joensuu 2021

To my parents

献给罗舫与马继新

ACKNOWLEDGEMENTS

This thesis is the output of the research conducted in the Wireless Identification and Sensing Systems Lab. First and foremost, I wish to express my deepest gratitude to my supervisor Professor **Leena Ukkonen** for funding my research and inspiring and guiding my way through this PhD journey. I am also greatly indebted to my instructor Dr. **Toni Björninen** for his persistent guidance and encouragement, which made me go further professionally in my academic career.

During my doctoral study, I am profoundly grateful for having been supported by **Tampere University** for the oversea visiting research. Many thanks to my supervisor and Professor **Jan M. Rabaey** for providing me with this valuable opportunity. Special thanks to Dr. **George Alexandrov** and Dr. **Arno Thielens** for the inspiring discussions in Berkeley. My gratitude also goes to **Annukka Viitanen** and **Candy Corpus** for facilitating my transition during that time.

I must also thank Professor **Merja H. Voutilainen** for her expertise in neuroscience. Our in-vivo test could not have been accomplished without her support.

Thanks should also go to **Nokia Foundation**. It is a huge encouragement to have my work to be recognized and rewarded.

I would also like to extend my gratitude to my lovely friends: **Chen Yu**, **Shahbaz Ahmed**, **Nikta Pournoori** for the joyful time spent together during my PhD.

Lastly, I wish to express my deepest gratitude to my parents for always being there for me. I could not have accomplished this journey without their constant support and unconditional love.

ABSTRACT

The recent progress in wireless technology has prompted the development of wireless implantable and wearable systems to realize the envisioned bio-telemetry where the patients can access to diagnosis and treatment at any time, any location and with any amount of monitoring and diagnostic data. Especially in brain care applications, wireless intracranial implantable microsystems are believed to open a new paradigm for the management of brain disorders and the treatment of neurological diseases.

Planning the transcranial wireless link between the implant and the external devices is a challenging task that requires multidisciplinary considerations. The fundamental challenge is the attainment of miniature implantable antennas achieving adequately high efficiency for signaling and wireless power transfer in the presence of the dissipative intracranial tissues. Moreover, in the antenna development, accurate modeling of the human tissue environment is of great importance to characterize the antenna performance and to evaluate the tissue interaction with the electromagnetic radiation. Importantly, for the sake of the patient's safety and comfort, extra-low power consumption with a batteryless operation of the implant is highly appealed to minimize the biological intrusiveness and to ensure a long-term operation. For this reason, radio frequency identification (RFID) technique, which is based on the extra low-power and low-complexity backscatter communications, has been recently considered as a promising wireless solution for the implants.

To address the above-mentioned challenges, this thesis starts with a discussion of the RFID based wireless sensing, numerical modeling of the intracranial tissue environment and the characteristics of antenna radiation in lossy tissue materials. During this discussion, an approach to enable the semi-passive operation of an RFID system without the assistance of external batteries is presented, and a guideline for efficient modeling of the human head for implantable antenna development is provided. Finally, a multimodal spatially distributed antenna and a miniature dual-split-ring antenna with tuneable impedance are introduced for far-field backscattering brain implants. The promising performance of the proposed antennas is analyzed and discussed with simulation, in-vitro measurement and in-vivo experiment.

CONTENTS

ACRONYMS

ADC	Analog to Digital Converter
AR	Axial Ratio
BCI	Brain Computer Interface
BEM	Boundary Element Method
CAD	Computer-Aided Design
CEM	Computational Electromagnetics
CP	Circular Polarization
CSF	Cerebrospinal Fluid
EM	Electromagnetic
EMC	Electromagnetic Compatibility
EPC	Electronic Product Code
EPDM	Ethylene Propylene Diene Monomer
FA	Frontal Anterior
FCC	Federal Communications Commission
FDTD	Finite-Difference Time Domain
FEM	Finite-Element Method
FP	Frontal Posterior
HFSS	High Frequency Structure Simulator
ICP	Intracranial Pressure
MoM	Method of Moments
MRI	Magnetic Resonance Imaging
PA	Parietal Anterior
PP	Parietal Posterior
RCS	Radar Cross Section
RFID	Radio Frequency Identification
SAR	Specific Absorption Rate
TID	Transponder ID
UHF	Ultra High Frequency
VHP	Visible Human Project

WBAN	Wireless Body Area Network
WSN	Wireless Sensor Network

ORIGINAL PUBLICATIONS

Publication I S. Ma, L. Sydänheimo, L. Ukkonen and T. Björninen, "Split-Ring Resonator Antenna System with Cortical Implant and Head-Worn Parts for Effective Far-Field Implant Communications," accepted in *IEEE Antennas and Wireless Propagation Letters*, vol. 17, no. 4, pp. 710-713, 2018.

Publication II S. Ma, T. Björninen, L. Sydänheimo, M. H. Voutilainen and L. Ukkonen, "Double Split Rings as Extremely Small and Tuneable Antennas for Brain Implantable Wireless Medical Microsystems," accepted in *IEEE Transactions on Antennas and Propagation*, 2020.

Publication III S. Ma, L. Sydänheimo, L. Ukkonen and T. Björninen, "Robustness Evaluation of Split Ring Resonator Antenna System for Wireless Brain Care in Semi-Anatomical Ellipsoid Head Model," accepted in *Journal of Applied Computational Electromagnetics Society ACES*, vol. 33, no. 9, 2018.

Publication IV S. Ma, L. Sydänheimo, L. Ukkonen and T. Björninen, "Inductively Coupled Split Ring Resonator as Small RFID Pressure Sensor for Biomedical Applications," *IEEE International Symposium on Antennas and Propagation (AP-S), Montréal, Québec,* Canada, 2020.

Publication V S. Ma, N. Pournoori, L. Sydänheimo, L. Ukkonen, T. Björninen and A. Georgiadis, "A Batteryless Semi-Passive RFID Sensor Platform," *IEEE International Conference on RFID Technology and Applications (RFID-TA)*, Pisa, Italy, 2019.

Publication VI S. Ma, L. Ukkonen, L. Sydänheimo and T. Björninen, "Comparison of Human Head Phantoms with Different Complexities for Implantable Antenna Development," *International Applied Computational Electromagnetics Society Symposium - China (ACES)*, Beijing, China, 2018.

Publication VII S. Ma, L. Ukkonen, L. Sydänheimo and T. Björninen, "Dual-Layer Circularly Polarized Split Ring Resonator Inspired Antenna for Wearable UHF RFID Tag," *IEEE International Symposium on Antennas and Propagation (AP-S)*, Boston, MA, USA, 2018.

AUTHOR CONTRIBUTIONS

Publication I — S. Ma conceived of the antenna design method, fabricated the antenna prototypes, and conducted the simulation and wireless measurement. S. Ma and T. Björninen wrote the manuscript. All authors provided critical feedback and helped shape the research.

Publication II — S. Ma conceived of the antenna design method, fabricated the antenna prototypes, and conducted the simulation. S. Ma, L. Ukkonen and M. H. Voutilainen carried out the measurement. S. Ma wrote the manuscript in consultation with T. Björninen. L. Ukkonen and L. Sydänheimo supervised the research.

Publication III — S. Ma conceived of the original idea and conducted the simulation. S. Ma and T. Björninen analyzed the results. S. Ma wrote the manuscript in consultation with T. Björninen. L. Ukkonen and L. Sydänheimo supervised the research.

Publication IV — S. Ma conceived of the sensor design method, fabricated the prototypes, and conducted the simulation and wireless measurement. S. Ma wrote the manuscript. T. Björninen supervised the research. All authors provided critical feedback and helped shape the manuscript.

Publication V — S. Ma conceived of the original idea. S. Ma and N. Pournoori fabricated the prototypes and conducted the simulation and wireless measurement. S. Ma wrote the manuscript. T. Björninen supervised the research. All authors provided critical feedback and helped shape the manuscript.

Publication VI — S. Ma and T. Björninen conceived of the original idea. S. Ma conducted the simulation and wrote the manuscript. T. Björninen supervised the research. All authors provided critical feedback and helped shape the research.

Publication VII — S. Ma conceived of the antenna design method, fabricated the antenna prototypes, and conducted the simulation and wireless measurement. S. Ma wrote the manuscript. T. Björninen supervised the research. All authors provided critical feedback and helped shape the manuscript.

1 INTRODUCTION

1.1 Brain Implant in Biomedical Applications

For ages, due to the seriously limited knowledge of the brain mechanisms, brain disorders and neurological diseases were considered formidable and intractable in clinical practice. This situation started to improve in the second half of the 20th century with the aid of the remarkable advances in chemistry, electronics, computer science and medical imaging. Consequently, not only the understanding of the brain and the nervous system became progressively comprehensive, effective treatments with brain implants were also successionally proposed for neurophysiological diseases. For instance, in the late 1970s, Professor Jacques Vidal put forward the concept of brain-computer interface (BCI) that aimed to interconnect the brain and the computer via bi-directional neural pathways [1]. This concept is believed to enable mind-control of prosthetics and assistive devices for the patients with a wide range of disabilities [2-3]. Nearly concurrently, neuroprosthetic devices with an implantable electrode array were invented to augment or substitute the damaged sensory system by simulating electrical neural signals, the most known device of this kind is the cochlear implant for the patients with sensorineural hearing loss [4]. Entering the 21st century, deep brain implants with neurostimulator became available for direct intervening brain activities to manage the movement disorders. These brain implants treat essential tremor and have the potential to prominently improve the life quality of patients with epilepsy, obsessive-compulsive disorder or Parkinson's disease [5].

In general, brain implants in treatment for neurological diseases require a chronical implantation under the skull either for intracranial physiologically parameters monitoring [6-8], high-resolution neural signal recording [9-11] or deep brain stimulation [12-14]. The existing brain implants are often connected with the off-body signal processing devices via percutaneous catheters or cables through a socket anchored on the skull. This bulky and fragile arrangement arouses concerns about patients' mobility and safety in long-term implementation. Therefore, wireless

solutions are currently demanded to take the place of the cable-based data and power links for obtaining cranially concealed safe wireless implants that last for a lifetime.

1.2 Scope and Objective of the Thesis

One of the major challenges in developing wireless brain implants is to build an efficient and reliable trans-cranial wireless link with the embedded implantable antenna. From the point of view of electromagnetics wave propagation, the human head is a sophisticated and heterogeneous environment consisting of dispersive dissimilar biological materials with relative permittivity and conductivity tens of times larger than that in ordinary wireless signal ambience. Since the brain implants need to be placed with a deep depth in the intracranial cavity, usually up to 15 mm for neural signal sampling and even several centimeters for deep brain stimulation, the inhomogeneous and lossy intracranial tissues surrounding the implantable antenna will considerably deteriorate antenna's radiation efficiency and ultimately worsen the overall quality of the trans-cranial link. In terms of implantable antenna development, the physical constraint of the implant poses strict requirements on antenna design regarding antenna form factors and miniaturization. The overall volume of an implant that hosts the antenna, electronic, sensor elements etc. needs to be as small as possible to minimize the biological intrusiveness for the sake of the patient's safety and comfort. The space left for the implantable antenna is usually limited, and the antenna is often inevitably to have a small electrical size. Electrically small antenna generally faces the issues of low radiation efficiency and limited bandwidth [15]. Thus, miniature antennas with high radiation efficiency are most favorable in implantable applications. In addition to antenna minimization, the path loss and deterioration of the antenna gain caused by the lossy tissue materials are with increasing trends versus frequency. As a consequence, the approach to minimize the antenna's electrical size with centimeter or even millimeter wave frequencies loses its effectiveness, and sub-GHz band are considered to offer the optimal size-performance balance for intracranial wireless systems from the angle of the overall link efficiency [16-17].

In chronical implant applications, battery-assisted device, due to the necessity of the periodical replacement of the bulky battery, is unlikely an optimal solution to prolong the implant's service life or to decrease the implant's overall size. Recently, radio-frequency identification (RFID) technique, which is based on the extra low-power and low-complexity backscatter communications, has been considered as a

promising solution to build the wireless link for implantable wireless systems [18-20]. These RFID based implants harvest the energy from the off-body interrogator's carrier wave and use impedance modulation to scatter back the data. Without the necessity of the power-wasting RF transmitters, the implant's overall power consumption notably decreases, and an entirely passive batteryless operation of the implant becomes feasible.

This thesis mainly focuses on exploring new design approaches for miniature antennas that could be implemented into RFID based implantable microsystems for wireless brain care applications. In balancing the operation distance, antenna footprint and tissue impact on antenna radiation, the far-field RFID operating in UHF band is selected as the target system in this work. Based on the characteristics of antenna radiation in the tissue environment, two novel design approaches for implantable antennas to establish an efficient and stable trans-cranial radio link are proposed:

1. A multimodal spatially distributed antenna system with a small implant part and a passive head-worn part is developed and evaluated with simulation and in-vitro measurement [Publication I], the antenna robustness towards the anatomical variability is evaluated with a semi-anatomical head model [Publication III], the realization of circular polarization operation with a modified wearable part is investigated and evaluated with wireless measurement [Publication VII].
2. A dual-split-ring miniature antenna with readily tuneable impedance is proposed and evaluated with in-vitro and in-vivo measurements [Publication II]. Additionally, the feasibility to build a passive pressure sensor with the proposed antenna structure is evaluated and preliminarily verified [Publication IV].

As the human body model is indispensable in the development of implantable antennas, a guideline on model selection towards a performance balance between computational efficiency and accuracy is provided [Publication VI]. In addition, the concept to enable the semi-passive operation of a sensory RFID IC without the assistance of batteries is proposed and verified [Publication V].

2 REVIEW OF THE LITERATURE

2.1 Far-Field RFID in Wireless Sensing Applications

RFID technology was originally developed to enable automatic and wireless identification of items attached with electronic transponders (also known as tags). The most distinguishing feature of an RFID system is its extra-low power consumption and simple RF frontend of the tags. Therefore, the power consumption of the RFID system is mainly predominant on the reader side, and the tags can be made small, passive, light weigh with low cost. Thanks to these advantages, the past decades have witnessed an increasing interest in developing RFID based sensors for large-scale, maintenance-free wireless sensor networks (WSN) and wearable and implantable sensors based wireless body area networks (WBAN). This section briefly overviews the operation principle and performance characteristics of an RFID system. Following the overview, the methods to enable wireless sensing with RFID tags are discussed.

2.1.1 Operation Principle of Far-Field RFID System

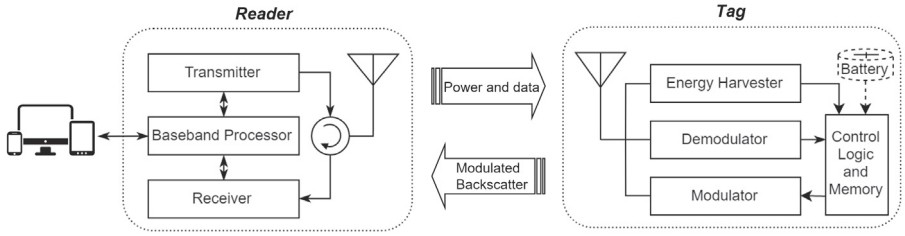

Figure 1. Major components and operation principle of an RFID system.

A typical RFID system consists of readers, tags, and a host for data management. The RFID reader contains a baseband processor, an RF transceiver, and reader antennas. The reader is controlled by the host with dedicated data management software. An RFID tag, on the other hand, has a relatively simple structure. A passive

tag only has a microchip (RFID IC) connected with the tag antenna, and for the semi-passive tags, an external battery is included to provide extra power to the IC. Figure 1 illustrates the major components and the operation principle of an RFID system.

As standardized in EPC C1G2, the RFID system works in a half-duplex style, and the communication between a reader and tags is always initialed by the RFID reader [21]. To start an interrogation with the tags, the reader emits a continuous carrier wave followed by a modulated command signal to the tags. When waiting for the response, the reader keeps emitting an unmodulated carrier. In a passive tag, the energy harvester integrated inside the tag IC scavenges energy from the received carrier via the tag antenna. Once the harvested energy is sufficient to activate the logic circuitry, the IC starts to demodulate the reader's signal and alter its internal impedance in a coding scheme based on the tag's data. The alternation of the IC impedance leads to the varying of the reflection coefficient of the tag antenna. As a result, the tag antenna modulates the incoming carrier and scatters an amplitude or phase-shifted version back to the reader. When the reader detects and demodulates the backscattered signal, the data from the tag can be decoded and delivered to the data management system for further processing. Neither passive tags nor semi-passive tags contain active RF transmitters; instead, they communicate with the reader by backscattering the reader's carrier using impedance modulation. The major factor differentiates the semi-passive tag from the passive one is its power source. The operation of a passive tag completely depends on the energy harvested from the reader's carrier. Thus, the passive tag can only respond to the reader when the harvested energy exceeds a certain threshold (known as the IC sensitivity) to activate the IC. In a semi-passive tag, the external battery provides the power for the IC, and the tag can respond to the reader's command whenever requested.

2.1.2 Performance Characteristics of Far-Field RFID System

The performance of an RFID system is commonly characterized by the interrogation distance between a reader and tags. Either the forward link (reader to tag) or the reverse link (tag to reader) can potentially limit this distance. This subsection briefly analyses the link budget of an RFID system and discuss the strategy to maximize the interrogation distance.

Forward link budget

In the forward link, the reader transmits the EM wave to its interrogation region. The tag antenna interacts with the incident wave and the power absorbed by the IC in the free space can be calculated with the Friis equation as [22],

$$P_{r\to t} = \chi_{pol}\left(\frac{\lambda}{4\pi r}\right)^2 P_r G_r G_t(1-|\Gamma|^2) \text{ with } \Gamma = \frac{Z_{ic} - Z_a{}^*}{Z_{ic} + Z_a} \tag{2.1}$$

where, χ_{pol} is the polarization loss factor between the reader antenna and tag antenna, λ is the wavelength of the operation frequency, r is the distance between the reader and the tag, P_r is the output power from the reader, G is the gain of the antennas, with the subscript r and t denoting the reader antenna and tag antenna, respectively, $Z_a = R_a + jX_a$ is the antenna impedance, $R_{ic} = R_{ic} + jX_{ic}$ is the IC impedance at its wake-up power threshold and Γ is the power reflection coefficient due to the mismatch between the tag antenna and the IC. Alternatively, $\tau = 1-|\Gamma|^2$ is defined as the power transfer efficiency given by [23],

$$\tau = \frac{4R_{ic}R_a}{|Z_{ic} + Z_a|^2}. \tag{2.2}$$

Here, τ measures the ratio of the power absorbed by the IC to the total available power on the tag antenna.

Reverse link budget

In the reverse link, the tag antenna backscatters the reader's carrier wave in two different modes: structure mode scattering and antenna mode scattering. The former one results from the inducted surface currents flowing through the antenna conductor. These currents are confined in separated regions on the antenna surface and are independent of the matching condition between the antenna and the IC. The antenna mode scattering, on the other hand, results from the power reflection due to the impedance mismatch between the IC and the tag antenna. Therefore, by appropriately manipulating the IC impedance, antenna mode scattering can be utilized to carry information.

When the IC switches its internal impedance between two states, the antenna mode scattering can be characterized with differential radar cross-section (*⊿RCS*) [24],

$$\Delta RCS = \chi_{pol} \frac{\lambda^2}{4\pi} {G_t}^2 K, \tag{2.3}$$

where, *K* is the modulation loss factor written as:

$$K = \alpha |\Gamma_1 - \Gamma_2|^2. \tag{2.4}$$

The coefficient α is mainly determined by the duty cycle of the modulation method, and Γ_1 and Γ_2 are the two reflection coefficients corresponding to the two states of the IC impedances. *⊿RCS* measures the ratio of the antenna differential backscattered power to the power density of the reader's incoming wave [24]. Similarly, according to the Friis equation, the power of the backscattered signal received by the reader in the free space can be given as [23],

$$P_{t\to r} = \chi_{pol} \frac{\lambda^2}{(4\pi)^3 r^4} P_r {G_r}^2 \Delta RCS \tag{2.5}$$

According to the above analysis of the forward link and reverse link, successful communication between readers and tags requires the following condition to be satisfied: $P_{r\to t}$ exceeds the IC sensitivity meanwhile $P_{t\to r}$ is higher than the reader's sensitivity.

In the forward link, based on Equation 2.1, $P_{r\to t}$ is proportional to the transmitted power P_r of the reader, the gain of the reader and tag antennas, and the power transfer efficiency *τ*. Generally, P_r is restrained by the regional *EIRP* limit; in Europe, $P_r G_r$ cannot exceed 3.25 W [23]. Therefore, to optimize the forward link, the tag antenna should be properly designed to provide a decent antenna gain. Meanwhile, to maximize power transfer efficiency *τ*, the impedance of a tag antenna should be complex conjugate matched to the IC impedance.

In the reverse link, according to Equation 2.5, $P_{t\to r}$ is not only determined by the antenna properties but also influenced by the modulation method adopted by the IC. For instance, if the duty cycle of the modulation method is 50% and the IC switches its impedance between short and the impedance that maximizes *τ*, the loss factor *K* is -6 dB [24]. In contrast, if the IC impedance switches between open and short, then nearly all the incident energy is scatted back. The corresponding *K* decreases to 0 dB

which means $P_{t\to r}$ has 6 dB improvement than that with the previous modulation method [24]. However, this aggressive modulation method is only applicable for semi-passive tags, as they are powered by the external battery and do not need to absorb the energy from the incident wave.

Interrogation Distance

In most cases, the interrogation distance of an RFID system is limited in the forward link. This is especially true for readers with high sensitivity (up to -80 dB) working with passive tags. This means the reader can hear the tag as long as the power absorbed by the IC exceeds the IC's power-on threshold P_{th}. In this case, the maximum interrogation distance can be derived from the link budget of the forward link by substituting P_{ic} by P_{th} into Equation 2.1,

$$r_{forward} = \frac{\lambda}{4\pi}\sqrt{\frac{\chi_{pol} P_r G_r G_t \tau}{P_{th}}} \tag{2.6}$$

In certain case, when the sensitivity of the reader is not high enough, even the tag is activated, the backscattered signal is too weak to be detected by the reader. Then the interrogation distance is limited in the reverse link. Under such circumstance, the tag modulation scheme should be adjusted to increase the power strength of the backscattered wave.

2.1.3 Wireless Sensing with RFID Tags

Wireless sensing with RFID tags is realized by manipulating the tags' backscattered signal in a way to reflect the variation of certain environmental parameter. With such an arrangement, the reader can extract the sensed information by analyzing the features of the received backscattered signal. The manipulation of the backscattered signal can be achieved with antenna-based or chip-based approaches.

Antenna-based Approach

In the antenna-based approach, the tag antenna is engineered so that its antenna parameters (e.g. gain or impedance) directly or indirectly change with the

environmental stimuli. The changed antenna parameters lead to the strength fluctuation or the resonant frequency shift of the tag's ΔRCS and consequently influence the optimal frequency of the tag's threshold power. By analyzing the frequency variation of the tag's threshold power, the reader can remotely obtain the sensed information. The antenna-based approach, due to its easy realization and low complexity, is commonly used in developing passive sensors to monitor temperature [25], strain [26], pH value [27], humidity [28] etc. Based on a dual-split-ring antenna, the author developed a miniature pressure sensor that can potentially monitor the intracranial pressure [Publication IV]. This sensor is discussed with more details in Subsection 4.4.4.

Chip-based Approach

Instead of engineering the tag antenna, tailoring the tag's IC is another way to endow the RFID tag with sensing ability. This can be achieved by interfacing the IC to sensor elements and encoding the sensed data into the tag's Electronic Product Code (EPC) or Transponder ID (TID) [89-90]. The EPC commonly has a length of 96 bits and the TID typically with a length of 64 bits [21]. Suppose an Analog to Digital Converter (ADC) with an accuracy of 10 bits, the data lengths of EPC and TID are sufficient to host several samplings in a single tag response. Alternatively, there are sensory RFID ICs with customed protocols specifically for sensing applications [29-30]. These ICs usually come with inbuilt ADC and the interface to connect external sensors. To work with these ICs, specific readers are generally required.

Chip-based RFID sensors, due to their additional auxiliary circuitry and sensor elements, provide advanced functionalities with a high sensing accuracy. These advantages cannot be obtained with the antenna-based ones. However, the increased complexity of these chip-based sensors leads to the rise of power consumption. This is the reason that chip-based sensors usually work in semi-passive mode with external batteries. Although some proposed sensors support fully passive operation, it is usually at the cost of considerably decreased IC sensitivity that limits its applicability [29-30]. To tackle this problem, the author conceived of a batteryless semi-passive RFID sensor platform [Publication V]. This work is discussed with more detail in Subsection 4.1.

2.2 Antenna Radiation in Human Tissue Environment

Antennas are passive transducers that convert alternating electric currents into propagating electromagnetic (EM) waves and vice versa. They are crucial components in every wireless communication system and play a significant role in obtaining reliable and efficient communication links. Recently, the advent of the wireless era in medicine and healthcare has prompted a considerable demand for the development of antennas that could be embedded into miniature implantable devices [91-93]. Unlike conventional antennas that operate in the free space or in another word: lossless medium, implantable antennas are required to radiate effectively in a dispersive heterogeneous tissue environment. Thus, the knowledge of the influences brought by the lossy tissues is highly valuable in implantable antenna design and optimization. Meanwhile, implantable devices generally have strict requirements on form-factor, biocompatibility, and durability; these special constraints bring considerable challenges which require extra consideration in the antenna development. This subsection aims to review the essential knowledge to design the antenna for the implantable system and to briefly discuss the challenges in the development of implantable antennas.

2.2.1 Radiation of Magnetic Dipole in Lossy Material

In order to understand the characteristics of antenna radiation in human tissue, let us conceive of an infinitesimal magnetic diploe that radiates in a homogeneous lossy material with an infinite volume. The dielectric properties of the material are characterized with permittivity ε, conductivity σ, and permeability μ. The corresponding propagation constant k is given as $\sqrt{j\omega\mu(\sigma+j\omega\epsilon)}$. In this analysis, all the quantities are assumed to have the $e^{j\omega t}$ as the harmonic time factor. To facilitate the analysis, the magnetic dipole is equivalent to a circulating current I with a loop area of dA. It is placed at the origin of a Cartesian coordinate system, as shown in Figure 2.

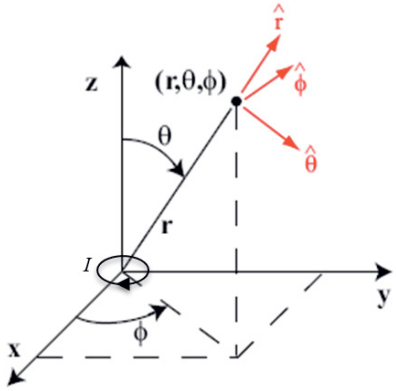

Figure 2. Magnetic dipole in a spherical coordination system.

The magnetic vector potential of the circulating current loop in the Cartesian coordinate system is given by [33, Ch. 24],

$$\mathbf{\Pi} = \frac{IdA}{4\pi}\frac{e^{-kr}}{r}\,\hat{z}. \tag{2.7}$$

Then the fields' components of the current loop can be conveniently represented with $\mathbf{\Pi}$ as [33, Ch. 24],

$$\mathbf{E} = -j\mu\omega\,\nabla \times \mathbf{\Pi}, \tag{2.8}$$

$$\mathbf{H} = -k^2\mathbf{\Pi} + \nabla(\nabla \cdot \mathbf{\Pi}). \tag{2.9}$$

Substituting Equation 2.7 into Equation 2.8 reduces the electric field components in the corresponding spherical coordination system to

$$\begin{aligned} \mathbf{E_r} &= \mathbf{E_\theta} = \mathbf{0}, \\ \mathbf{E_\phi} &= -\frac{j\mu\omega I\,dA}{4\pi r^2}(1+kr)e^{-kr}sin\theta, \end{aligned} \tag{2.10}$$

and the corresponding magnetic field can be derived as

$$\mathbf{H_r} = \frac{I\,dA}{2\pi r^3}(1+kr)e^{-kr}cos\theta, \tag{2.11}$$

$$\boldsymbol{H_\theta} = \frac{I\,dA}{4\pi r^3}(1 + kr + (kr)^2)e^{-kr}sin\theta,$$

$$\boldsymbol{H_\phi} = \mathbf{0}.$$

With the obtained field components, the averaged radiated power density in the radial direction can be calculated with the Poynting vector as [33, Ch. 24],

$$\boldsymbol{P}_{rad} = \frac{1}{2}Re\left(\boldsymbol{E_\phi} \times \boldsymbol{H_\theta}^*\right) = \left(\frac{I\,dA}{4\pi}\right)^2 \frac{\mu\omega}{r^5}(1 + \alpha r)(\alpha\, r\, sin\theta)^2 e^{-2k'r}. \quad (2.12)$$

Here, in Equation 2.12, the displacement currents are neglected, and *k'* becomes $\sqrt{(\sigma\mu\omega)/2}$. Then if we choose an enclosing sphere with a radius of *R*, the total power radiated crossing its surface $\boldsymbol{s}$ can be calculated as [33, Ch. 24],

$$\boldsymbol{P}_{Tm} = \oiint_s \boldsymbol{P_r} \cdot d\boldsymbol{S} = \frac{\sigma\mu^2\,\omega^2\,(I\,dA)^2}{12\pi}\left(\frac{1}{R} + \frac{\mu^2\,\omega^2}{8}\right)e^{-2k'R}. \quad (2.13)$$

From Equation 2.13, it is obvious that the total power radiated by a circulating current loop is inversely proportional to the distance from the radiator to the selected sphere surface. This is a different situation when the current loop radiates in lossless material where the total power crossing a sphere enclosing the source is independent on *R*. Another interesting hint implied from Equation 2.13 is that near the current loop the radiated power is proportional to R^{-1}, if we compare with an electric dipole in the same lossy material, its radiated power near the source will have an R^{-3} dependence as shown in Equation 2.14 [33, Ch. 24],

$$\boldsymbol{P}_{Te} \approx \frac{1}{16\pi\mu\omega}\left(\frac{Idl}{\sigma\delta}\right)^2 \frac{1}{R^3}. \quad (2.14)$$

Due to this R^{-3} dependency, the electric dipole dissipates more energy than the magnetic dipole in the lossy material surrounding it. This is because the wave impedance near the electric dipole is largely resistive while the impedance of the magnetic dipole is mainly inductive [34]. This can be very useful information when choosing antenna types for implantable applications.

2.2.2 Tissue Impact on Antenna Performance

From the previous discussion of magnetic dipole radiation in a lossy environment, we have the idea that the lossy dielectric properties significantly affect the antenna radiation. This situation becomes even more complicated when considering the heterogeneous structure of the human tissues. This subsection briefly discusses the tissue impact on several major antenna parameters. Due to the antenna reciprocity theorem, in the following discussion, the antenna is assumed to be the transmitting one.

2.2.2.1 Radiation Efficiency

Radiation efficiency is one of the most important parameters to characterize antenna EM performance. It measures the ratio of the antenna's radiated power to the total power that the antenna absorbs from the source. In the tissue environment, there are mainly two factors that affect the efficiency of the implantable antenna: absorption losses inside tissues and reflection losses at the tissue boundaries [34]. Then, we can have the following expression to define the antenna radiation efficiency,

$$\boldsymbol{e_{rad}} = \frac{\boldsymbol{P}_{rad}}{\boldsymbol{P}_{rad} + \boldsymbol{P}_{abs} + \boldsymbol{P}_{tissue\_ref}}. \tag{2.15}$$

Absorption Losses in Tissues

When the antenna is placed in the lossy tissue environment, a certain part of the radiated energy is absorbed by the surrounding tissue due to tissue's non-zero effective conductivity. The averaged absorption power losses in a certain tissue with a volume of V can be calculated by [33, Ch. 24]

$$\boldsymbol{P}_{abs} = \frac{1}{2}\int_V w_{vol} dV, \text{ with } w_{vol} = \frac{1}{2}|E|^2\sigma_e = \frac{1}{2}|E|^2(\sigma' + \omega\varepsilon'') . \tag{2.16}$$

Here w_{vol} is the dielectric loss density of the tissue. According to equation 2.16, the absorption losses are proportional to the tissue volume, operation frequency, strength of the electric field and the effective conductivity of the surrounding medium. The volume of the tissue is generally uncontrollable with a given implant site. However, the rest of the terms can be carefully managed to lower the overall

energy absorption. Intuitively, lowering the operation frequency results in smaller tissue absorption. However, this is usually at the cost of the decreased operation distance and data rate, and increased antenna size. In terms of the surrounding electric field $\boldsymbol{E}$, if we take a closer look at Equation 2.12 and 2.10 from the last subsection, $\boldsymbol{P}_{rad}$ and $\boldsymbol{E}$ both have the independent power terms that dominate in the antenna's near-field or far-field with different dependencies on *r*. The tissue absorption mainly happens in the antenna's near field where the energy is coupled with the surrounding tissues. Since typical human tissues are non-magnetic, a dominant magnetic field in the antenna's near field can help to decrease the tissue absorption. This is the reason why the magnetically excited antenna has higher radiation efficiency in a lossy environment. Moreover, proper antenna insulation using materials with low conductivity can reduce the tissue coupling in the near field and consequently lower the tissue absorption. This is one of the reasons that the antenna insulation is essential in implantable applications.

Reflection Losses on Tissue Boundaries

From the perspective of electromagnetic wave propagation, the human body is a heterogeneous medium with a variety of layered tissue types having dissimilar dielectric properties. The difference of the dielectric properties causes the wave impedance mismatch on the tissue boundaries and results in the reflection losses. The reflection losses, contrary to the absorption losses, are reversely proportional to the frequency [34] and become more manifest on the boundaries with higher contrast of wave impedances, such as the CSF-skull interface and the skin-air interface in the through-cranial radio link. Since the implantable antenna mainly radiates from the high dense tissue to the less dense one, a considerable amount of energy is reflected on the tissue boundaries and excites the surface wave that finally dissipates in the surrounding tissues [34]. An on-skin passive device that changes the surface properties can help to alleviate the mismatch of the wave impedance and reduce the reflection losses. Utilizing this technique, the author developed a spatially distributed antenna that is discussed in Section 4.3. Apart from the mismatch of the wave impedance, the reflection losses are also highly influenced by the angle of the incident $\boldsymbol{E}$ field, which implies that the placement of the implantable antenna regarding the tissue boundaries could affect the antenna radiation efficiency. This phenomenon is further discussed in Subsection 4.4.2.1.

2.2.2.2 Radiation Pattern and Directivity

Antenna radiation pattern refers to the directional dependence of the strength of the radiated electromagnetic wave in the far-field. When the antenna is radiating in the lossy medium, e.g. the heterogeneous human tissue, the radiation from the different part of the antenna may experience dissimilar attenuation, which makes the radiation pattern significantly different from that in the free space. Moreover, the human body is a dynamic and complex environment, not only the surrounding tissues, but the whole body has an impact on the radiation pattern. Fortunately, full-wave computational electromagnetic modeling tools with accurate tissue phantoms can be beneficial in analyzing the radiation pattern of the implantable antenna. Another antenna parameter that is relevant to the radiation pattern is the antenna directivity. It measures the maximum radiated power density of the antenna versus the power density radiated from an isotropic one with the same input power. In the implantable application, highly directional antennas with the main lobe pointing outwards human body are favorable to obtain an efficient through-body radio link.

2.2.3 Challenges in the Development of Implantable Antennas

In the development of antennas for the implantable system, the physical constraint of the implant is the major challenge that needs to be carefully addressed. The overall volume of an implant that holds the antenna, electronic, sensor elements etc. needs to be as compact as possible to minimize the biological intrusiveness and to improve the patients' comfort. The space left for the implantable antenna is usually very limited, and the antenna is often inevitably to have a small electrical size. Problematically, electrically small antenna generally faces the issues of low radiation efficiency and limited bandwidth. Thus, miniature antennas with high efficiency are most favorable in implantable applications. Additionally, to obtain better compatibility between the implant and the physical features of the tissue environment, implantable antennas are often required to be coplanar and flexible. This flexibility makes the antenna prone to the distortion in the complex tissue environment, and thus, antenna robustness towards the geometrical distortion becomes a factor needs to be taken into consideration in the process of antenna development.

Apart from the physical constraint, tissue safety due to the exposure to the radiated electromagnetic wave also needs to be carefully tackled. The Specific Absorption Rate (SAR) is the parameter that measures the power dissipation in the

lossy tissue per unit mass. SAR can be calculated by dividing the P_{abs} in Equation 2.16 with the total mass of the selected tissue. The maximum input power of the antenna must be controlled so as not to exceed the SAR limit. In this work, the target system is fully passive, and thus the SAR is not evaluated.

Another special consideration in RFID systems or more generally, passive wireless systems with an energy harvesting unit, is the complex conjugate impedance matching between the antenna and the microsystems. As already discussed in Section 2.1.2, these systems, due to the essential charge storage component and the non-linear AC rectifier, have an overall capacitive impedance with its value varies from different designs. For these systems, an antenna with a readily tunable impedance that can help to achieve a good complex conjugate matching to the target system is of high demand. A miniature implantable antenna with a wide tunable impedance range developed by the author is discussed in detail in Section 4.4.

So far, quite a few techniques have been proposed for antenna development in addressing the design constraints and challenges brought by the human tissue environment. For antenna miniaturization, high permittivity substrate and superstrate are used and evaluated in [49-51]; meandering or slots to prolong the current traces are reported in [52-53] and inverted-F structure and multi-layered patch antenna are extensively studied in [54-56]. The authors in [40, 57, 58] elaborately discussed the methods to mitigate the tissue absorption and to reduce the SAR. Antenna insulation is specifically studied in [59] with physical models and experimental results. In terms of the antenna impedance matching, different loading approaches are presented in [60-61].

In reviewing the most recent works, most of the proposed implantable antennas are only capable for subcutaneous applications with an implant depth less than 5 mm [50, 56, 62-64, 86-87, 94]. Some antennas developed for deep implant applications with an implant depth of more than 12 mm; however, they either come with a big antenna size or with non-ideal radiation efficiency [65-68]. The small implantable depth, limited antenna radiation efficiency or the non-ideal antenna form factor makes these antennas not favorable for intracranial implantable applications. In addressing this issue, the author proposed two approaches to develop miniature antennas for deep brain backscattering implantable system. The detail of the antenna configuration and performance evaluation is presented in Section 4.3 and 4.4.

3 MATERIALS AND METHODS

3.1 Computational EM Modeling Method

Maxwell's Equations are the fundamental that governs the behavior of EM field and plays an irreplaceable role in antenna design, EM wave propagation analysis, EM compatibility etc. However, it is virtually impossible to obtain the analytical solutions of these equations without canonical configurations. To address this problem, a new form of EM analysis based on computational EM modeling has emerged, where the numerical approximation of Maxwell's equations is alternatively used to describe the behavior of EM field in realistic configurations [80-81]. In the literature, the most adopted numerical techniques for EM modeling are Method of Moments (MoM), Boundary Element Method (BEM), Finite-Element Method (FEM) and Finite-Difference Time Domain (FDTD). These techniques can be categorized according to the forms (integral or differential) of Maxwell's equations on which they are based or the domain (time or frequency) where the numerical solutions are derived. Each technique has its own strengths and weaknesses; therefore the technique should be properly selected based on the given EM problems. In general, MoM is usually specialized in modeling multilayer planar structure; BEM is suitable for solving radiation problems of metal plates and thin wires, but it is not capable of modeling inhomogeneous structures. FEM and FDTD are both capable in modeling inhomogeneous and complex structures; however, they cannot accurately model thin wires. A detailed survey and comparison of the current computational EM modeling techniques can be found in the report presented in [82].

3.1.1 FEM Based Computational EM Modeling Tool

Since all the EM modeling conducted in this work is carried out in FEM based ANSYS High Frequency Structure Simulator (HFSS), this subsection presents a brief review of FEM.

The basic idea of FEM is to discretize a large problem domain into a mesh of small finite constituent elements. In each element, basis functions are generated to

interpolate the spatial variation of the unknown and a solution for the entire domain is obtained when these interrelated field solutions satisfy the boundary conditions across every inter-element boundary [83].

In HFSS, the element units for 2D and 3D problems are triangle and tetrahedra, respectively. The unknown is the electric field components along the edge of each element [95]. When the electric field is derived for the entire structure, HFSS calculates the magnetic field using Ampère's circuital law and determines the solution of S-matrix. To guarantee the accuracy of the results, the solution process in HFSS is conducted in an iterative manner [95]. In each iteration of the solving process, the error is analyzed, and the regions with a high degree of error will be discretized with a refined mesh, and then the solution is recomputed. This iterative process repeats until the convergence criterion is satisfied or the adaptive passes reach the requested number of times. The combination of FEM and the adaptive solution process makes HFSS a powerful tool to analyze the EM behavior in arbitrary complex structures and to facilitate the development of antennas for biomedical applications.

3.2 Numerical Modeling of Human Tissue Environment

Numerical modeling of human tissues has become an indispensable technique that expedites research in biomedicine [96], biomechanics [97-98], and electromagnetics [99-100]. In the development of antennas for biomedical applications, numerical tissue models provide a powerful tool for scientists and engineers to evaluate the interaction between the radiator and biological tissues. On the one hand, these models provide the key information about the biological tissues' impact on antenna parameters, such as antenna impedance, radiation efficiency and directivity [101-102]. This information helps to optimize the antenna performance in the tissue environment. On the other hand, these models predict the tissue reaction to the electromagnetic exposure caused by antenna radiation [103-104]. Since excessive radiation power increases the tissue temperature and may eventually cause tissue damage, it is crucial to evaluate tissue safety when developing antennas for wearable and implantable applications. This subsection overviews the methods to model the dielectric properties and geometry of the human tissue environment.

3.2.1 Dielectric Properties of Human Body Tissues

In consideration of the frequency ranges and the corresponding power level in the scope of this work, the EM properties of biological tissues can be assumed as dispersive, isotropic, linear, and non-magnetic ($\mu=\mu_0$) [44, Ch. 2]. Thus, a good knowledge of the tissue scalar permittivity and conductivity is sufficient to predict the interaction between biological tissues and EM fields. The permittivity of biological tissues is determined by a variety of complicated phenomena [44, Ch. 2]. Each phenomenon has its own dominance in a certain frequency range; consequently, the tissue permittivity disperses strongly with the frequency. In the frequency range of gigahertz, due to the high-water content of the human body, the tissue permittivity is dominant by the dipolar relaxation that arises from the molecule dipolar moments' alignment when an alternating electric field is applied [44, Ch. 2]. The permittivity related to the dipolar polarization can be written as

$$\varepsilon_d = \varepsilon' - j\varepsilon'' . \tag{3.1}$$

ε_d is a function of frequency and relaxation time of which the dipolar polarization reaches its saturation state. Its real part is proportional to the total moment of the molecule dipoles, and the imaginary part indicates the energy absorbed and dissipated in the tissue due to the rotation of molecule dipoles. Similarly, the tissue conductivity is also dispersive and can be written as,

$$\sigma = \sigma' - j\sigma'', \tag{3.2}$$

where σ' is from the loss of the ionic conductivity and σ'' reflects the time lagging of ionic conduction response [44, Ch. 2]. The final complex effective permittivity ε_c is determined by the superimposed influence of ε_d and σ, and it is given by the Ampere-Maxwell Equation as,

$$\varepsilon_c = \varepsilon_e - j\frac{\sigma_e}{\omega}, \tag{3.3}$$

where ε_e and σ_e are the tissue effective permittivity and conductivity, respectively. They are derived as,

$$\varepsilon_e = \varepsilon' - \frac{\sigma''}{\omega}, \tag{3.4}$$

$$\sigma_e = \sigma' + \omega\varepsilon''. \tag{3.5}$$

The ratio of the imaginary and real parts of the ε_c is defined as the loss tangent given as,

$$tan\delta = \frac{\sigma_e}{\varepsilon_e \omega}. \tag{3.6}$$

The loss tangent indicates the power dissipation due to the effective conductivity of the medium. Moreover, the non-zero effective conductivity results in the propagation loss of the electromagnetic wave inside the human tissue. The skin depth is very useful to quantify the relationship between the propagation distance and the decrease of the field amplitude. It is defined as the reciprocal of attenuation constant α (Np/m) [44, Ch. 2],

$$\delta = \alpha^{-1} = \frac{1}{\omega}\left(\frac{\mu\varepsilon(\omega)}{2}\right)\left\{\left(1 + \left(\frac{\sigma}{\omega\varepsilon(\omega)}\right)^{1/2}\right) - 1\right\}^{1/2}. \tag{3.7}$$

Apparently, the skin depth decreases with the frequency and significantly depends on the tissue dielectric properties. The typical skin depth of human tissue at 900 MHz is about 1 cm, which means that the amplitude of the electric field and magnetic fields decrease by 1/e with a propagation distance of 1 cm inside the tissue environment. With a propagation distance of 3 cm, there is only 1% of energy left in the electromagnetic wave.

Tissue dielectric properties are experimentally obtained by in-vitro and in-vivo measurement of ε_c. Currently, the IT'IS tissue dielectric database [45], based on Gabriel's measurements and the four-term Cole-Cole dielectric relaxation model [46, 47], is widely used for electromagnetic modeling of human tissues. This database includes the dielectric properties of 45 human tissues in a frequency range from 10 Hz to 100 GHz. Figure 3 and 4 show the relative permittivity and conductivity of eight major tissue types of the human head in a frequency range from 1 MHz to 10 GHz, respectively. Overall, the tissue relative permittivity monotonously decreases over the entire selected frequency range but with a slowdown trend starting from 100 MHz. The fat and skull have a relative lower permittivity and conductivity in comparison with other tissue types. This is because of the low-water content in these two tissue types. In contrast, due to the high-water content in CSF and blood, these two tissue types possess a high value in both relative permittivity and conductivity. Another noticeable trend is that the conductivity of all the eight tissue types

undergoes a sharp rise above 1 GHz. This indicates that the tissue absorption losses will significantly increase when the operation frequency of the antenna is higher than 1 GHz.

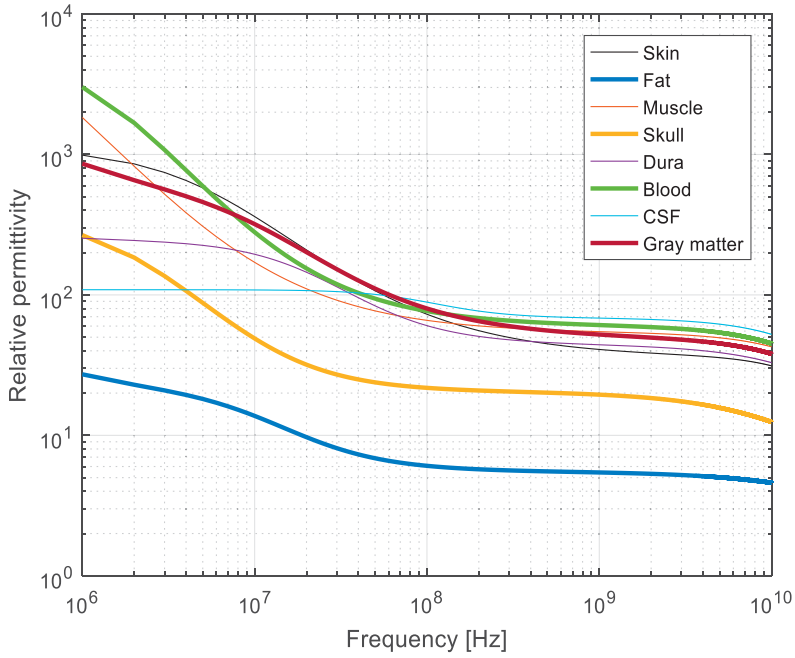

Figure 3. Relative permittivity of the major tissue types of human head.

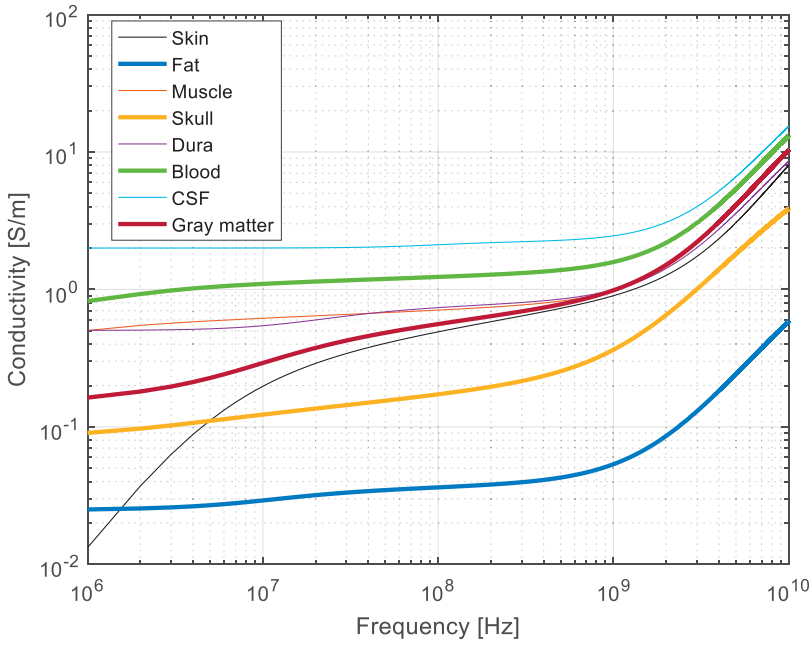

Figure 4. Conductivity of the major tissue types of human head.

3.2.2 Geometry of Human Body Tissues

In modeling the geometry of the human body tissues, canonical models are extensively used as they can be conveniently built with the embedded CAD tools that are available in most computational EM modeling platforms. These CAD-based canonical models use geometric primitives to model the geometry of the human body. Based on the target implant sites, the shape of the model can be cuboid, spherical or cylindrical. For example, a rectangular cuboid is commonly used to model the human torso [35]; cylinders are often made to simulate arms [36-37]; and spherical models are usually adopted for the human head [38]. To obtain a more accurate representation of the human body, these canonical models can be even combined [39]. In terms of the constituting materials, the canonical models can be made homogeneously with only single tissue type or with a layered structure that includes several different tissue types to obtain a better approximation of the body structure. For instance, three-layered structure with skin, fat and muscle tissue types are widely used for percutaneous implants [36]; the intracranial environment is normally modeled with a six-layered sphere including the tissue types of skin, fat, muscle, skull, CSF, and grey matter [38]. The advantage of the canonical model is its

simplified geometries that allow to reduce the consumption of computational resource and consequently to increase the simulation speed in full-wave electromagnetic solvers. Moreover, its favorable deformability offers the flexibility to investigate the impact of tissue-structure's variations on the antenna performance. As for the disadvantage, the canonical model, due to its simplified geometrical structure, provides limited anatomical adequacy. This inadequacy affects the accuracy of the simulation results, especially in the evaluation of antenna far-field parameters, such as the radiation efficiency and directivity [40].

Alternatively, the geometry of the human body can be modelled with the detailed geometrical information extracted from high-resolution medical imaging data (e.g. magnetic resonance imaging (MRI) or cryosections) [41]. For instance, the most comprehensive anatomical human body models from Virtual Population Project [42] were generated based on the whole-body MRI scanning data, and the body models from Visible Human Project [43] were built with the high-resolution scanning of cryosections images. These anatomical models are currently widely used in computational EM and radiological simulations. Anatomical models contain highly detailed structural information of the human tissues, and thus they are inevitably to be computationally expatiatory when adopted in simulation platforms. Moreover, since each anatomical model contains the anatomical details of a particular scanned individual, it is generally difficult to modify the geometrical structure of the anatomical models to evaluate the impact of anatomical variability. In antenna development, since the propagation of electromagnetic waves is largely influenced by the geometry and boundary structure of the surrounding materials, anatomical models provide higher accuracy in predicting the antenna radiation performance than the canonical ones. A guideline for selecting the human head model that achieves an optimal balance between computational efficiency and accuracy is provided in Subsection 4.2.

3.3 Experimental Modeling of Human Tissue Environment

In the experimental evaluation and validation of implantable antennas, experimental phantoms are necessary to mimic the intended implantation scenario. These phantoms include the physically fabricated tissue-mimicking phantoms and animal tissue models.

3.3.1 Physical Tissue Mimicking Phantom

In the preliminary evaluation of the implantable antenna's performance, physically manufactured tissue phantoms have been commonly used. Several recipes for preparing the phantom that simulates the tissue environment at different frequency bands have been proposed [70, 84, 85]. The main ingredients of the physical phantoms are deionized water, sugar, and salt. Deionized water serves as the base ingredient, and the phantom permittivity and conductivity can be adjusted with the proportion of the sugar and salt. Generally, the phantom permittivity decreases with the addition of the sugar and the conductivity increase with the proportion of the salt. To control the viscosity of the phantom, agar and other ingredients are usually mixed with the main ingredients.

In this work, the tissue mimicking-liquid with 39 % of deionized water, 58 % of sugar and 3 % of salt is prepared according to the receipt presented in [70]. The dielectric properties of the liquid are measured with Agilent Technologies 85070E Dielectric Probe Kit and adjusted in accordance with the FCC guideline for the 'average head' model with a conductivity and relative permittivity of 0.77 S/m and 45.74, respectively at 915 MHz [71]. Finally, the formulated liquid is transferred into a plastic truncated cone container (height: 8 cm, lower radius: 6.5 cm, upper radius: 8.5 cm), which has a dimension comparable to that of the human head.

3.3.2 Animal Tissue Model

Animal tissue models are recommended to further evaluate the implantable antenna when its functionality is verified with physically manufactured phantoms. Animal tissue models can be a certain part of the animal, e.g. porcine meat [56, 87], rat skin [88], sheep fat [54], piglet's head [86] and chicken breast [51]. The main purpose of using the animal tissue model is to evaluate the effects that the physical phantoms cannot properly reflect. For example, physical phantoms are generally made to emulate the actual biological tissue environment in a limited frequency band. Due to the frequency dependence of the biological tissue properties, the physical phantoms become less effective when evaluating the performance of multiband and wideband implantable antennas. Furthermore, the animal tissue models provide access to evaluate the effect of multiple types of tissues and the surgical procedures on antenna performance.

In this work, an in-vivo animal test with Wistar rats is carried out to evaluate the performance of the proposed implantable antenna in a realistic biological environment. The detail of this animal test is discussed in Subsection 4.4.3.2.

4 RESULTS AND DISCUSSION

4.1 Batteryless Semi-Passive RFID Sensor Platform

The advent of RFID IC with sensing ability has significantly facilitated the development of RFID sensors with high accuracy and good reliability. Nevertheless, due to the increased power consumption, the sensory ICs working in passive mode not only have a non-ideal IC sensitivity but also with limited access to the sensing functionalities. Powering the IC with an external battery is a simple solution to solve this problem; however, the battery increases the total cost of the sensor. Moreover, the periodical replacement of the battery requires extra maintenance effort, which hinders its implementation in biomedical applications and large-scale maintenance-free WSN. When reviewing the usage scenarios of these sensors, one common ground is that a high-speed real-time sensing performance is usually not necessary. A sampling interval with several seconds or even several minutes is sufficient for most of the sensing applications. With this consideration, the author conceived of a batteryless sensor platform [Publication V] that operates in a time-divided manner with two switching modes: energy-harvesting mode and backscattering mode.

4.1.1 Platform Architecture and Operation Mechanism

The block diagram in Figure 5a illustrates the structure of the proposed platform. The platform consists of an antenna, an RFID IC, and an energy harvester. As shown in Figure 5a, they are linked with a single-pole-double-through RF switch.

The selected sensory chip is the SL900A IC [29] which contains a built-in temperature sensor and an interface that supports the connection with up to two external sensor elements. This IC supports both passive and semi-passive operations; nevertheless, the IC sensitivity in fully passive mode is only -6.9 dBm. In our test, the sensitivity drops even lower when processing sensing commands. In contrast, when an external power source is available to the IC, the IC sensitivity improves to -17 dBm. Enabling the IC to operate in semi-passive mode can significantly improve the system reliability and interrogation distance. The RF switch utilized in this

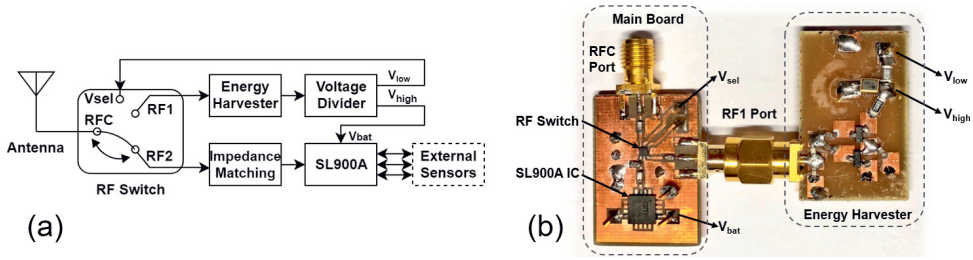

Figure 5. a. Block diagram of the proposed sensor platform. b. Prototype of the proposed sensor platform. [Publication V]

platform is the GRF6011 from Guerrilla. Its favorable fail-safe property ensures a default connection between RFC port and RF1 port even without DC bias on its control pin.

This system initializes from the energy-harvesting mode where the antenna and energy-harvester are connected through the fail-safe RF link. As soon as the harvested energy charges up the supercapacitor, a DC output from the harvester automatically biases the switch's control pin and toggles the switch to connect the antenna to the sensory IC; the system thus switches to the backscattering mode. In this mode, the sensory IC starts its semi-passive operation assisted by the energy from the charged capacitor. With the energy consumed by the sensory IC, the voltage on the supercapacitor decreases. Once it drops below the threshold bias voltage of the switch, the system switches back to the energy-harvesting mode and scavenges the RF energy for the next interrogation cycle. As the duty cycle starts, the RFID reader can intermittently interrogate the sensor system for the remote-sensing information.

4.1.2 Measurement Results and Discussion

To validate this idea, the author built the prototype of the proposed sensor platform, which is shown in Figure 5b. The sensory IC and the RF switch were soldered on the same PCB board with an L-matching circuit that converts the IC impedance (119-j290 Ω at 866 MHz) to 50 Ohm. To ease the test and debugging, the energy harvester was built on a separate board and connected to the RF switch via an SMA connector. There are two outputs V_{low} and V_{high} from the harvester, and they are connected to the V_{sel} and V_{bat} pins on the mainboard, respectively. V_{sel} is the control pin to toggle the RF switch, and V_{bat} is the power input pin for the sensory IC. The minimum voltage required to toggle the switch is 1 V and the voltage for the IC to

operate in semi-passive mode is 1.5 V. In the wireless measurement, a linearly polarized UHF patch antenna with a gain of 8 dBi was connected to the RFC port. Figure 6a shows the setup of the wireless measurement. The author first conducted a response test to verify the operation of the RF switch. In a followed threshold test, the author evaluated the improvement brought by the harvester and tested the sensing functionality.

Response test

In this test, the author measured how long it took to toggle the RF switch and receive the first response from the tag. This test was conducted with the Voyantic Tagformance system [31]. The Tagformance system was controlled to emit a carrier wave at 866 MHz with a constant output power of 20 dBm. With the prototype placed 2 meters away from the reader antenna, it took approximate 90 seconds to get the first response from the sensor. At this point, V_{low} was 1.1 V, and V_{high} reached to 2.1 V.

Threshold test

In this test, the author measured the maximum attainable interrogation distance of the prototype operating in the backscattering mode. Figure 6b compares the distances with and without the external power from the energy harvester. With the V_{bat} connected to the energy harvester, there is a maximum of 7.5 meters increase of the interrogation distance at 810 MHz; this improvement is due to the increase of the IC sensitivity with additional power from the charged capacitor. The IC's sensing functionality was verified with the ThingMagic M6 reader [32]. Figure 7 shows the results of temperature monitoring with a 4-second sampling interval.

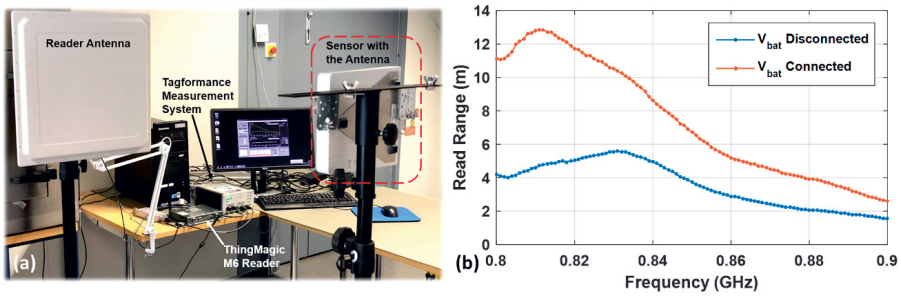

Figure 6. a. Measurement setup b. comparison of the interrogation distances with the V_{bat} connected and disconnected to the harvester output. [Publication V]

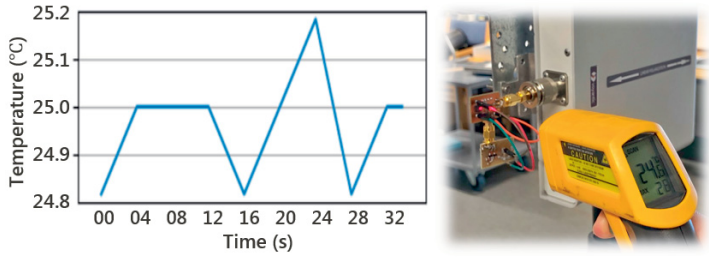

Figure 7. Real-time temperature monitoring with the ThingMagic M6 reader. [Publication V]

According to the results from the tests, the feasibility to enable the semi-passive operation of a sensory IC without the battery was preliminarily verified. By arranging the system to operate in a time divided manner between energy harvesting and RF backscattering, the advantages (e.g. improved interrogation distance, sensing functionality) of the semi-passive operation can be obtained. The costs of this configuration are the prolonged sensing interval and minor increase in the overall sensor size. This proposed platform can be further optimized and utilized in developing the passive wireless sensor system for biomedical applications.

4.2 Performance Evaluation of Human Head Models with Different Geometrical Complexities

The choice of a human body model to evaluate the implantable antenna performance in electromagnetic solvers not only affects the computational efficiency but more importantly determines the accuracy and reliability of the simulation results. In this subsection, the author evaluates the performance of human head models with different geometrical complexity for intracranial implantable antenna development. The primary purpose of this evaluation is to provide a guideline on model selection in different phases of the implantable antenna development conducted in this thesis.

4.2.1 Head Models and Evaluation Method

Figure 8 shows the evaluated four human head models with their composition and geometrical structures. The 'VHP full' is an anatomical head model obtained from the Visible Human Project [48]. This model contains 15 different tissue types and 58 separate tissue parts. Based on this 'VHP full' model, the author made a simplified

anatomical model with decreased geometrical complexity by keeping only six major tissue types: grey matter, CSF, skull (cancellous bone), muscle, fat and skin. To further reduce the model complexity, the author made a semi-anatomical model by substituting the anatomical model's cranial cavity with a six-layer ellipsoid. The structure of the six-layer ellipsoid was built as ellipsoid shells with an adjustable thickness representing skin, fat, muscle, skull, CSF and grey matter. The thickness of each layer was set according to the measurement from the implant location of the VHP model. The model with the least anatomical complexity is a six-layer rectangular cuboid model with a dimension of 30 cm × 30 cm × 20 cm. This cuboid model has the same layer structure as that of the ellipsoid one, but all the layers are in a flat form. The dielectric properties assigned to each tissue type are obtained from the open-source database provided by the IT'IS foundation [45].

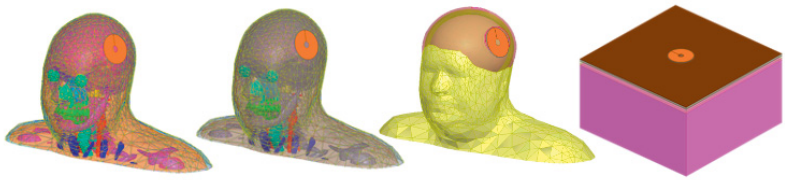

	VHP Full	VHP Simplified	Layered Ellipsoid	Layered Block
Components	15 individual tissues and 58 separate tissue parts	six major tissue layer - skin, fat, muscle, skull, CSF and Grey Matter	six major tissue layer - skin, fat, muscle, skull, CSF and Grey Matter	six major tissue layer skin, fat, muscle, skull, CSF and Grey Matter
Layer Structure	Original medical image based	Original medical image based	Six-layer ellipsoid replacing the cranial cavity	Six flat block layers 30 cm × 30 cm × 20 cm

Figure 8. Comparison of the evaluated four head models.

A multimodal spatially distributed implantable antenna is selected in this model evaluation. Figure 9 shows the antenna dimensions and its implementation with the head model. This antenna is developed for intracranial RFID backscattering system, and its detailed information regarding the antenna development and performance is discussed in Section 4.3.

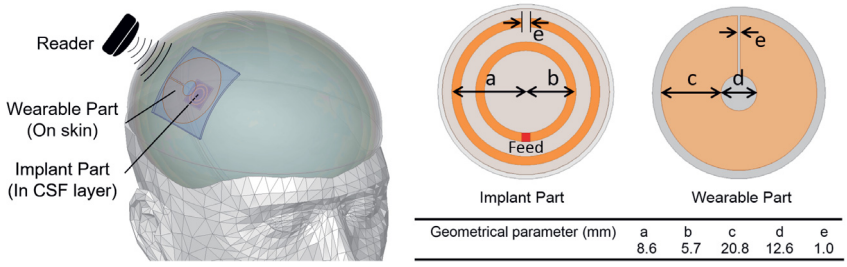

Figure 9. Antenna under evaluation with its geometrical dimensions. [Publication VI]

In this model evaluation, the selected antenna was placed at the identical position in the head models with its implantable part placed in the CSF layer and the wearable part affixed on the skin tissue layer. The full-wave electromagnetic solver ANSYS HFSS v.17 is utilized to calculate the antenna parameters when implanted in the four head models. The antenna parameters selected to evaluate the model performance are radiation efficiency (e_r), antenna directivity (D) and power transfer efficiency (τ). In the simulation, to obtain a good convergence of the results, the change of the simulated τ, e_r, and D in each iteration is monitored. After the sixth iteration, the maximum change in τ, e_r, and D in the four models were less than 0.01%, 0.14% and 0.13%, respectively; and at this point, the solution was considered to reach the convergence.

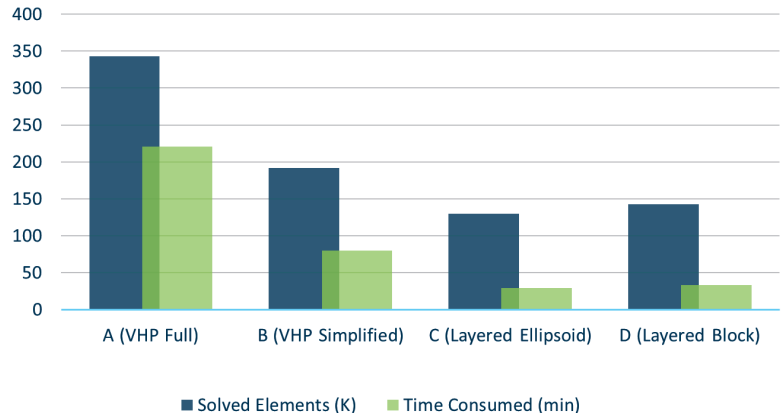

Figure 10. Comparison of the solved elements and simulation time with the four head models.

Figure 10 compares the number of solved elements and the simulation time (mesh generation and solving 15 frequency points) with the four head models at the sixth iteration. Unsurprisingly, the 'VHP full' model with the highest anatomical complexity gives the lowest computational efficiency with a simulation speed more

than six times slower than that of the ellipsoid and cuboid models. It is also noticeable that the simplified VHP model has a considerable reduction in the simulation time. By including only the six major tissue parts, the geometrical complexity is vastly decreased with only about half of the solved elements than that of the 'VHP full' model.

4.2.2 Simulation Results and Discussion

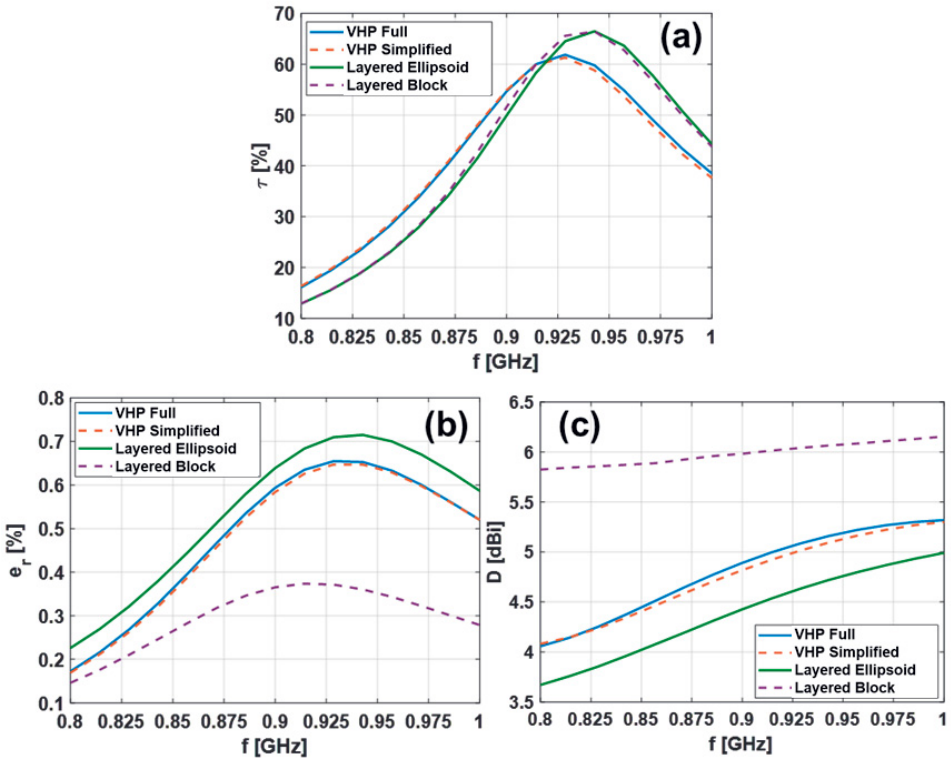

Figure 11. Comparison of the simulated τ, e_r, and D from the four head models. [Publication VI]

The obtained simulation results from the evaluated head models are compared in Figure 11. As the 'VHP full' model contains the most accurate geometrical information of the intracranial environment, it is considered as the reference model to evaluate the rest models. According to the comparison of the power transfer efficiency τ shown in Figure 11a, both the ellipsoid and cuboid models undergo a detuning of the peak frequency from 925 MHz to 942MHz. In contrast, the simplified VHP model has a negligible impact on τ. In the comparison of radiation

efficiency e_r that is shown in Figure 11b, the cuboid model has the worst accuracy. Not only the peak frequency shifts from 925 MHz to 910 MHz, the efficiency level also has a more than 50% underestimation. The ellipsoid model, on the other hand, estimates the peak frequency correctly with only about 10% overestimation of the efficiency level. This overestimation is mainly due to the missing geometrical details on the tissue boundaries. From the comparison shown in Figure 12, the wrinkled tissue boundary is smoothed in the ellipsoid model. The material's boundary structure has a large influence on antenna radiation efficiency; this simplicity explains the inaccurate estimation with the ellipsoid model. In terms of the antenna directivity D shown in Figure 11c, the cuboid model fails to predict its variation trend versus frequency, and the level estimation is 1.5 dB less than that from the 'VHP full' model. On the contrary, the ellipsoid model reflects the variation of D with the frequency, and the difference in level estimation is only 0.5 dB.

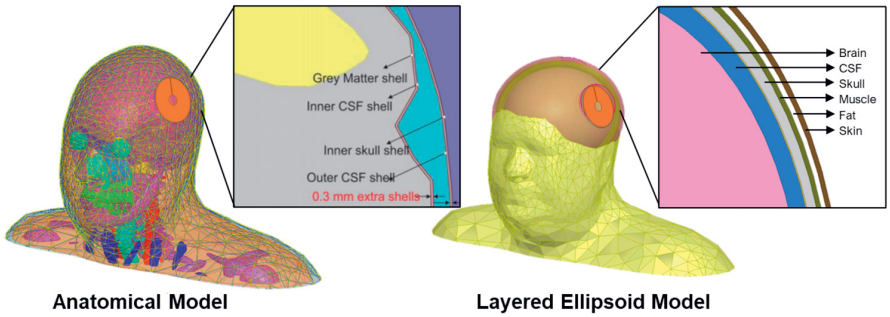

Figure 12. Comparison of the tissue boundaries between anatomical model and ellipsoid model.

Based on the comparison of the simulated antenna parameters, the layered cubic model can accurately estimate the antenna impedance; however, it fails to provide an accurate prediction on antenna far-field parameters. On the contrary, the layered ellipsoid model not only accurately estimates all the antenna parameters but with the least amount of simulation time. The simplified VHP model predicts nearly the identical antenna parameters than that from the 'VHP full' model. For this reason, it is unnecessary to use the full anatomical model as its redundant anatomical complexity largely slows down the computation speed. Instead, a simplified anatomical model that includes only the major tissues parts is recommended to obtain an accurate estimation on antenna performance efficiently. Overall, when developing intracranial implantable antennas, layered ellipsoid model, due to its high computational efficiency and the adjustable layer thickness, is a good option for preliminary antenna optimization and evaluation of the antenna robustness towards

tissue structure variation. The anatomical model with a simplified structure is more suitable for final verifications of the antenna performance.

4.3 Spatially Distributed Implantable RFID Antenna System

As discussed in Subsection 2.2.3, the major challenge in developing antennas for wireless implantable devices is the strict requirements on antenna form-factor and geometrical dimensions. In contrast, these physical constraints become less stringent if the antennas become non-invasive, such as the wearable antennas. Taking advantage of this fact, the author developed a spatially distributed antenna system with a small implant part carrying the RFID microsystem and an inductively coupled wearable part to improve the system radiation efficiency for wireless brain care applications [Publication I].

4.3.1 Antenna Configuration

Figure 13 demonstrates the prototyped antenna system with its geometric dimensions. Its implementation in the human head is illustrated with the layered semi-anatomical head model. The wearable part of the developed system is affixed to the scalp with the ethylene propylene diene monomer (EPDM) ($\varepsilon_r = 1.26$, $\tan\delta = 0.007$ at 915 MHz) as the substrate to avoid the antenna conductor directly contacting the skin tissue. The split-ring-resonator inspired implant part is concentrically placed in the CSF tissue layer. The substrate for this implant part is the flexible polyimide ($\varepsilon_r = 2.25$, $\tan\delta = 0.001$ at 915 MHz) with a thickness of 50 μm. The selected RFID IC for antenna evaluation is the NXP UCODE G2iL IC with a P_{th} of -18 dBm; this IC is attached to the split of the implant part's inner ring using the conductive epoxy - Circuit Works CW2400. In this work, silicone (ε_r=2.2, $\tan\delta$=0.007 at 915 MHz) was used as the insulation material for the implant part. In consideration of the balance between the overall implant size and the insulation effect in the lossy tissue environment, the thickness of the silicone coating was set to be 1 mm.

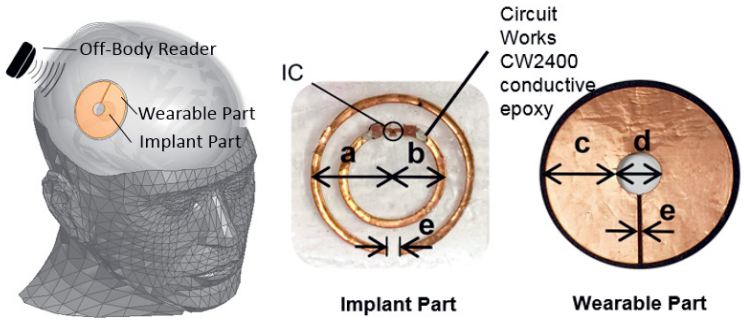

Geometrical parameter (mm)	a	b	c	d	e
	8.6	5.7	20.8	12.6	1.0

Figure 13. Prototyped antenna with its geometric dimensions and implementation with the human head model. [Publication I]

The antenna simulation and optimization were conducted with the HFSS V.17. In the simulation, the RFID IC was modeled as the shunted capacitance and resistance of 0.91 pF and 2.85 kΩ, respectively [69]. Meanwhile, the seven-layer ellipsoid was built to simulate the human head environment. Figure 14 shows the layered structure of the head model in detail. The tissue dielectric properties were obtained from the database provided by the IT'IS Foundation [45]. Among the seven major layers of the human head, the thicknesses of CSF and skull tissue layers largely depend on the locations of the head. In the antenna optimization phase, the thicknesses for the skull and CSF layer were set to 5.2 mm and 4.9 mm, respectively. In Subsection 4.3.4.2, the influences of the thickness of these two layers are further investigated.

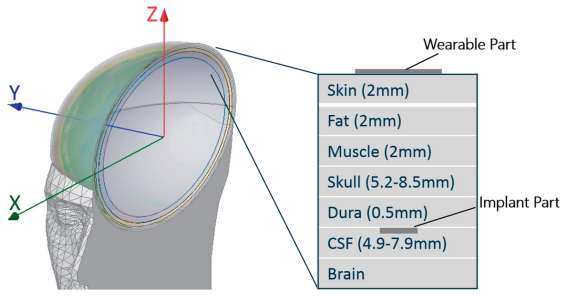

Figure 14. Layered structure of the ellipsoid head model. [Publication I]

4.3.2 Simulation and Measurement Results

As discussed in Section 2.1.2, the read range of an RFID system is the most comprehensive parameter in evaluating system performance. Since the read range is proportional to the antenna radiation efficiency, directivity, and the goodness of the conjugate impedance matching between the antenna and the IC, it is worthwhile to investigate how the antenna geometrical structure influences these antenna parameters.

The author first found that the passive head-worn part has minor influence on antenna input impedance but quite significantly influences the antenna radiation efficiency and directivity. To demonstrate this impact, the author compared the magnitude of the radiated **E** field with and without the wearable part in Figure 15.

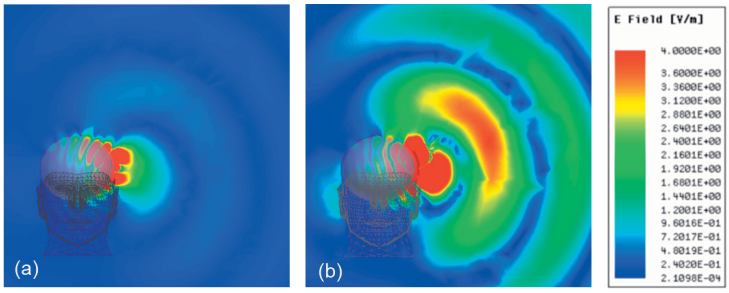

Figure 15. Comparison of the radiated **E** field. (a) without the wearable part (b) with the wearable part.

According to this comparison, the wearable part boosts the strength of the radiated **E** field up to 5 times in the antenna's far-field. As a result, the wearable part improves the maximum antenna gain from -35 dBi (without the wearable part) to -18 dBi (with the wearable part) with a 17 dB improvement. The comparison of the 2D antenna radiation pattern with and without the wearable part is shown in Figure 16. This improvement of the antenna gain is mainly brought by the relatively large electrical size of the wearable part and the strong magnetic coupling between the two parts. More specifically, the implant part is a magnetically excited radiator which has a dominant magnetic field in its near field, and the close distance between the wearable part and the implantable part ensures a strong magnetic coupling between the two. Since the human tissue is non-magnetic, the energy can be efficiently coupled through the magnetic field from the implant part to the wearable part. Finally, the wearable part is excited by this coupled energy, since the wearable part is no longer inside the lossy tissue environment, it can radiate with higher efficiency.

A closer look of the magnetic field between the implant part and the wearable part is illustrated in Figure 17. A strong coupled magnetic field can be observed near the wearable part.

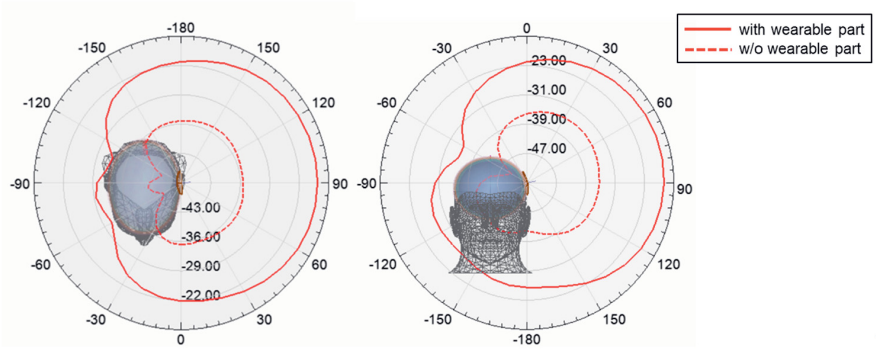

Figure 16. Comparison of 2D radiation pattern (antenna gain in dBi) with and without the wearable part.

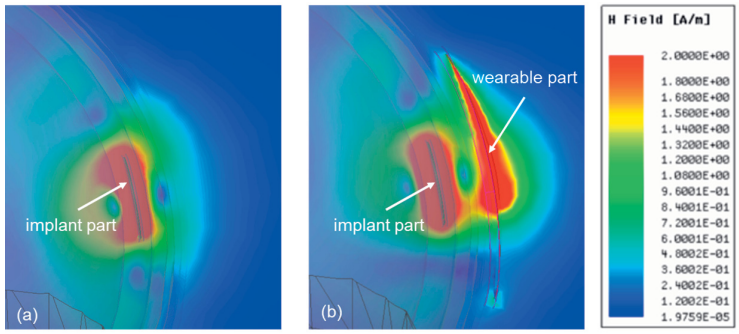

Figure 17. Comparison of the magnetic field (a) without the wearable part (b) with the wearable part.

In terms of the complex conjugate impedance matching, the split ring structure inherently provides a favorable inductive impedance. By adjusting the radius of the two rings, the input impedance of the antenna can be tuned to be close to the complex conjugate value of the IC impedance to maximize the power transfer efficiency τ given in Equation 2.2. Figure 18 compares the optimized antenna input impedance with the IC impedance along with the calculated power transfer efficiency τ. In the UHF band, the maximum power transfer efficiency reaches 74% at 915 MHz.

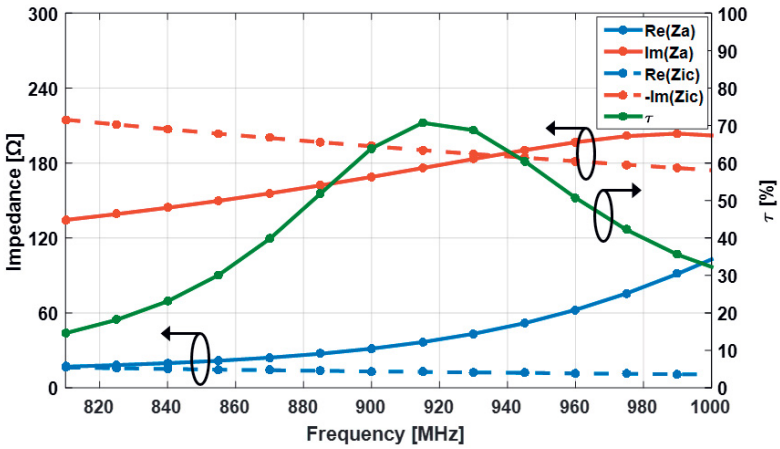

Figure 18. Impedance comparison of the antenna and IC, and the calculated power transfer efficiency. [Publication I]

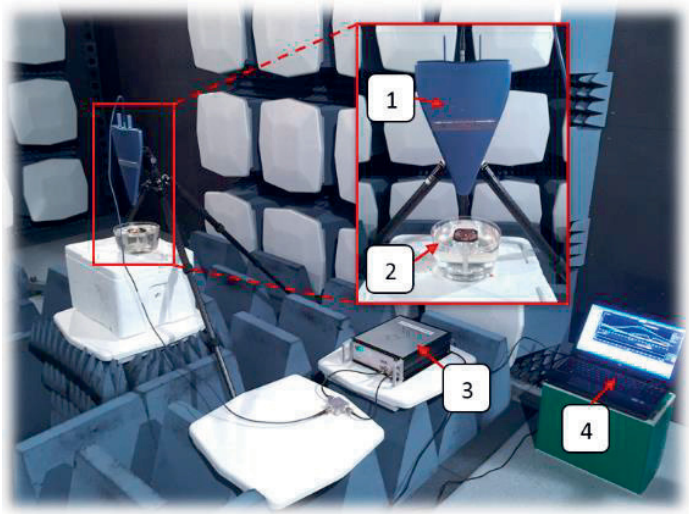

Figure 19. Measurement setup 1: Reader antenna 2: Prototyped antenna system with the implantable part submerged in the liquid phantom 3 and 4: Tagformance measurement system. [Publication I]

The antenna prototype was tested with the Tagformance system [31] in an anechoic chamber. The phantom liquid mixed with sugar, salt and water was made to simulate the lossy environment [70]. The dielectric properties of the liquid were adjusted in accordance with the FCC guideline for 'average head' with a conductivity and relative permittivity of 0.77 S/m and 45.74, respectively at 915 MHz [71]. The measurement setup is showed in Figure 19. In the wireless measurement, the read

ranges were successively measured with the implant part immersed in the liquid phantom at three different depths: 15 mm, 10 mm and 5 mm. In the simulation, a liquid phantom with the same geometrical dimension and dielectric properties was made for reference. Figure 20 compares the simulated and measured theoretical maximum read ranges with the three depths. With the increase of depth, the read range becomes shorter. This is mainly due to the weakened magnetic coupling between the two parts, which caused by the increased submerged depth. However, even at 15 mm depth, there is still more than 0.8-meter read range in the wireless measurement.

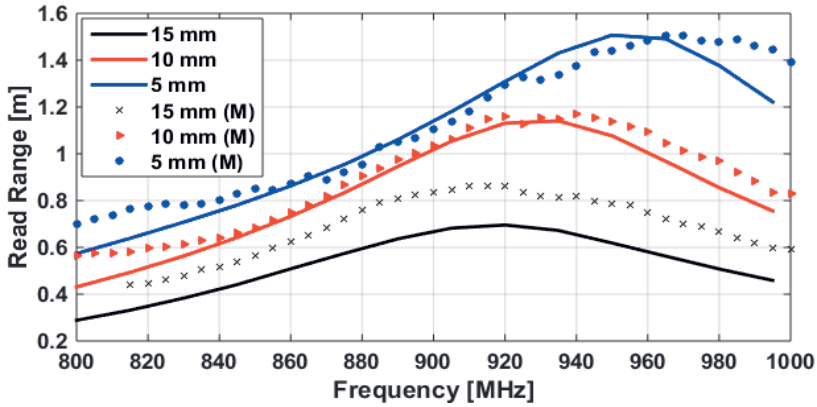

Figure 20. Comparison of the maximum attainable read ranges with different implant depths in simulation and wireless measurement with tissue-mimicking liquid. [Publication I]

4.3.3 Realization of Circular Polarization with Modified Wearable Part

In the wireless measurement, the author found the polarization of the proposed antenna system is approximately linear in the direction orthogonal to the split on the wearable part. Meanwhile, the wearable part has been proved to have a significant influence on the radiated **E** field (see Figure 15). Inspired by these facts, the author realized the circular polarization of the proposed antenna with a modified wearable part [Publication VII].

Figure 21a shows the geometrical structure of the modified wearable part. The main purpose of this modification is to have a pair of orthogonal dipoles connected to a centered split ring. The lengths of the dipoles and the connection positions were adjusted to ensure the resonance of the two dipoles is at the same frequency but with a phase shift of 90° between each other. By doing so, the circular polarization is

realized. The optimized geometrical parameters of the modified wearable part are obtained with the HFSS optimization tools as follows: $R_1 = 75°$, $R_2 = 85°$, $R_3 = 75°$, $R_4 = 25°$, $L_1 = 18$ mm, $L_2 = 20$ mm, $L_3 = 5.5$ mm, $L_4 = 4.5$ mm, $L_5 = 12$ mm and $w = 1$ mm.

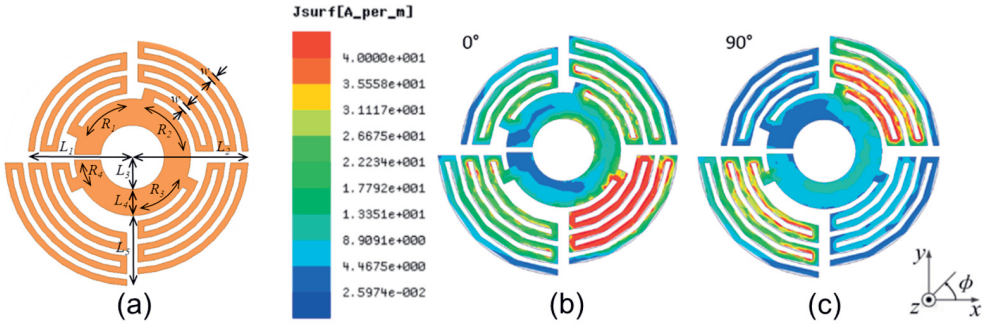

Figure 21. Modified wearable part and the surface current distribution with different phase at 915 MHz. [Publication VII]

Figure 21b and 21c demonstrate the simulated surface current distribution of the modified wearable part. With a phase of 0°, the dipole along $\varphi = 135°$ resonates and when the phase changes to 90°, the resonance shifts to the dipole along $\varphi = 45°$. This configuration excites an LHCP in the far-field of the proposed antenna. Figure 22 compares the measured and simulated axial ratio (AR), both the measured and simulated AR drops below 3 dB in the UHF RFID band. The advantages of the CP operation are the improved link efficiency and reliability, which are both favorable in wireless biomedical applications.

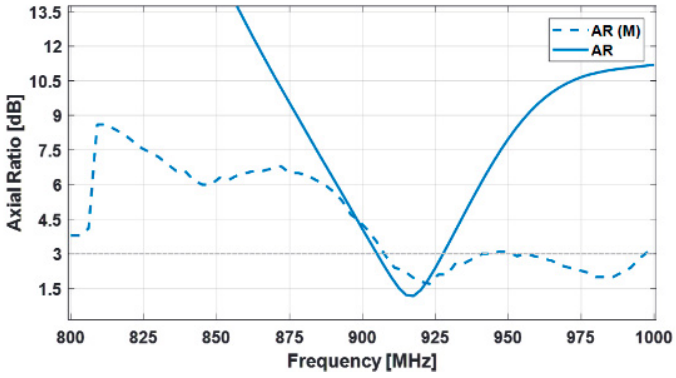

Figure 22. Comparison of the measured and simulated axial ratio. [Publication VII]

4.3.4 Robustness Evaluation in Semi-Anatomical Head Model

In practice, the implant site of wireless brain care devices can hardly be fixed into a specific region; instead, it highly depends on application scenarios. Thus, it is crucial to evaluate the antenna performance at different implant locations of the head. Meanwhile, the tissue thickness varies from different individuals; the implantable antenna must be robust towards these anatomical variabilities. To further verify the applicability of the proposed antenna, the author conducted the robustness evaluation of the antenna system towards these factors with the semi-anatomical head model discussed in Subsection 4.2 [Publication III].

4.3.4.1 Impact of Implant Location on Antenna RF Performance

In this evaluation, the author selected six different locations on the human head: the parietal posterior (PP), frontal anterior (FA), parietal anterior (PA) with upper and lower positions and frontal posterior (FP) with upper and lower positions. Figure 23 illustrates these locations on the head model. The thicknesses for each tissue layer at different locations are listed in Table 1. This geometrical information is obtained from published empirical results [72] and our measurement of anatomical head models [47].

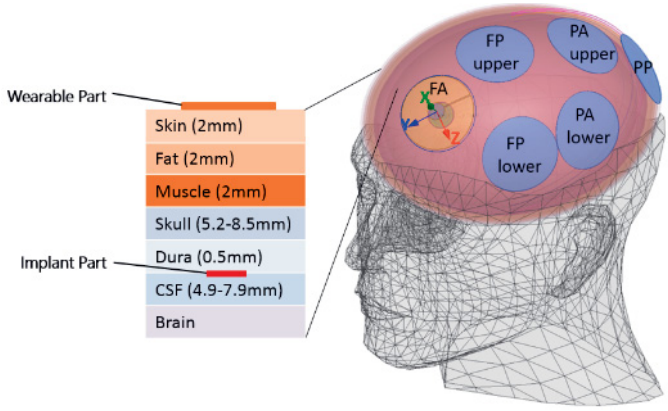

Figure 23. Semi-anatomical head model with the selected six evaluation locations. [Publication III]

Table 1. Tissue thickness at different locations of the head model [mm]. [Publication III]

Tissue \ Position	FA	FP	PA	PP
Skin	2	2	2	2
Fat	2	2	2	2
Muscle	2	2	2	2
Skull	5.2	4.0	3.9	8.5
Dura	0.5	0.5	0.5	0.5
CSF	6.1	7.2	7.9	4.9

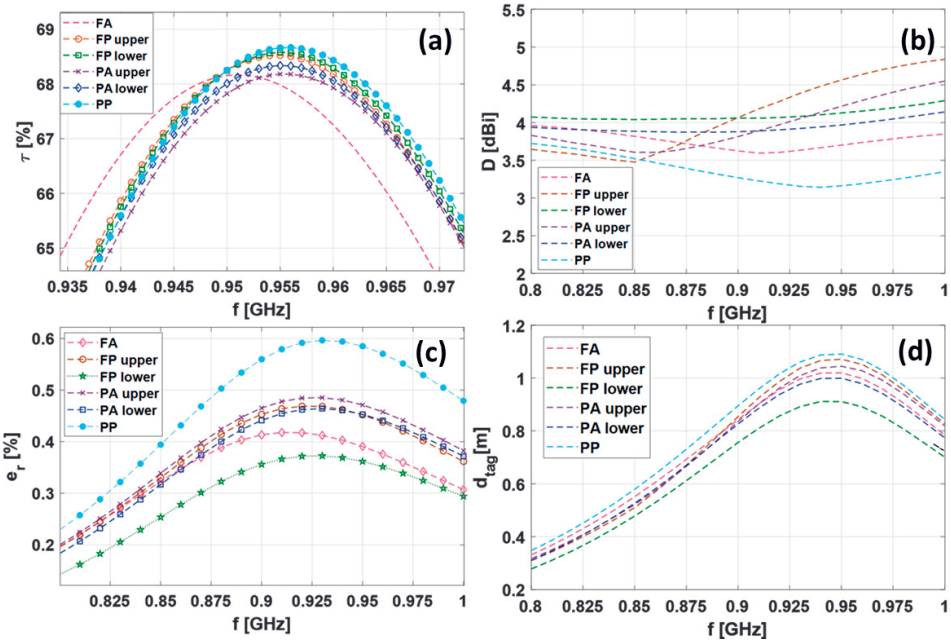

Figure 24. Comparison of the antenna parameters at different locations. [Publication III]

For each selected location, the author compared the power transfer efficiency τ, directivity D and radiation efficiency e_r of the implantable antenna. Figure 24a compares τ with the antenna placed at different locations. The results indicate that the variation of the implant location has a minor influence on antenna impedance. This is because the impedance of the antenna is mainly determined by the closest surrounding tissues, which is the CSF in all the evaluated positions [Publication VI]. The comparison results of the antenna directivity are shown in Figure 24b. The variation of the antenna directivity caused by the location change is relatively smaller than that observed in the radiation efficiency. The maximum variation of directivity in the whole frequency range is about 1.5 dB. The comparison of the antenna

radiation efficiency at different locations is given in Figure 24c. The variation of the location brings a noticeable level shift in antenna radiation efficiency; however, it does not affect the peak frequency. The PP location with the smallest thickness of the CSF layer has the highest efficiency of 0.6% at 925 MHz. The lowest efficiency of 0.38% is obtained at location FP lower with an approximate 50 percent drop than the highest one. Based on the simulated τ, e_r and D, the author calculated the theoretical maximum read range d_{tag} of the tag (antenna with the RFID IC) with Equation 2.6. Figure 24d shows the comparison results. The maximum d_{tag} varies from the minimum 0.9 m to 1.1 m around 930 MHz at different locations.

The variation of implant location has a relatively larger impact on e_r and D and limited influence on τ. Nonetheless, the proposed antenna shows good robustness towards the variation of the implant locations. A simulated maximum read range of more than 0.9 m is maintained at the six evaluated positions.

4.3.4.2 Impact of Thickness Variation of CSF and Skull Tissue Layers on Antenna EM Performance

To evaluate the antenna performance towards the anatomical variability, the author set the thicknesses of the most variable skull and CSF layers with a wider range that covers the corresponding thickness intervals shown in Figure 23.

First, the thicknesses of all the tissue layers were set to the corresponding values of the PA lower location (see Table 1), then the thickness of the skull layer was increased from 3 mm to 13 mm with a step of 2 mm. As shown in Figure 25, the increase of the skull thickness notably decreases D, e_r and d_{tag}. When the thickness reaches 10 mm, the read range decreases to less than 0.5 m. This is because the increase of the skull layer leads to a larger separation between the implant and wearable part. The increased separation deteriorates the magnetic coupling between the two parts and overall worsens the antenna EM performance.

The evaluation of the CSF tissue thickness was conducted in a similar manner, where the author changed its thickness from 2.5 mm to 12.5 mm with a step of 2 mm. In the meantime, the thicknesses of other tissue layers were fixed to the values of the PA lower location. The evaluation results are presented in Figure 26. A similar inverse relation between D and the layer thickness can be observed, even though the change is much smaller than that with the skull tissue layer. The e_r also experiences a decreased trend with the increase of the CSF thickness; however, this is mainly due to the increased tissue dissipation in the high lossy CSF tissue layer. Overall, even in

the extreme case with a thickness of 12.5 mm, the simulated maximum read range still maintains about 1 meter.

Generally, the proposed antenna has nearly consistent EM performance at the six evaluated locations that cover most of the possible antenna placements on the human head. Moreover, the antenna system shows decent robustness towards the thickness variation of the skull and CSF tissue layers.

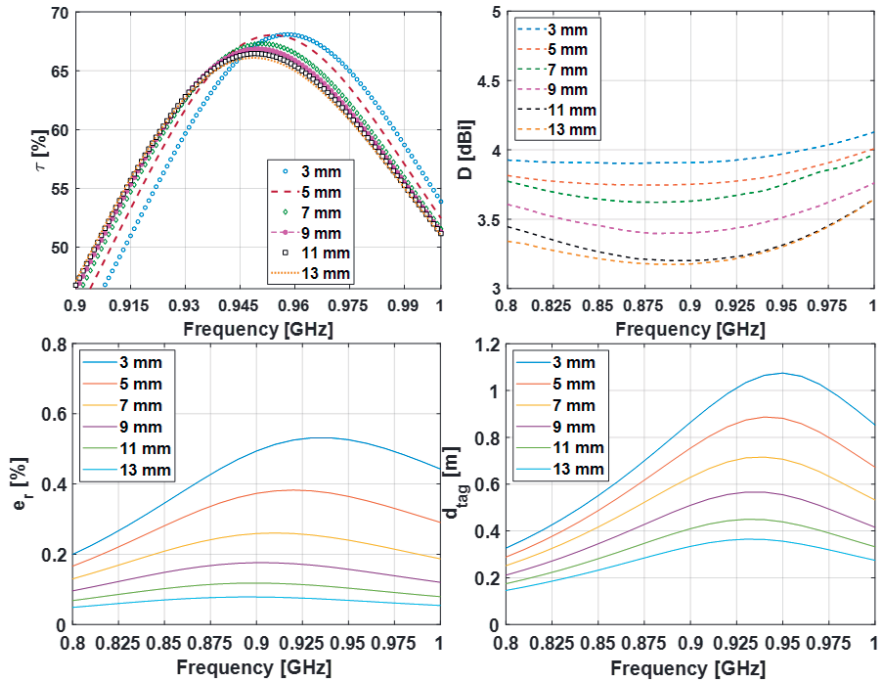

Figure 25. Comparison of antenna parameters with different thicknesses of skull layer. [Publication III]

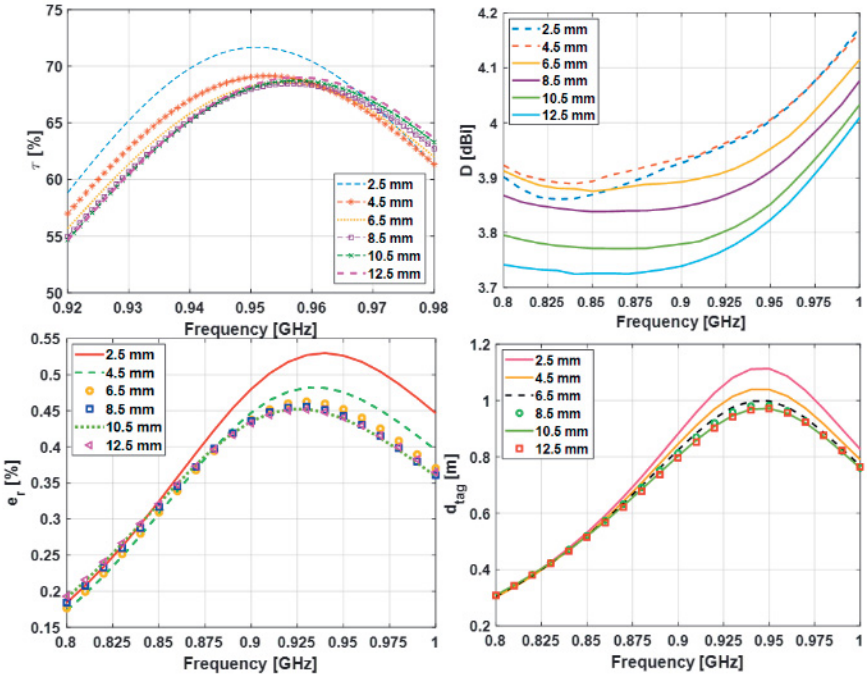

Figure 26. Comparison of antenna parameters with different thicknesses of CSF layer. [Publication III]

4.4 Double Split Rings as Extremely Small Implantable Antenna with Readily Tunable Impedance

As discussed in Section 2.2, the magnetically excited radiator possesses inherent high radiation efficiency in a lossy medium. Utilizing this advantage, the author developed a miniature implantable antenna with solely a pair of split copper rings [Publication II]. Based on the proposed configuration, the overall volume of the implantable antenna can be decreased to as small as $\pi \times (3 \times 1.5) \times 1$ mm^3 and the maximum antenna gain maintains a level around -25 dBi with an implant depth of 16 mm in the CSF tissue layer. Moreover, the input impedance of the antenna can be readily adjusted to achieve the complex conjugate matching to a wide range of capacitive impedance of the passive microsystems with built-in energy harvester. Figure 27 shows the antenna structure and its implementation with the HFSS anatomical head model.

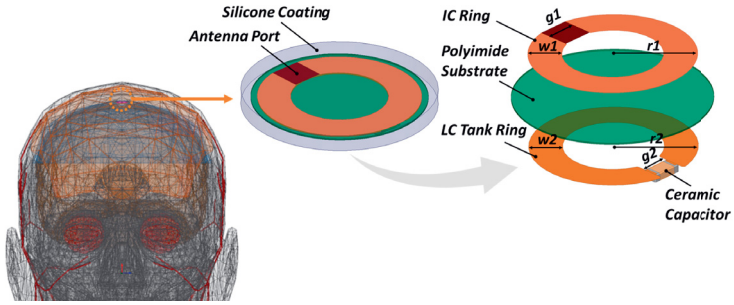

Figure 27. Antenna structure and its implementation with the anatomical head model. [Publication II]

4.4.1 Antenna Configuration and Tunable Input Impedance

The proposed antenna consists of an IC ring and an LC tank ring. The antenna port is located at the split terminals of the IC ring. A lumped capacitor with a capacitance of C_s is connected to the terminals of the LC ring. The two rings are placed concentrically on the top and bottom surfaces of the polyethylene substrate (ε_r=2.25, tanδ=0.001 at 915 MHz), respectively. The thickness of the substrate is 0.05 mm and the outer radiuses of the IC ring and the LC tank ring are denoted as r_1 and r_2, respectively.

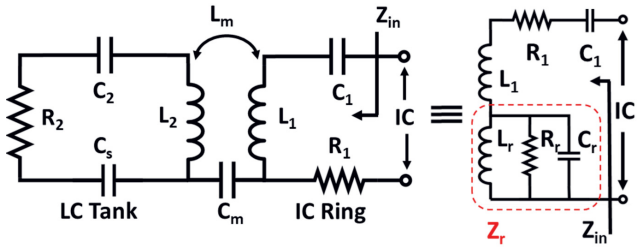

Figure 28. Equivalent circuit model of the proposed antenna. [Publication II]

The tunable input impedance of the proposed antenna is realized by adjusting the mutual coupling between the two rings and the capacitance of the lumped capacitor. Based on the reflected load theory [23] and the equivalent circuit of the antenna shown in Figure 28, the antenna input impedance can be calculated as,

$$Z_{in} = R_1 + j\omega L_1 + \frac{1}{j\omega C_1} + Z_r \tag{4.1}$$

$$where, Z_r = \frac{\omega^2 M^2}{j\omega L_2 - \frac{j}{\omega}(\frac{1}{C_2} + \frac{1}{C_s}) + R_2}. \quad (4.2)$$

Here, L, C and R are the inductance, parasitic capacitance, and parasitic resistance of the split rings, with its subscript 1 and 2 denoting the IC ring and LC ring, respectively. The M stands for the equivalent mutual inductance that represents the mixed coupling of mutual inductance L_m and the mutual capacitance C_m between the two rings [73]. In Equation 4.1, except the C_s from the lumped capacitor, the rest parameters are dominated by the geometrical structure of the two copper rings [74-76]. To find out the relation between the antenna geometrical dimensions and its input impedance in the lossy tissue environment, the author built the antenna model in the HFSS and conducted a parametric analysis including all the antenna geometrical parameters. Based on the conclusion from Section 4.2 that the homogeneous model is computationally adequate for antenna impedance evaluation. A homogeneous tissue cube (ε_r=41.5, σ=0.77 S/m at 915 MHz) with a side-length of 10 cm was built to simulate the tissue environment. According to the results from this analysis, the author found that the difference between r_1 and r_2, and C_s had the dominant influence on the antenna input impedance. To facilitate the prototype fabrication, $w_{1(2)}$ and $g_{1(2)}$ were set to 1 mm. Figure 29 presents the attainable antenna input impedance with r_1 fixed to 3 mm while r_2 varies from 3 mm to 5 mm with a step of 0.25 mm. In each combination of r_1 and r_2, C_s sweeps from 0.5 pF to 1 pF with a step of 0.1 pF. The shadowed area in Figure 29 denotes the range of the attainable antenna input impedance at 915 MHz. This wide impedance range covers typical values to obtain good complex conjugate impedance matching with most of the capacitive microsystems with an energy harvester. Importantly, the variation of r_2 and C_s in the evaluated ranges have minor impact on antenna gain [Publication II]. This feature provides the possibility to adjust the antenna impedance without deteriorating the antenna far-field performance.

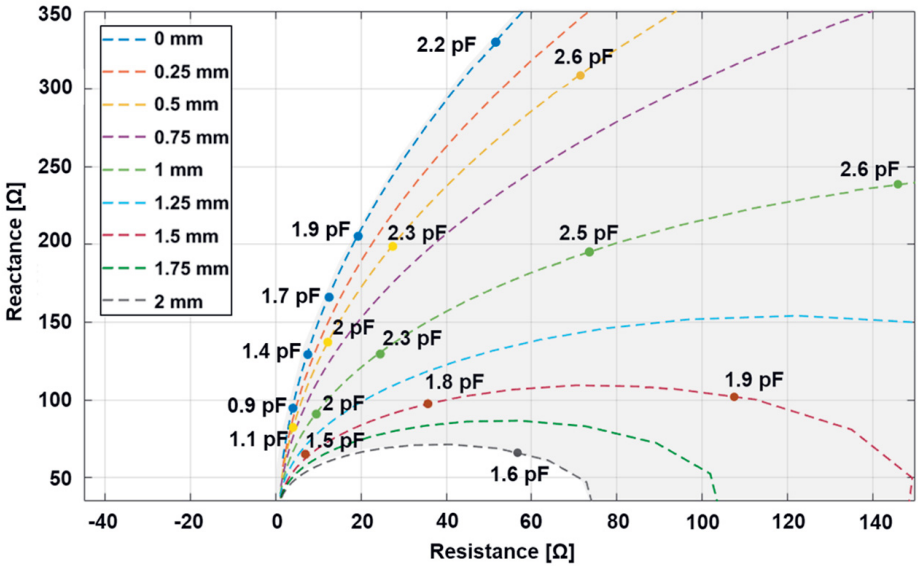

Figure 29. Antenna input impedance with the variation of r_2-r_1 and C_s. [Publication II]

4.4.2 Evaluation of Proposed Antenna Design Method

To evaluate the performance of the proposed antenna in wireless measurement, the author adapted the antenna to build implantable RFID tags with the NXP UCODE G2iL RFID IC. The IC is modeled with the same equivalent circuit adopted in Section 4.3. The HFSS anatomical head model with 15 individual tissue types and 58 separate tissue parts was utilized to simulate the tissue environment. All the tissues' dielectric properties were obtained from the database provided by the IT'IS foundation [45].

The antenna implementation is initiated by setting the initial values of 3 mm and 1.9 pF for r_2 and C_s, respectively. This combination is made based on the impedance lines in Figure 29, where the impedance of the antenna with the selected values is very close to the conjugate values of the IC impedance. As shown in Figure 30, the antenna is placed horizontally in the CSF tissue layer at an implant depth of 16 mm. The HFSS optimization tool is used to further optimize the combination of r_2 and C_s that maximizes the power transfer efficiency τ defined in Equation 2.2. As a result of this optimization process, the obtained optimal values for r_2 and C_s are 3 mm and 1.8 pF, respectively. Figure 31a compares the impedances of the obtained antenna (dash lines) and the IC (solid lines). The antenna impedance achieves a good complex

conjugate impedance matching with that of the IC at 915 MHz. The corresponding power transfer efficiency τ reaches 94 %.

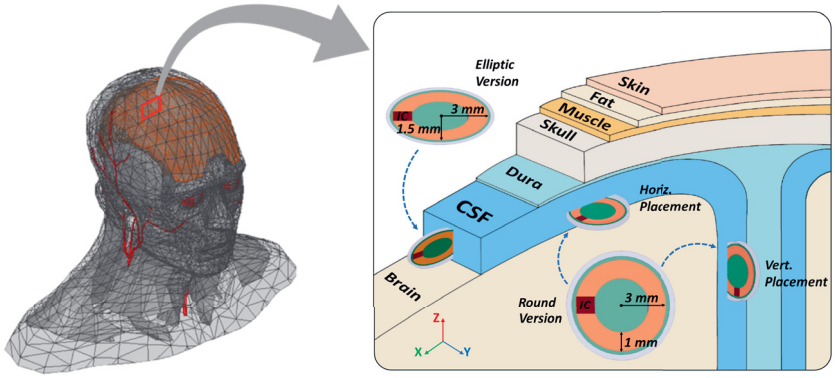

Figure 30. Proposed antennas with horizontal and vertical placements in a simplified cross-sectional view of the anatomical model. [Publication II]

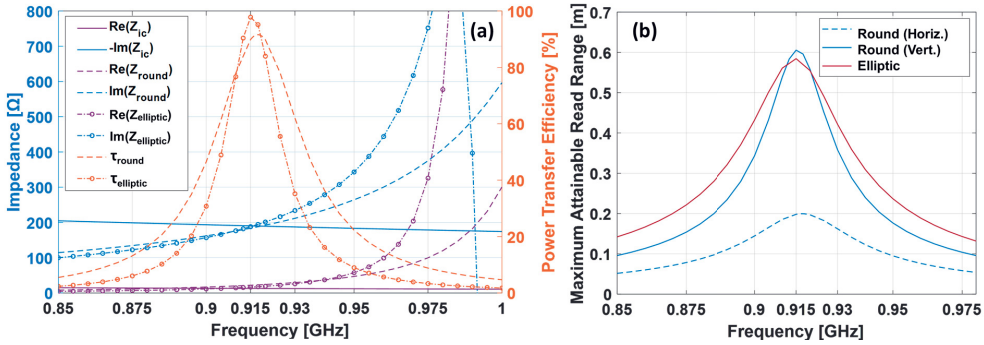

Figure 31. a. Comparison of the simulated power transfer efficiency and the impedance of antennas and the IC. b. Comparison of the simulated maximum attainable read ranges of the antennas with different placements. [Publication II]

4.4.2.1 Effect of Antenna Placements on Radiation Efficiency and Directivity

When evaluating the antenna gain in the anatomical model, the author found the antenna placement relative to the tissue boundaries had a considerable impact on antenna radiation efficiency. The antenna in horizontal placement has the radiation efficiency and the maximum directivity of 0.01 % and 4.36 dBi, respectively. The corresponding maximum antenna gain is -35.6 dBi at 915 MHz. In contrast, with a

vertical placement, the efficiency improves ten times higher to 0.13 %, and the maximum antenna gain reaches -24.9 dBi. Figure 32 and 33 show the antenna radiation patterns with horizontal and vertical placements, respectively at 915 MHz.

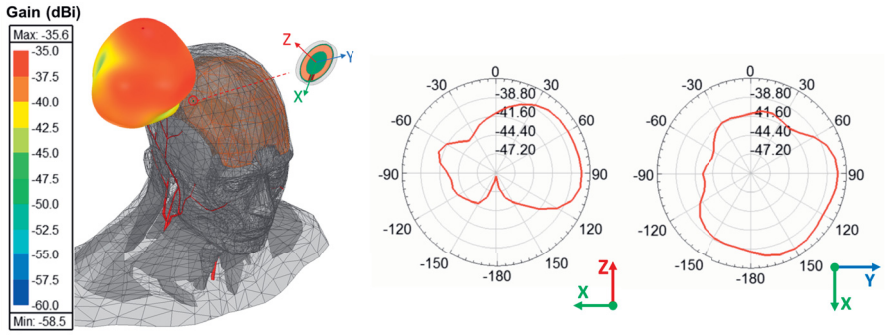

Figure 32. Simulated 3D and 2D radiation patterns of the antenna in horizontal placement at 915 MHz. [Publication II]

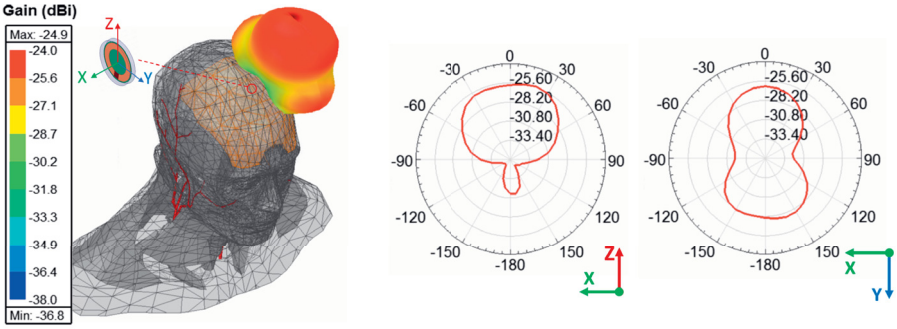

Figure 33. Simulated 3D and 2D radiation patterns of the antenna in vertical placement at 915 MHz. [Publication II]

Figure 31b compares the maximum attainable read range of the tags with different placements. In horizontal placement, due to the relatively low radiation efficiency, the read range is 0.2 m. With vertical placement, the read range increases to 0.6 m.

The reason for the efficiency improvement in vertical placement is due to the decreased reflection losses on the tissue boundaries and the tissue absorption losses that discussed in Subsection 2.2.2. More specifically, the reflection losses highly depend on the incident angle of the radiated wave relative to the boundaries. It decreases to the minimum when the antenna's radiated **E** field is orthogonal to the boundaries of different tissues [34]. In terms of the tissue absorption losses, in the

vertical placement, the main lobe of the antenna points towards the tissues with a relatively smaller thickness than that in the horizontal placement. The decrease of the tissue thickness results in a lower absorption loss. As a result, the antenna in vertical placement offers a higher radiation efficiency. Figure 34 compares the strength of the radiated **E** field of the antenna in a horizontal and vertical placement. In the horizontal placement, the antenna excites the surface wave on the tissue-air boundary, and thus the radiated **E** field in the antenna far-field is weak. When the antenna is placed vertically, there is a notable boost of the radiated field density in the antenna far-field.

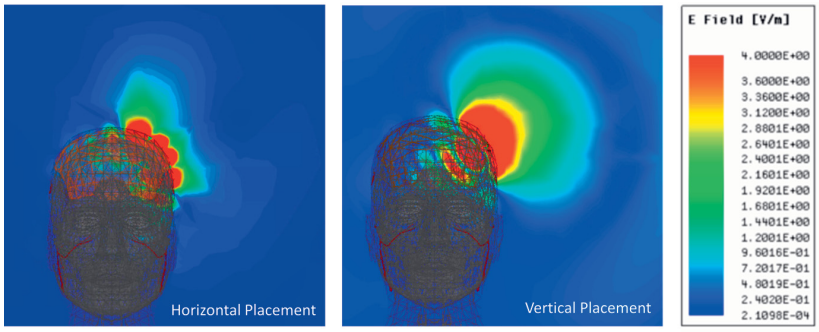

Figure 34. Comparison of the radiated **E** field of the antenna in horizontal and vertical placements.

It is worth mentioning that the CSF tissue thickness varies from different locations on the human head with a typical range from 2 mm to 8 mm [77-78]. As illustrated in Figure 30, when the outer radius of the antenna equals to 3 mm, the thickness of the antenna in vertical placement reaches 6 mm and the only region of the CSF layer that can host this large thickness is the location near the longitudinal fissure. In practice, the implant location of brain care devices can hardly be fixed into a particular region, and it is thus necessary to further downsize the antenna to release the constraint of implant sites on the head.

4.4.2.2 Improvement of Antenna Applicability with Elliptic Version

To decrease the antenna dimension for better antenna applicability, an elliptic version is developed by assigning a 50% aspect ratio to the two circular rings of the original antenna. As shown in Figure 30, the thickness of the elliptic antenna in vertical placement drops to 3 mm. Since the size difference between the two rings remains unchanged, it is only needed to tune the capacitance value C_s of the lumped

capacitor to achieve the complex conjugate impedance matching between the antenna and the IC. With the help of the optimization tool provided by HFSS, the obtained optimal value for C_s is 3.9 pF.

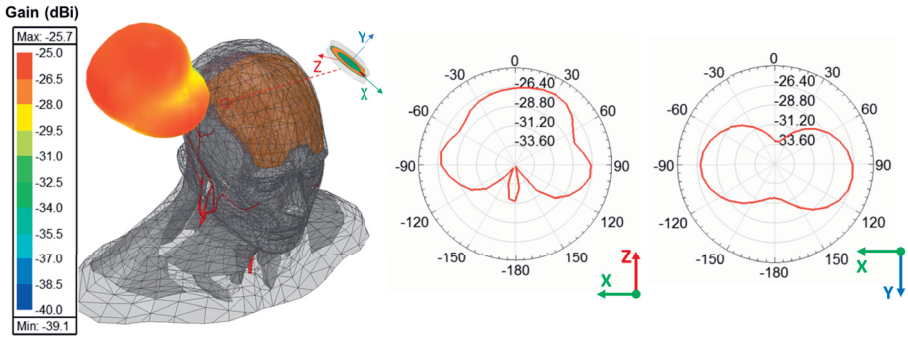

Figure 35. Simulated 3D and 2D radiation patterns of the elliptic antenna in vertical placement. [Publication II]

The impedance of the elliptic antenna is shown in Figure 31b with the dot-dash lines. The peak value of τ reaches 98 % at 915 MHz. With an implant depth of 16 mm, the simulated radiation efficiency of the elliptic antenna is 0.12 %, and the maximum directivity is 3.4 dBi. Figure 35 illustrates the corresponding radiation patterns where the maximum antenna gain reaches -25.7 dBi with the direction pointing outwards the human head. The estimated maximum attainable read range is shown in Figure 31b with a maximum value of 0.6 m near 915 MHz.

4.4.2.3 Antenna Robustness towards Bending Distortion

Since the antenna substrate is flexible, the antenna may experience bending distortion in the complex tissue environment. To evaluate the antenna performance under such distortion, the author chose three levels of bending of the proposed antenna. Figure 36 shows the cross-sectional view of the round antenna with the three levels of bending. To ease the comparison of the impact on the antenna impedance, the author compared the power transfer efficiency between the antenna and the IC.

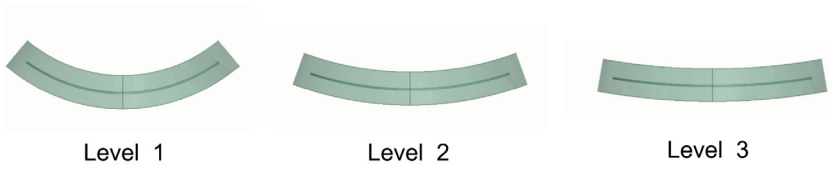

Figure 36. Cross-sectional view of the antenna with different bending levels.

According to the results shown in Figure 37, except the extreme case of level 1 bending, the moderate bending has only minor impact with slight frequency shifts. With level 1 bending, the power transfer efficiency drops by approximately 1 percent, which is still tolerable from the point of view of the link budget. Moreover, the bending also has a negligible impact on the antenna radiation pattern. Figure 38 compares the **E** plane and **H** plane of the radiation pattern with and without the level 1 bending; the maximum gain decreases only 0.2 dB with the bending. The elliptic antenna also shows a similar insensitivity to the bending of the antenna structure in the evaluation. Overall, the proposed antennas show robustness towards the bending distortion in the tissue environment.

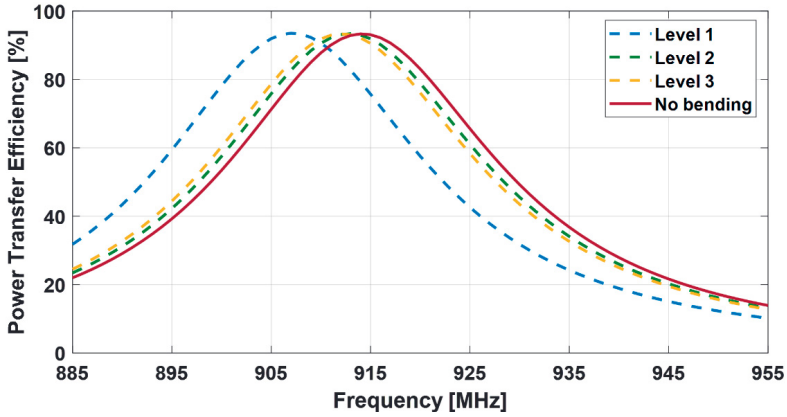

Figure 37. Comparison of antenna power transfer efficiency with different bending levels in anatomical head model.

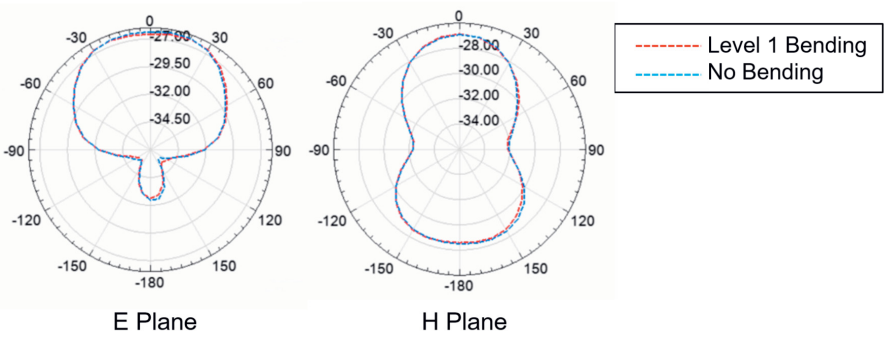

Figure 38. Comparison of antenna radiation pattern with different bending level in anatomical head model.

4.4.3 Antenna Prototypes and Experimental Evaluation

Figure 39a depicts the prototyped round and elliptic tags. The author patterned the split rings using 35 μm thick copper foil (σ = 58 MS/m) with the vinyl cutter. The obtained copper rings were affixed to the top and bottom sides of the polyimide substrate (Kapton 200HN). The IC and the ceramic capacitor were soldered to the terminals of the IC ring and the LC tank ring, respectively. The antenna insulation material is MED-2000 silicone (ε_r=2.2, tanδ=0.007 at 915 MHz) with a thickness of 1 mm. This coating thickness is selected in consideration of the balance between the insulation effect and the overall size of the antenna.

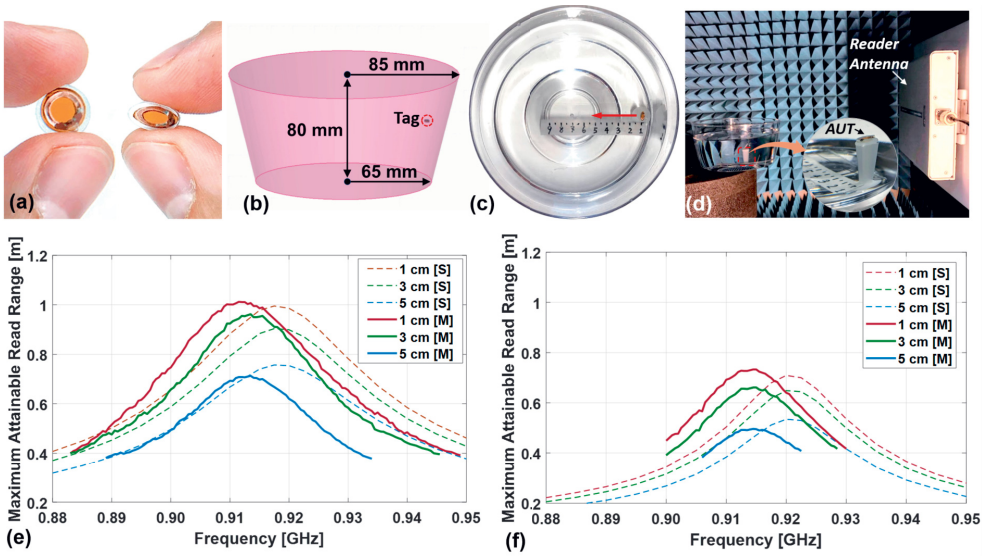

Figure 39. a. Prototyped round tag (left) and elliptic tag (right). b. Liquid phantom in simulation. c. Top view of the container filled with the tissue-mimicking liquid with the tag under test. d. Measurement setup in the EMC chamber. e. Comparison of the simulated and measured read ranges of the round tag with different horizontal depths in the liquid. f. Comparison of the simulated and measured read ranges of the elliptic tag with different horizontal depths in the liquid. [Publication II]

4.4.3.1 Wireless Measurement with Tissue Mimicking Phantom

In the wireless measurement, the tissue-mimicking liquid was prepared according to the FCC recommendation with the relative permittivity of 45.74 and conductivity of 0.77 S/m at 915 MHz. The prepared liquid was then transferred to a container that has a geometrical dimension comparable to the human head. Figure 39b shows the simulated tissue phantom with its geometrical size in the HFSS. To measure the prototype with different immersed depths, the author made a stand with a sliding rail in the container, as shown in Figure 39c. The horizontal distance from the stand and the container shell is the analogue of the implant depth in the human head.

The measurement was conducted with the Voyantic Tagformance system in the anechoic chamber, as shown in Figure 39d. Figure 39e and 39f compare the simulated and measured read ranges of the prototyped round and the elliptic tags, respectively. Overall, the measured and simulated results have a good agreement with the prototyped round and elliptic tags. The round tag, due to its relatively higher gain, provides 0.3 m longer distance in all the measured immerged depths. With a typical

depth of 3 cm, the read ranges of the round and elliptic tags are 0.95 m and 0.65 m, respectively.

4.4.3.2 In-vivo Experiment with Animal Model

To evaluate the applicability of the proposed antenna in in-vivo animal research, the author conducted a wireless measurement by implanting the round and elliptic tags into two Wistar rats' intracranial cavities, respectively. The experiment is approved by the National Animal Experiment Board of Finland (ESAVI/12830/2020).

Figure 40a and 40c show the rats with the implanted tags. The elliptic tag was implanted vertically in the rat's cranial cavity with an implant depth of 6 mm whereas the round one was implanted in horizontal placement with a depth of 3 mm. The measurement setup is demonstrated in Figure 40b and 40c where the rats were fixed on the plastic table, and the RFID reader antenna is placed with a vertical distance of 30 cm. For reference, a homogeneous tissue cube (ε_r=45.74, σ=0.77 S/m at 915 MHz) with a side-length of 50 mm was built to mimic the rat's head in the HFSS. Figure 40e shows the cube model with the tag in the simulation.

In the measurement, the position of the rats is adjusted so as to ensure that the tag antennas' **E** plane is perpendicular to the reader antenna. Figure 40f compares the simulated and measured read ranges. The round tag has a maximum read range of 1.2 m at 912 MHz, and the read range of the elliptic one is 1.1 m. The simulation generally predicts the antenna performance in the measurement. However, there are about 0.1 m level shift and 10 MHz frequency shift compared with the measured results. The main reasons for these shifts are the computational inaccuracy of the homogenous cubic model and the uncertainty in the in-vivo experiment. For example, in the surgery, the blood and the cement in the implant spot may influence the antenna performance, but this influence is difficult to be reflected in the simulation. Since the shifts are minor, the simulation still provides the reference value in the estimation of the antenna performance in practical implementations.

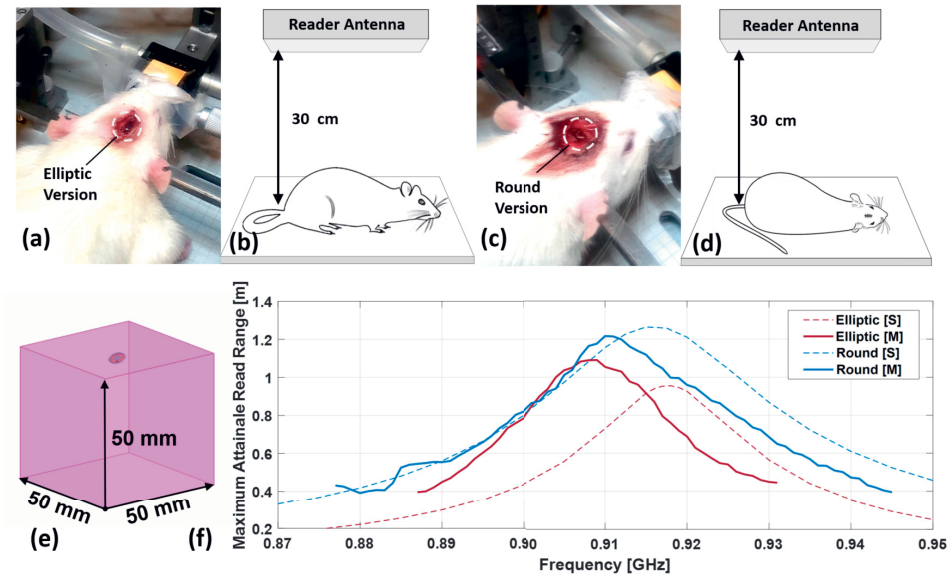

Figure 40. a. The rat with the elliptic tag vertically implanted in its cranial cavity. b. Measurement setup of the rat with the implanted elliptic tag. c. The rat with the round tag horizontally implanted in its cranial cavity. d. Measurement setup of the rat with the implanted round tag. e. Cubic tissue model to simulate the rat head in HFSS. f. Comparison of the simulated and measured read ranges. [Publication II]

4.4.4 Towards the Development of Passive RFID Pressure Sensor

The monitoring of the pressures in different locations of the human body provides valuable medical references in treatment and diagnosis. For instance, in brain care application, the monitoring of intracranial pressure (ICP) is a common medical practice to diagnose and evaluate brain trauma and neurological disorders [79]. Utilizing the proposed dual split rings antenna, the author demonstrates the feasibility to develop a small RFID pressure sensor [Publication IV] that can be potentially utilized for ICP monitoring.

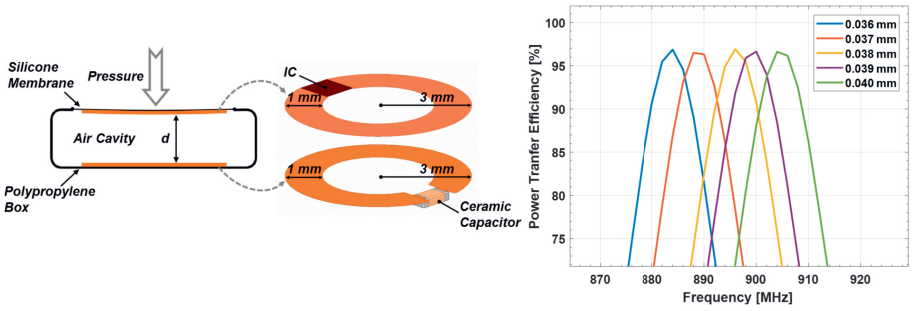

Figure 41. a. Structure of the proposed pressure sensor. b. Power transfer efficiency with different distances between the two rings. [Publication IV]

Figure 41a shows the structure of the proposed pressure sensor where the IC ring is attached to a silicone membrane, and the LC ring is fixed at the bottom of a polypropylene box. Due to the elasticity of the silicone membrane, the applied pressure results in the decrease of the distance d between the two rings. In the parametric analysis, the author found that the antenna input impedance is extremely sensitive to the distance d between the two rings. Figure 41b shows the power transfer efficiency τ with different d in a homogeneous tissue model (10 cm × 10 cm × 10 cm) assigned with the frequency-dependent dielectric properties (ε_r=45.74, σ=0.77 S/m at 915 MHz). According the comparison of the peak frequency of τ, an increase of 0.001 mm in d finally leads to a peak frequency shift of 4 MHz. This high sensitivity of the antenna impedance towards the variation of d can be potentially utilized for pressure monitoring.

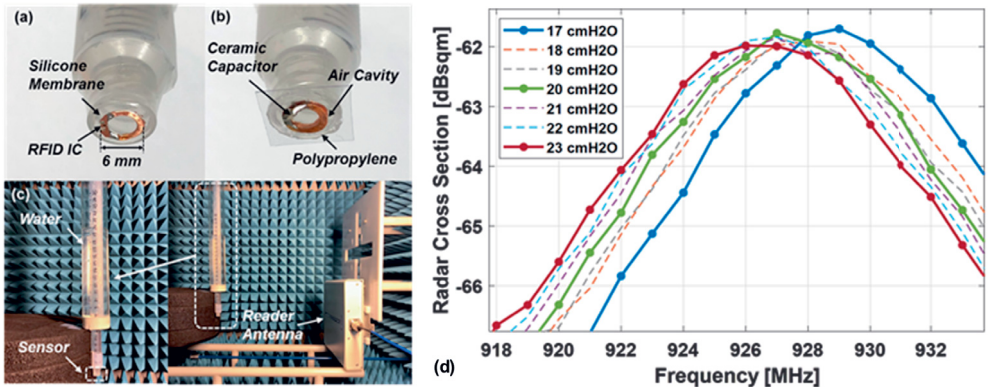

Figure 42. Left: Prototyped sensor and measurement setup in EMC chamber. Right: Measured tag ΔRCS versus different water pressures. [Publication IV]

To verify this idea, the author fabricated the sensor prototype and conducted a preliminary measurement in the air. Figure 42a and 42b demonstrate the prototyped sensor fixed on the tip of a syringe. Figure 42c shows the setup of the wireless measurement in the EMC chamber. The ICP is in a range of 10 to 20 cmH2O. In the wireless measurement, the author gradually increased the depth of the water inside the syringe from 17 cm to 23 cm with a step of 1 cm. In each step, the ΔRCS of the tag antenna is measured. According to the results shown in Figure 42d, the peak frequency of ΔRCS is inversely proportional to the applied pressure. With an increase of 3 cmH2O pressure, a shift of 2 MHz of the ΔRCS peak frequency can be observed. The preliminary measurement of the prototype verifies the linear correlation between the peak frequency of antenna ΔRCS and the applied pressure. Moreover, the prototyped sensor shows a resolution of 3 cmH2O in the pressure measurement. These results validate the feasibility to develop the passive RFID pressure sensor with the double split ring antenna.

5 CONCLUSIONS

One of the major challenges hindering the broad deployment of wireless implantable devices in clinical practice is the difficulty to establish an efficient and reliable through-body wireless link. To address this challenge, the main focus of this thesis has been concentrated on the essential part of a wireless implantable system - the implantable antenna. Based on the investigation on the characteristics of antenna radiation in the lossy tissue environment, two tailored antenna design methods have been proposed for far-field RFID based implantable systems for wireless brain care.

- A multimodal spatially distributed antenna with a small implant part and a passive head-worn part has been developed for intracranial implantable applications. According to the in-vitro measurement of the antenna prototype, the method of utilizing an inductively coupled wearable part to improve the overall antenna radiation efficiency and directivity has been proved to be effective even with an implant depth of 15 mm in the CSF tissue layer. With the antenna gain reaching -17 dBi, the maximum distance to activate an RFID microsystem carried by the proposed antenna exceeds 1.1 m. Moreover, since the wearable part influences the radiated **E** field in the antenna far-field, a special configuration of the wearable part is verified to realize the LHCP operation of the antenna. Importantly, the proposed antenna shows robustness towards different implant locations on the head model, which further verifies its feasibility to be implemented in wireless brain care applications.
- A dual-split-ring implantable antenna with a footprint of only $\pi \times (3 \times 1.5) \times 1$ mm^3 has been developed for intracranial brain care applications. The proposed antenna has a wide adjustable inductive impedance range that facilitates the self-matching with most of the microsystems with an energy harvesting unit. In the simulation with the anatomical head model, the proposed antenna provides an antenna gain of -25 dBi with an implant depth of 16 mm in the CSF tissue layer. In the wireless measurement with tissue mimicking-liquid, the maximum interrogation distance of the prototyped antenna reaches 0.7 m with an immersed depth of 30 mm. In an in-vivo

experiment with rats, the proposed antenna provides an interrogation distance of 1.1 m.

Overall, the thesis presents a comprehensive analysis of the development of antennas for intracranial implantable systems targeting for far-field data telemetry. The author believes that the proposed design solutions could contribute to the development of implantable antennas for wireless intracranial sensors in brain care applications and help to pave the way towards the realization of the envisioned biotelemetry.

5.1 Future Work and Perspectives

In the development of the batteryless semi-passive RFID sensor platform, there are two aspects that need further improvement. First, the output voltage from the harvester to toggle the switch needs to be regulated to prevent the RF switch intermittently running into a transition state. Secondly, the efficiency of the energy harvester needs to be further improved to enable the cold start of the system with a longer distance. In the future, the optimized sensor platform will be implemented with miniature implantable antennas and evaluated in the tissue environment.

Although the dual split ring antenna shows superiority in antenna footprint and radiation gain, the antenna efficiency could be further improved by manipulating the antenna radiation pattern with a decreased side lobe that points inwards the brain. Moreover, due to its high radiation efficiency and small dimension, the antenna can serve as the antenna element to build the implantable antenna array with improved antenna gain and directivity.

The feasibility to develop the passive RFID pressure sensor with the dual split ring antenna has been preliminarily validated in the air; the future work will focus on the optimization of the sensor structure and the evaluation in the lossy tissue environment.

REFERENCES

[1] J. J. Vidal, “Toward direct brain-computer communication,” *Annual Review of Biophysics and Bioengineering*. vol. 2, no. 1, pp. 157–80, 1973.

[2] M. A. Lebedev, M. A. Nicolelis, “Brain–machine interfaces: past, present and future,” *Trends in Neurosciences*, vol. 29, no. 9, pp. 536-546, 2006.

[3] J. K. Chapin et al. “Real-time control of a robot arm using simultaneously recorded neurons in the motor cortex,” *Nat. Neurosci*., vol. 2, pp. 664–670, 1999.

[4] F. G. Zeng, S. Rebscher, W. Harrison, X. Sun, H. Feng “Cochlear implants: system design, integration, and evaluation,” *IEEE Rev Biomed Eng*. 2008.

[5] E. D. Flora, C. L. Perera, A. L. Cameron, G. J. Maddern, “Deep brain stimulation for essential tremor: A systematic review,” *Mov. Disord.*, vol. 25, pp. 1550-1559, 2010.

[6] J. Wang, H. Xie, T. Chung, L. L. H. Chan, S. W. Pang, “Neural probes with integrated temperature sensors for monitoring retina and brain implantation and stimulation,” *IEEE Trans. Neural Syst. Rehabil. Eng.*, vol. 25, no. 9, pp. 1663–1673, 2017.

[7] C. W. Lee, A. Kiourti, J. Chae, and J. L. Volakis, “A high-sensitivity fully passive neurosensing system for wireless brain signal monitoring,” *IEEE Trans. Microw. Theory Techn.*, vol. 63, no. 6, pp. 2060–2068, 2015.

[8] M. W. A. Khan, L. Sydänheimo, L. Ukkonen, T. Björninen, “Inductively powered pressure sensing system integrating a far-field data transmitter for monitoring of intracranial pressure,” *IEEE Sensors Journal*, vol. 17, no. 7, pp. 2191-2197, 2017.

[9] M. A. Shaeri, A. M. Sodagar, “A method for compression of intra-cortically-recorded neural signals dedicated to implantable brain–machine interfaces,” *IEEE Transactions on Neural Systems and Rehabilitation Engineering*, vol. 23, no. 3, pp. 485-497, 2015.

[10] L. Pazzini, D. Polese, J. F. Weinert et al. “An ultra-compact integrated system for brain activity recording and stimulation validated over cortical slow oscillations in vivo and in vitro,” *Sci. Rep.*, vol. 8, 16717, 2018.

[11] R. Chen, A. Canales, P. Anikeeva, “Neural recording and modulation technologies,” *Nat. Rev. Mater*, vol. 2, 16093, 2017.

[12] C. Pena et al., “An overview of FDA medical device regulation as it relates to deep brain stimulation devices,” *IEEE Transactions on Neural Systems and Rehabilitation Engineering*, vol. 15, no. 3, pp. 421-424, 2007.

[13] A. Mohammed, M. Zamani, R. Bayford, A. Demosthenous, “Toward on-demand deep brain stimulation using online parkinson’s disease prediction driven by dynamic detection,” *IEEE Transactions on Neural Systems and Rehabilitation Engineering*, vol. 25, no. 12, pp. 2441-2452, 2017.

[14] C. O. Oluigbo, A. Salma, A. R. Rezai, “Deep brain stimulation for neurological disorders,” *IEEE Reviews in Biomedical Engineering*, vol. 5, pp. 88-99, 2012.

[15] H. A. Wheeler, “Fundamental limitations of small antennas,” *Proceedings of the IRE*, vol. 35, no. 12, pp. 1479–1484, 1947.

[16] A. S. Y. Poon, S. O’Driscoll, T. H. Meng, “Optimal frequency for wireless power transmission over dispersive tissue,” *IEEE Trans. Antennas Propag.*, vol. 58, no. 5, pp. 1739–1749, 2010.

[17] M. Zaeimbashi et al., “NanoNeuroRFID: a wireless implantable device based on magnetoelectric antennas,” *IEEE J. Electromagn., RF Microw. Med. Biol.*, vol.3, pp. 206-215, 2019.

[18] Z. Xiao et al., “An implantable RFID sensor tag toward continuous glucose monitoring,” *IEEE Journal of Biomedical and Health Informatics*, vol. 19, no. 3, pp. 910-919, 2015.

[19] H. Huang et al., “RFID tag helix antenna sensors for wireless drug dosage monitoring,” *IEEE Journal of Translational Engineering in Health and Medicine*, vol. 2, pp. 1-8, 2014.

[20] T. Volk et al., “RFID technology for continuous monitoring of physiological signals in small animals,” *IEEE Transactions on Biomedical Engineering*, vol. 62, no. 2, pp. 618-626, 2015.

[21] EPC UHF radio frequency identity protocols: class 1 generation 2 UHF RFID, version 1.2.0 [Online]. Available: https://www.gs1.org/standards/epc-rfid [Accessed: June-2020]

[22] H. T. Friis, “A note on a simple transmission formula,” *Proc. IRE*, vol. 34, no. 5, pp. 254-256, 1946.

[23] K. Finkenzeller, *RFID-Handbook*, 2nd ed., Wiley, New York, 2003.

[24] P. V. Nikitin, K. V. S. Rao, R. D. Martinez, “Differential RCS of RFID tag,” *Electronics Letters*, vol. 43, no. 8, pp. 431-432, 2007.

[25] S. Amendola et al., “Calibration and experimentation of an epidermal RFID sensor for remote temperature monitoring,” *IEEE Sens. J.*, vol. 16, pp. 7250–7257, 2016.

[26] C. Occhiuzzi, C. Paggi, G. Marrocco, “Passive RFID strain-sensor based on meander-line antennas,” *IEEE Trans. Antennas Propag.*, vol. 59, pp. 4836–4840, 2011.

[27] A. Hillier, V. et al., “A passive UHF RFID pH sensor (Smart polymers for wireless medical sensing devices),” Loughborough Antennas & Propagation Conference (LAPC 2017), Loughborough, pp. 1-2, 2017.

[28] S. Manzari, et al., “humidity sensing by polymer-loaded UHF RFID antennas,” *IEEE Sens. J.*, vol. 12, pp. 2851-2858, 2012.

[29] Datasheet of AMS SL900A Chip [Online]. Available: https://ams.com/sl900a [Accessed: June-2020]

[30] Datasheet of Farsens Rocky100 Chip [Online]. Available: http://www.farsens.com/en/products/rocky100/ [Accessed: June-2020]

[31] Tagformance pro measurement system, user guide, 2015 [Online]. Available: http://voyantic.com/products/tagformance-pro [Accessed: June-2020]

[32] Mercury 6 4-port enterprise uhf rain RFID reader, 2017 [Online], Available: https://www.jadaktech.com/documentation/rfid/mercury6-readers/ [Accessed: June-2020]

[33] R. E. Collin, F. J. Zucker, *Antenna Theory Part II*, Inter-University Electronics Series. McGraw-Hill Book, vol. 7, 1969.

[34] Denys Nikolayev et al., “Electromagnetic radiation efficiency of body-implanted devices,” *Phys. Rev. Applied*, vol. 9, 2018.

[35] C. Miry, R. Gillard, R. Loison, “An application of the multi-level DG-FDTD to the analysis of the transmission between a dipole in free-space and an implanted antenna in a simplified body model with various positions,” *Proc. 3rd European Conference on Antennas and Propagation* EuCAP, pp. 67–70, 23–27, Berlin, Germany Mar. 2009.

[36] K. Koski, T. Björninen, L. Sydänheimo, L. Ukkonen, Y. Rahmat-Samii, “A new approach and analysis of modeling the human body in RFID-enabled body-centric wireless systems,” *Int.J. Antennas Propag.*, vol. 2014, 2014.

[37] S. M. Abbas, K. P. Esselle, Y. Ranga, “An armband-wearable printed antenna with a full ground plane for body area networks,” 2014 IEEE Antennas and Propagation Society International Symposium (APSURSI), pp. 318-319, Memphis, TN, USA, 2014.

[38] L. Song and Y. Rahmat-Samii, “An end-to-end implanted brain–machine interface antenna system performance characterizations and development,” *IEEE Trans. Antennas Propag.*, vol. 65, no. 7, pp. 3399-3408, July 2017.

[39] C. Miry, T. Alves, R. Gillard, J. Laheurte, R. Loison, and B. Poussot, “Analysis of the transmission between on-body devices using the bilateral Dual-Grid FDTD technique,” *Antennas and Wireless Propagation Letters*, vol. 9, pp. 1073 –1075, 2010.

[40] J. Kim and Y. Rahmat-Samii, “Implanted antennas inside a human body: simulations, designs, and characterizations,” *IEEE Trans. Microw. Theory Tech.*, vol. 52, no. 8, pp. 1934–1943, 2004.

[41] S. N. Makarov et al., “Virtual human models for electromagnetic studies and their applications,” *IEEE Reviews in Biomedical Engineering*, vol. 10, pp. 95-121, 2017.

[42] The Virtual Population, “High-resolution anatomical models for computational life sciences,” SPEAG AG, Flyer, EuCAP 2016, Davos, Switzerland, 2016.

[43] G. M. Noetscher, J. Yanamadala, M. Kozlov, S. Louie, A. Nazarian, S. Makarov, “VHP-female v3.0 FEM/BEM computational human phantom,” in Proc. 24th Int. Meshing Roundtable, Austin, TX, 2015.

[44] A. V. Vorst, A. Rosen, Y. Kotsuka, *Fundamentals of electromagnetics. RF/Microwave interaction with biological tissues*, Wiley Online Library, 2005.

[45] P. A. Hasgall et al., “IT’IS database for thermal and electromagnetic parameters of biological tissues,” Version 3.0, 2015. [Online]. Available: www.itis.ethz.ch/database [Accessed: June-2020]

[46] S. Gabriel, R. W. Lau, C. Gabriel, “The dielectric properties of biological tissues: II. Measurements in the frequency range 10Hz to 20 GHz,” *Phys. Med. Biol.*, vol. 41, no. 11, pp. 2251–2269, 1996.

[47] S. Gabriel, R. W. Lau, C. Gabriel, “The dielectric properties of biological tissues: Part III. Parametric models for the dielectric spectrum of tissues,” *Phys. Med. Biol.*, vol. 41, no. 11, pp. 2271–2293, 1996.

[48] J. Yanamadala et al., “New VHP-female V.2.0 full-body computational phantom and its performance metrics using FEM simulator ANSYS HFSS,” *Proc. 37th Annu. Int. Conf. IEEE Eng. Med. Biol. Soc.*, Milano, Italy, pp. 3237–3241, 2015.

[49] Z. Chen, H. Sun and W. Geyi, “Maximum wireless power transfer to the implantable device in the radiative near field,” *IEEE Antennas and Wireless Propagation Letters*, vol. 16, pp. 1780-1783, 2017.

[50] B. Rana, J. Shim and J. Chung, “An implantable antenna with broadside radiation for a brain–machine interface,” *IEEE Sensors Journal*, vol. 19, no. 20, pp. 9200-9205, 2019.

[51] S. Das and D. Mitra, “A compact wideband flexible implantable slot antenna design with enhanced gain,” *IEEE Transactions on Antennas and Propagation*, vol. 66, no. 8, pp. 4309-4314, 2018.

[52] J. Kim, Y. Rahmat-Samii, “Planar inverted-F antennas on implantable medical devices: meandered type versus spiral type,” *Microw. Opt. Technol. Lett.*, 48: 567-572, 2006.

[53] P. Soontornpipit, C. M. Furse, Y. C. Chung, “Design of implantable microstrip antenna for communication with medical implants,” *IEEE Trans. Microw. Theory Techn*., vol. 52, no. 8, pp. 1944-1951, 2004.

[54] A. Abdi, H. Aliakbarian, “A miniaturized UHF-band rectenna for power transmission to deep-body implantable devices,” *IEEE Journal of Translational Engineering in Health and Medicine*, vol. 7, pp. 1-11, 2019.

[55] X. Yang, H. Wong and J. Xiang, “Polarization reconfigurable planar inverted-F antenna for implantable telemetry applications,” *IEEE Access*, vol. 7, pp. 141900-141909, 2019.

[56] C. Liu, Y. Guo, H. Sun, S. Xiao, “Design and safety considerations of an implantable rectenna for far-field wireless power transfer,” *IEEE Trans. Antennas Propag.*, vol. 62, no. 11, pp. 5798-5806, 2014.

[57] M. Wang et al., “Investigation of SAR reduction using flexible antenna with metamaterial structure in wireless body area network,” *IEEE Trans. Antennas Propag.*, vol. 66, no. 6, pp. 3076-3086, 2018.

[58] K. S. Nikita, G. S. Stamatakos, N. K. Uzunoglu, A. Karafotias, “Analysis of the interaction between a layered spherical human head model and a finite-length dipole,” *IEEE Trans. Microw. Theory Tech.*, vol. 48, no. 11, pp. 2003–2013, 2000.

[59] F. Merli, B. Fuchs, J.R. Mosig, A.K. Skrivervik, “The effect of insulating layers on the performance of implanted antennas,” *IEEE Trans. Antennas Propag.*, vol. 59, no. 1, pp. 21-31, 2011.

[60] C. J. Sanchez-Fernandez, O. Quevedo-Teruel, J. Requena-Carrion, L. Inclan-Sanchez, E. Rajo-Iglesias, “Dual-band microstrip patch antenna based on short-circuited ring and spiral resonators for implantable medical devices.” *IET Microwaves, Antennas Propag.*, vol. 4, no. 8, pp. 1048-1055, 2010.

[61] L. Xu, Y. Guo and W. Wu, “Miniaturized dual-band antenna for implantable wireless communications,” *IEEE Antennas and Wireless Propag. Letters*, vol. 13, pp. 1160-1163, 2014.

[62] C. Zhang et al, “A wideband circularly polarized implantable antenna for 915 MHz ism-band biotelemetry devices,” *IEEE Antennas and Wireless Propag. Letters*, vol.17, pp. 1473-1477, 2018.

[63] Z. Chen et al., “Maximum wireless power transfer to the implantable device in the radiative near field,” *IEEE Antennas and Wireless Propag. Letters*, vol. 16, pp. 1780-1783, 2017.

[64] S. A. A. Shah and H. Yoo, “Scalp-implantable antenna systems for intracranial pressure monitoring,” *IEEE Trans. Antennas and Propag.*, vol. 66, pp. 2170-2173, 2018.

[65] A. Abdi and H. Aliakbarian, “A miniaturized UHF-band rectenna for power transmission to deep-body implantable devices,” *IEEE Journal of Translational Engineering in Health and Medicine*, vol. 7, pp. 1-11, 2019.

[66] Z. Jiang et al., “Wideband loop antenna with split-ring resonators for wireless medical telemetry,” *IEEE Antennas and Wireless Propagation Letters*, vol. 18, no. 7, pp. 1415-1419, 2019.

[67] B. Rana et al., “An implantable antenna with broadside radiation for a brain–machine interface,” *IEEE Sensors Journal,* vol. 19, pp. 9200-9205, 2019.

[68] H. Li, Y. Guo, C. Liu, S. Xiao and L. Li, "A miniature-implantable antenna for medradio-band biomedical telemetry," *IEEE Antennas and Wireless Propagation Letters*, vol. 14, pp. 1176-1179, 2015.

[69] T. Björninen, L. Sydänheimo, L. Ukkonen, "Development and validation of an equivalent circuit model for UHF RFID IC based on wireless tag measurements," *AMTA Symp.*, Bellevue, WA, USA, 2012.

[70] G. Hartsgrove et al., "Simulated biological materials for electromagnetic radiation absorption studies," *Bioelectromagnetics*, vol. 8, pp. 29-36, 1987.

[71] Body tissue dielectric parameters (Federal Communications Commission) [Online]. Available: www.fcc.gov/general/body-tissuedielectric-parameters [Accessed: June-2020]

[72] A. Drossos, V. Santomaa and N. Kuster, "The dependence of electromagnetic energy absorption upon human head tissue composition in the frequency range of 300-3000 MHz," *IEEE Trans. Microwave Theory Techn.*, vol. 48, no. 11, pp. 1988–1995, 2000.

[73] J. Hong, *Microstrip Filters For RF/Microwave Applications*, Second Edition. Hoboken, N.J., Wiley, 2011.

[74] S. S. Mohan et al., "Simple accurate expressions for planar spiral inductances," *IEEE J. Solid-State Circuits*, vol. 34, pp. 1419–1424, 1999.

[75] R. Garg, I. J. Bahl, "Characteristics of coupled microstrip lines," *IEEE Trans. Microw. Theory Tech.*, vol. 27, pp. 700–705, 1979.

[76] U. M. Jow and M. Ghovanloo, "Design and optimization of printed spiral coils for efficient transcutaneous inductive power transmission," *IEEE Trans. Biomed. Circuits Syst.*, vol. 1, pp. 193–202, 2007.

[77] V. O. Korhonen et al., "Light propagation in NIR spectroscopy of the human brain," *IEEE Journal of Selected Topics in Quantum Electronics*, vol. 20, pp. 289-298, 2014

[78] F. B. Haeussinger et al., "Simulation of near-infrared light absorption considering individual head and prefrontal cortex anatomy: implications for optical neuroimaging," *PLoS One*, vol. 6, 2011.

[79] L. Chen et al., "Continuous wireless pressure monitoring and mapping with ultra-small passive sensors for health monitoring and critical care," *Nat Commun*., vol. 5, 2014.

[80] K. S. Yee, "Numerical solution of initial boundary value problems involving Maxwell's equations in isotropic media," *IEEE Trans. Antennas Propagat.*, vol. 14, no. 4, pp. 302-307, 1966.

[81] R. F. Harrington, "Matrix methods for field problems," *Proc. IEEE*, vol. 55, no. 2, pp. 136-149, Feb. 1967.

[82] T. Hubing, C. Su, H. Zeng, H. Ke, "Survey of current computational electromagnetics techniques and software," Clemson University, 2008.

[83] J. W. Hand, “Modeling the interaction of electromagnetic fields (10 MHz-10 GHz) with the human body: methods and applications,” *Phys Med Biol.*, vol. 53, no. 16, pp. 243-286, 2008.

[84] K. Ito, K. Furuya, Y. Okano and L. Hamada, “Development and characteristics of a biological tissue-equivalent phantom for microwaves,” *Electron. Commun. Japan*, vol. 84, no. 4, pp. 67-77, 2001.

[85] A. Kiourti, J. R. Costa, C. A. Fernandes and K. S. Nikita, “A broadband implantable and a dual-band on-body repeater antenna: Design and transmission performance", *IEEE Trans. Antennas Propag.*, vol. 62, no. 6, pp. 2899-2908, 2014.

[86] M. Manoufali, K. Bialkowski, B. Mohammed, P. C. Mills and A. M. Abbosh, “Compact implantable antennas for cerebrospinal fluid monitoring,” *IEEE Trans. Antennas Propag.*, vol. 67, no. 8, pp. 4955-4967, 2019.

[87] X. Y. Liu et al., “A miniaturized CSRR loaded wide-beamwidth circularly polarized implantable antenna for subcutaneous real-time glucose monitoring,” *IEEE Antennas and Wireless Propag. Letters*, vol. 16, pp. 577-580, 2017.

[88] M. S. Islam, K. P. Esselle, D. Bull and P. M. Pilowsky, "Converting a wireless biotelemetry system to an implantable system through antenna redesign," in *IEEE Trans Microwave Theory and Techniques*, vol. 62, no. 9, pp. 1890-1897, 2014.

[89] J. R. Smith, A. P. Sample, P. S. Powledge, S. Roy, and A. Mamishev, “A wirelessly-powered platform for sensing and computation,” in UbiComp 2006: Ubiquitous Computing, pp. 495–506, Springer Berlin Heidelberg, 2006.

[90] S. Naderiparizi, Z. Kapetanovic and J. R. Smith, “RF-powered, backscatter-based cameras,” 2017 11th European Conference on Antennas and Propagation (EUCAP), Paris, pp. 346-349, 2017.

[91] A. Kiourti, K. S. Nikita, “A review of in-body biotelemetry devices: Implantables, ingestibles and injectables,” *IEEE Trans. Biomed. Eng.*, vol. 64, no. 7, 2017.

[92] A. Yakovlev, S. Kim, A. Poon, “Implantable biomedical devices: Wireless powering and communication,” *IEEE Commun. Mag.*, vol. 50, no. 4, 2012.

[93] L. Ukkonen, L. Sydänheimo, “Contactless health-care sensing,” *Nature*, vol. 551, pp. 572–573, 2017.

[94] A. Sharma, E. Kampianakis and M. S. Reynolds, “A Dual-Band HF and UHF antenna system for implanted neural recording and stimulation devices,” *IEEE Antennas and Wireless Propag. Letters*, vol. 16, pp. 493-496, 2017.

[95] An introduction to HFSS: fundamental principles, concepts, and use [Online]. Available: https://elearning.ju.edu.jo/file.php/15311/HFSSintro.pdf [Accessed: June-2020]

[96] U.S. Food and Drug Administration, Center for Devices and Radiological Health, “Reporting of computational modeling studies in medical device submissions: Draft guidance for industry and food and drug administration staff,” 2014. [Online].

Available: http://www.fda.gov/downloads/MedicalDevices/DeviceRegulationandGuidance/GuidanceDocuments/UCM381813.pdf [Accessed: June-2020]

[97] K. H. Yang, J. Hu, N. A. White, A. I. King, C. C. Chou, and P. Prasad, "Development of numerical models for injury biomechanics research: A review of 50 years of publications in the stapp car crash conf.," *Stapp Car Crash J.*, vol. 50, pp. 429–490, 2006.

[98] M. Iwamoto, Y. Nakahira, and H. Kimpara, "Development and validation of the total human model for safety (THUMS) toward further understanding of occupant injury mechanisms in precrash and during crash," *Traffic Injury Prevention*, vol. 16, pp. 1–13, 2015.

[99] T. N. Killian, S. M. Rao, and M. E. Baginski, "Electromagnetic scattering from electrically large arbitrarily-shaped conductors using the method of moments and a new null-field generation technique," *IEEE Trans. Antennas Propag.*, vol. 59, no. 2, pp. 537–545, 2011.

[100] A. Lea, P. Hui, J. Ollikainen, and R. Vaughan, "Propagation between onbody antennas," *IEEE Trans. Antennas Propag.*, vol. 57, no. 11, pp. 3619– 3627, 2009.

[101] M. Grimm and D. Manteuffel, "Electromagnetic wave propagation on human trunk models excited by half-wavelength dipoles," in Proc. Antennas Propag. Conf., Loughborough, U.K., pp. 493–496, 2010.

[102] N. H. M. Rais, P. J. Soh, F. Malek, S. Ahmad, N.B.M. Hashim, and P. S. Hall, "A review of wearable antenna," in Proc. Antennas Propag. Conf., Loughborough, U.K., pp. 225–228, 2009.

[103] S. Oh, A. G. Webb, T. Neuberger, B. Park, and C. M. Collins, "Experimental and numerical assessment of MRI-induced temperature change and SAR distributions in phantoms and in vivo," *Magn. Reson. Med.*, vol. 63, no. 1, pp. 218–223, 2010.

[104] E. Cabot, A. Christ, and N. Kuster, "Whole body and local SAR in anatomical phantoms exposed to RF fields from birdcage coils," in Proc. 29th Gen. Assem. Int. Union Radio Sci., Chicago, USA, 2008.

PUBLICATIONS

PUBLICATION I

Split-Ring Resonator Antenna System with Cortical Implant and Head-Worn Parts for Effective Far-Field Implant Communications

Shubin Ma, Lauri Sydänheimo, Leena Ukkonen and Toni Björninen

IEEE Antennas and Wireless Propagation Letters, vol. 17, no. 4, pp. 710-713, April 2018,
doi: 10.1109/LAWP.2018.2812920.

Split-Ring Resonator Antenna System With Cortical Implant and Head-Worn Parts for Effective Far-Field Implant Communications

Shubin Ma(马述彬), *Student Member, IEEE*, Lauri Sydänheimo, *Member, IEEE*, Leena Ukkonen, *Member, IEEE*, and Toni Björninen, *Member, IEEE*

***Abstract*—We propose a spatially distributed antenna system to serve as the radio platform for RFID-inspired brain care applications. The antenna system consists of a passive wearable part placed on the scalp and a cortical implant part with split-ring resonator topology for miniaturization and antenna self-matching with a backscattering microsystem. We have optimized the antenna system in a hybrid head model combining anatomical features with a layered ellipsoid mimicking the major tissue layers of the human head in a controlled manner. Results from the wireless testing of the prototyped antenna system indicate that it enables remote powering and readout of a −18 dBm RFID microsystem at a distance of 1 m at 915 MHz with 10 mm implant depth. Moreover, our experiment shows that the studied system is tolerant toward misalignment between the implantable and wearable parts.**

***Index Terms*—Electrotextile, implantable antenna, RFID, split-ring antenna, wearable antenna.**

I. Introduction

WIRELESS implantable sensors for intracranial signal (e.g., electrocochleography (ECoG) and intracranial pressure) extraction are believed to possess promises for brain diseases treatment and quality of life improvement for the patients suffering from a traumatic brain or spinal cord injury or stroke [1]. One of the major challenges when deploying such wireless implantable system is achieving a reliable wireless radio link inside and around a human head due to the structural complexity and unfavorable electromagnetic properties of the biological environment. For this reason, various human tissue models with different complexity and modeling approaches have been proposed to predict the behavior of electromagnetic wave in the proximity of the human head [2], [3]. Meanwhile, the miniaturization requirement of the implant to reduce the patient's risk of tissue scarring also adds difficulty to the overall design of an implantable sensor. In a sensor with a miniature size, the battery is no longer an optimal power source, and remote powering of the system becomes preferable. RFID-based sensors are, thus, proposed. Equipped with the RFID technology, the sensor can harvest energy through the near-field electromagnetic field generated by an off-body device and send back the sampled data via a backscattering radio link. Without the necessity of the battery, the sensor footprint is largely decreased, and the miniaturization of its antenna system becomes especially important.

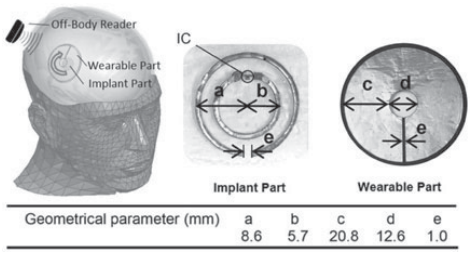

Geometrical parameter (mm)	a	b	c	d	e
	8.6	5.7	20.8	12.6	1.0

Fig. 1. Ellipsoid head model and prototyped antenna system with its geometrical dimensions.

According to a recent literature survey [4], a planar inverted-F antenna is the most common approach to achieve small implantable antennas. However, it requires a ground plane, and sometimes, additional vias and interconnected metallization layers have been introduced for the purpose of miniaturization. Therefore, it is hard to achieve thin and flexible structure, and in [4], all of the reviewed antennas comprise rigid circuit boards. To provide an alternative approach, we have proposed a spatially distributed antenna shown in Fig. 1 [5]. In this approach, only a thin and flexible split-ring resonator (SRR)-inspired part is implanted, and for far-field performance boost, a wearable part is affixed on the skin. In this approach, we only implant part of the antenna and also avoid the challenging task of downsizing the whole antenna structure as the size of the wearable part is not as strictly limited in this application.

In this letter, we will further investigate the implementation of a radio platform for brain care applications based on the SRR-inspired antenna system shown in Fig. 1. We introduce a layered ellipsoid model for the human head to assess the system's performance in a realistic setting compared with [5] and present further experimental evaluations of the robustness of the antenna system toward misalignment between the two

Manuscript received January 31, 2018; accepted March 1, 2018. Date of publication March 14, 2018; date of current version April 5, 2018. This work was supported in part by the Academy of Finland, in part by the Jane and Aatos Erkko Foundation, and in part by the Finnish Funding Agency for Technology and Innovation. *(Corresponding author: Shubin Ma.)*

The authors are with the BioMediTech Institute and Faculty of Biomedical Science and Engineering, Tampere University of Technology, Tampere 33720, Finland (email: shubin.ma@tut.fi; lauri.sydanheimo@tut.fi; leena.ukkonen@tut.fi; toni.bjorninen@tut.fi).

Digital Object Identifier 10.1109/LAWP.2018.2812920

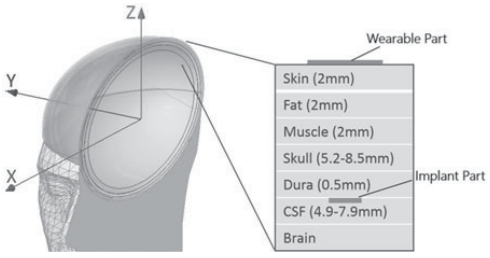

Fig. 2. Anatomical human head model with the layered ellipsoid.

parts. Finally, we verify the electromagnetic performance of the system when the wearable part is made of a textile conductor.

II. Antenna Development

Fig. 1 illustrates the fabricated RFID antenna system with its geometrical dimensions and the implemented position in the ellipsoid head model. We made the implant part with two concentric 35 μm thick copper ($\sigma = 58$ MS/m) rings. The 50 μm thick flexible polyethylene ($\varepsilon_r = 2.25$, tan$\delta = 0.001$ at 915 MHz) was used as the substrates. We attached the NXP UCODE G2iL series RFID IC to the inner ring split of the implant part using Circuit Works CW2400 conductive epoxy. We made a 1 mm thick coating box with silicone ($\varepsilon_r = 2.2$, tan$\delta = 0.007$ at 915 MHz) wrapping the implant to isolate the conductor from the human tissue. The wearable part inspired by the triple split-ring structure is affixed to the skin with its slit on the same direction as that of the outer ring of the implant part. We made it with the same 35 μm thick copper foil with 2 mm thick ethylene-propylene-diene-monomer (EPDM; $\varepsilon_r = 1.26$, tan$\delta = 0.007$ at 915 MHz) as the substrate.

A. Simulation Model

All the electromagnetic modeling and simulation were conducted in ANSYS High-Frequency Structure Simulator. In the simulation, we used the parallel connection of the resistance and capacitance of 2.85 kΩ and 0.91 pF, respectively, to model the RFID IC [6]. Meanwhile, we adopted the ANSYS anatomical human head model and built a seven-layer ellipsoid to mimic the human head including the most important tissue types. Fig. 2 shows the details of the anatomical head model combined with the layered ellipsoid. The ellipsoid was constructed by fitting its shape to the anatomical head model by visual inspection and then building the seven tissue layers, namely, skin, fat, muscle, skull, dura, cerebrospinal fluid (CSF), and brain, which are the major tissue layers of the human head in terms of thickness. The thicknesses of skin, fat, and muscle layers were selected according to [7]. The thickness of the dura layer was set to 0.5 mm, which is close to the median of 0.3–0.8 mm [8]. In reality, the skull thickness and the width of the subarachnoid space (SAS) occupied by CSF vary greatly depending on the location. Therefore, we measured these values over several cross-sectional slices of the anatomical head model to obtain averaged values. The thinner regions of the skull tend to coincide with wider SAS. Moreover, since we consider attaching the implant to the dura (see Fig. 2), the range for the skull thickness we present in Fig. 2 is the mean minimum thickness, whereas the CSF layer thickness is the mean maximum SAS width. This selection was made because we considered its benefits for both safety and wireless performance to maximize/minimize the distance between the implant and the brain/wearable part. In the simulation, all the tissues were assigned with their corresponding relative permittivity and loss tangent according to the frequency-dependent four-term Cole–Cole relaxation model [9]. The database of tissue properties utilized in this work is obtained from the IT'IS Foundation [10].

Despite the fact that the ellipsoid model can be readily built in the simulator, in practice it is very hard to create a solid phantom with exactly the same shape and tightly controlled tissue layer thickness and dielectric properties. Therefore, in the testing, we used a homogeneous liquid phantom in a container having the shape of a truncated cone (lower radius: 6.75 cm, upper radius: 8.25 cm, height: 8 cm). The head equivalent liquid was made with 42% of water, 57% of sugar, and 1% of salt having the dielectric properties of $\varepsilon_r = 41.5$, $\sigma = 0.98$ S/m at 915 MHz [11]. For the comparison between the measurement and simulations, we implemented exactly the same model also in the simulator.

B. Antenna Optimization

In the passive UHF RFID system, RFID tag communicates with the reader by impedance-modulated backscattering radio link. Since the RFID readers have typically high sensitivity of -70 to -90 dB, the maximum detectable distance of the tag is determined by the distance at which the tag could absorb enough power to exceed the wake-up power threshold of the RFID IC. Friis' free-space formula can be used to calculate this maximum off-body detectable distance d_{tag} as

$$d_{\text{tag}} = \frac{\lambda}{4\pi}\sqrt{\frac{\text{De}_r\,\tau\text{EIRP}}{P_{\text{ic0}}}} \tag{1}$$

where D is the antenna directivity, e_r is the radiation efficiency, EIRP is the equivalent isotropically radiated power, P_{ic0} is the RFID IC wake-up power threshold, and τ is the power transfer efficiency given by

$$\tau = \frac{4\,\text{Re}\,(Z_A)\,\text{Re}\,(Z_c)}{|Z_A + Z_C|^2} \tag{2}$$

where Z_A is the antenna impedance and Z_C is the IC impedance. Power transfer efficiency measures the ratio between the power available from the tag antenna to that transferred to IC. It reaches the maximum value when the antenna and IC are complex-conjugate matched with each other.

According to (1), the tag read range is in direct proportion to antenna gain and power transfer efficiency. Thus, in the optimization of the geometrical dimensions of the antenna, we targeted at both good complex-conjugate impedance matching with the IC and a high antenna gain. We found that the wearable part had negligible influence on the antenna impedance and thus were able to achieve the impedance matching by optimization of the geometrical dimensions of the implant part independent from those of the wearable part. As shown in Fig. 3, complex-conjugate impedance matching is closest at 915 MHz. Despite

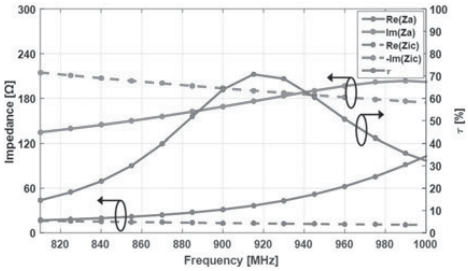

Fig. 3. Antenna impedance, complex-conjugate of the IC impedance, and the antenna-IC power transfer efficiency.

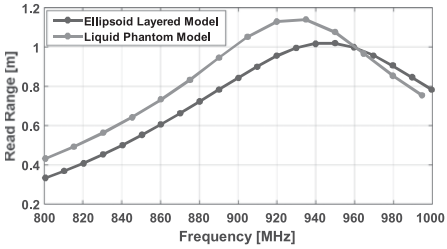

Fig. 4. Comparison of the simulated read range of the ellipsoid layered model and liquid phantom model.

the difference in real parts of the antenna and IC impedances, τ reaches 70% at 915 MHz.

The geometrical dimensions of the wearable part were optimized to maximize the system directivity. According to the simulation results, the antenna directivity increased by 8 dB, reaching 4.3 dBi with the wearable part concentrically placed 10 mm away from the implant part. Meanwhile, the simulated radiation efficiency is 0.48%.

In the ellipsoid model, the thicknesses of skull layers were set to its smallest value 5.2 mm, and thus the implant depth was 11.7 mm. To compare the results from the two models, we set the same 11.7 mm implant depth in the liquid phantom model. Fig. 4 shows the simulated read range from the two models, and they give similar results with slightly different frequencies of the peak value. In general, the proposed antenna system is capable of providing 0.8 m attainable read range within the 902–928 MHz band.

III. Results From Wireless Testing

We tested the prototyped antenna system with the Voyantic Tagformance measurement system in an anechoic chamber. Fig. 5 demonstrates the measurement setup. It consists of the reader antenna, the RFID measurement unit with an adjustable transmission frequency from 600 MHz to 1.2 GHz with up to 30 dBm output power, and the control software. The system is capable of detecting the backscattering signal strengths down to -80 dBm. During the measurement, we first characterized the wireless channel between the measurement system and the antenna under test with a system reference tag with known properties. Then, the lowest continuous transmission power to ensure the receiving of the response to the query command from the reader

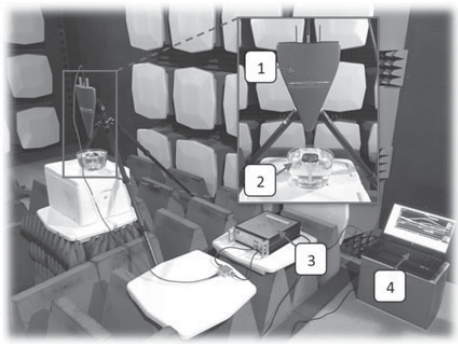

Fig. 5. Wireless measurement setup. 1: Reader antenna. 2: Liquid phantom with the antenna system under test. 3: Tagformance measurement unit. 4: Control software.

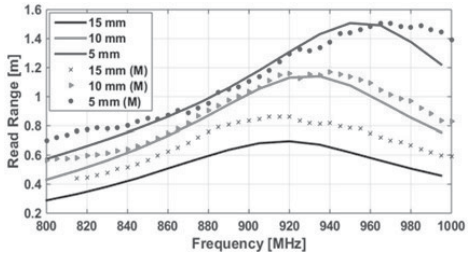

Fig. 6. Comparison between the simulated and measured read range at three different implant depths.

was recorded as P_{th}. With the measured output threshold power of the reference tag P_{th}^*, the system sensitivity constant Λ, and the emission power limit of the measurement system EIRP, the attainable read range of the tag versus frequency can be calculated by [12]

$$d_{\text{tag}} = \frac{\lambda}{4\pi}\sqrt{\frac{\text{EIRP}}{\Lambda}\frac{P_{\text{th}^*}}{P_{\text{th}}}}. \tag{3}$$

The head equivalent liquid made with water, sugar, and salt was used to mimic the human tissue environment in wireless measurement. Its relative permittivity and conductivity were confirmed with Agilent Technologies 85070E Dielectric Probe.

In the wireless measurement, the implant part was submerged in the liquid at three different implant depths: 5, 10, and 15 mm. Fig. 6 shows the comparison between the measured read range and the simulated read ranges from the homogeneous truncated cone model. A good match was found especially in 5 and 10 mm cases. In the 15 mm case, the measured read range was higher than the simulated one from the simulation.

A. Misalignments Test

In order to investigate the antenna system sensibility to the misalignment between the two parts, we also tested the read range with lateral and rotational misalignment between the wearable and implantable parts. In the lateral misalignment test, the wearable part was moved 5 mm from the central position to four different directions with the implant part fixed in the liquid.

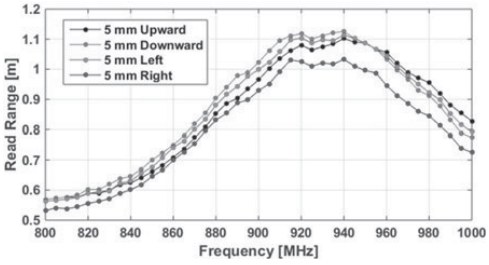

Fig. 7. Lateral misalignment test at 10 mm implant depth.

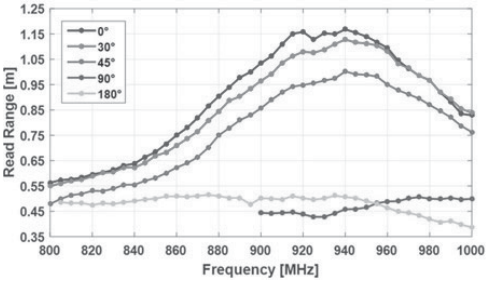

Fig. 8. Measured impact of rotational misalignment in the liquid phantom at 10 mm implant depth.

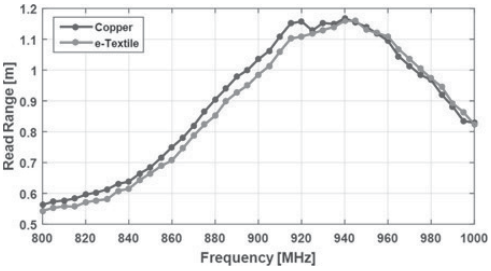

Fig. 9. Comparison of the measured read range of copper and conductive fabric wearable part at 10 mm implant depth.

In the rotational misalignment test, the wearable part was rotated clockwise from 0° to 180°, as shown by the arrow in Fig. 1. Fig. 7 shows the measured read range in the lateral misalignment test; in the four directions of the misalignment, the read range maintains at a very similar level with less than 0.1 m deviation compared with the nonmisalignment situation. Fig. 8 compares the read range with different rotational misalignments. The read range dropped with the increase of the rotational misalignment from 0° to 90°. When the misalignment angle was larger than 90°, the backscattered signal was too weak to be detected. However, a nearly 0.5 m read range was measured when the wearable part rotated 180° through the whole UHF band.

B. Conductive Textile

To improve the flexibility and durability of the wearable part, we fabricated also an e-textile version of it with less electromotive force Shieldit Super conductive textile featuring a sheet resistance less than 0.5 Ω/m^2 and EPDM as the substrate. According to the results from the wireless measurement in Fig. 9, the e-textile version has very similar performance compared with the copper one. This adds further assurance to the practical implementation where the user's comfort is a pertinent aspect.

IV. Conclusion

To face the challenge of establishing the radio link for the implantable wireless brain care application, we developed a spatially distributed passive UHF antenna system with an SRR-inspired implant part and an inductive coupled wearable part. By adopting the SRR topology, the implant part is downsized to $\pi \times 8.6^2 \times 1\,\text{mm}^3$ and the antenna impedance is complex-conjugate matched with the capacitive RFID IC without any matching components. In the wireless measurement with liquid mimicking human head environment, the prototyped antenna system was verified to provide up to 1.1 m backscattering read range at 10 mm implant depth even with moderate lateral or rotational misalignments between the implantable and wearable parts. Our future work will focus on integrating physiological sensors into the presented antenna system.

References

[1] M. O. Krucoff *et al.*, "Enhancing nervous system recovery through neurobiologics, neural interface training, and neurorehabilitation," *Front. Neurosci.*, vol. 10, Dec. 2016, Art. no. 584.

[2] L. Zhao, Q. Ye, K.-L. Wu, G. Chen, and W. Yu, "A new high-resolution electromagnetic human head model," *IEEE Antennas Propag. Mag.*, vol. 58, no. 5, pp. 32–42, Oct. 2016.

[3] S. Mustafa, A. M. Abbosh, and P. T. Nguyen, "Modeling human head tissues using fourth-order Debye model in convolution-based three-dimensional finite-difference time-domain," *IEEE Trans. Antennas Propag.*, vol. 62, no. 3, pp. 1354–1361, Mar. 2014.

[4] C. Liu *et al.*, "A review of implantable antennas for wireless biomedical devices," in *Proc. Forum Electromagn. Res. Methods Appl. Technol.*, 2016, pp. 1–11.

[5] S. Ma, L. Ukkonen, L. Sydänheimo, and T. Björninen, "Split ring resonator antenna system with implantable and wearable parts for far field readable backscattering implants," in *Proc. 2017 IEEE Int. Symp. Antennas Propag. USNC/URSI Nat. Radio Sci. Meeting*, San Diego, CA, USA, Jul. 2017, pp. 1689–1690.

[6] T. Björninen *et al.*, "Development and validation of an equivalent circuit model for UHF RFID IC based on wireless tag measurements," in *Proc. 34th Annu. Symp. Antenna Meas. Techn. Assoc.*, Bellevue, WA, USA, 2012, pp. 480–485.

[7] A. Drossos, V. Santomaa, and N. Kuster, "The dependence of electromagnetic energy absorption upon human head tissue composition in the frequency range of 300-3000 MHz," *IEEE Trans. Microw. Theory Techn.*, vol. 48, no. 11, pp. 1988–1995, Nov. 2000.

[8] A. N. Bashkatov *et al.*, "Glucose and mannitol diffusion in human dura mater," *Biophys. J.*, vol. 85, pp. 3310–3318, Nov. 2003.

[9] S. Gabriel *et al.*, "The dielectric properties of biological tissues: III. Parametric models for the dielectric spectrum of tissues," *Phys. Med. Biol.*, vol. 41, no. 11, pp. 2271–2293, Nov. 1996.

[10] IT'IS Foundation, "Tissue properties." [Online]. Available: https://www.itis.ethz.ch/virtual-population/tissue-properties/downloads.

[11] D. L. Means *et al.*, "Evaluating compliance with FCC guidelines for human exposure to radiofrequency electromagnetic fields," *Supplement C to OET Bulletin 65*, Federal Commun. Commission Office Eng. Technol., Washington, DC, USA, 1997.

[12] J. Virkki *et al.*, "The effects of recurrent stretching on the performance of electro-textile and screen-printed ultra-high-frequency radio-frequency identification tags," *Textile Res. J.*, vol. 85, no. 3, pp. 294–301, Aug. 2015.

PUBLICATION II

Double Split Rings as Extremely Small and Tuneable Antennas for Brain Implantable Wireless Medical Microsystems

Shubin Ma, Toni Björninen, Lauri Sydänheimo, Merja H. Voutilainen and Leena Ukkonen

IEEE Transactions on Antennas and Propagation, 2020, doi: 10.1109/TAP.2020.3016459.

Double Split Rings as Extremely Small and Tuneable Antennas for Brain Implantable Wireless Medical Microsystems

Shubin Ma, *Student Member, IEEE,* Toni Björninen, *Senior Member, IEEE*, Lauri Sydänheimo, *Member, IEEE,* Merja H. Voutilainen and Leena Ukkonen, *Member, IEEE*

***Abstract*— Wireless intracranial implantable microsystems are believed to potentially innovate the management of brain disorders and the treatment of neurological diseases. The fundamental challenge in the development of the wireless implantable system is the attainment of miniature antennas achieving adequately high efficiency for signalling and wireless power transfer in the presence of the dissipative intracranial tissues. Here we demonstrate and evaluate an effective approach that utilizes the coupled split rings to develop the miniature implantable antenna. With the proposed approach, the antenna size can be decreased to $\pi \times (3 \times 1.5) \times 1$ mm^3 which is less than 2 % of the operating wavelength at 915 MHz while the antenna maintains the gain of -25 dBi when placed 16 mm deep in the anatomical human head model. As a proof of concept, we developed RFID tags based on the proposed antenna and verified their performance with tissue mimicking liquid and in-vivo experiment with rats. The measured maximum read range of the tags reaches 0.7 m and 1.1 m when immersed 30 mm in the tissue mimicking liquid and implanted 6 mm in a rat's cranial cavity, respectively.**

***Index Terms*— Split ring antenna, implantable antenna, RFID**

I. Introduction

Progress in brain research has brought compelling approaches to managing neurological illnesses. In neurorehabilitation, bi-directional neural interfaces are enabling mind-control of prosthetics and assistive devices as well as versatile research platform [1]. Deep brain stimulators have become available for the management of movement disorders [2], such as tremors in Parkinson's disease. In the experimental neuroscience, optogenetic methods are providing a powerful new research tool [3] and advances have been made towards optoelectronics methods for potential local cerebral tissue oxygenation monitoring [4]. Apart from neurophysiological applications, new methods for the long-term monitoring of intracranial pressure (ICP) hold the potential for home monitoring for improving the safety of people predisposed to elevation of ICP [5-7] as well as become a research tool for cerebrospinal fluid (CSF) research [8]. In terms of medical technology, the enabling part for all systems involving long-term brain implantable devices are antennas that must be small and flexible enough to be cranially concealed and functional based on energy transmitted from an external source rather than relying on batteries. This technology will empower new means to research in in-vivo animal models and long-term implantable medical devices for humans alike.

A major challenge in the development of battery-free implantable microsystems is establishing an efficient and stable wireless link with the integrated implantable antenna. From the perspective of electromagnetics and wireless communications, human head is a complex dielectric environment comprising biological materials that are dispersive and characterized with relative permittivity and conductivity tens of times higher than materials present in regular electronics devices and wireless signal ambience. Often brain implants need to be placed under the skull, usually up to 20 mm for neural signal recording, or even several centimeters deep in the brain parenchyma for deep brain stimulation. The significant implant depth and the electromagnetic energy loss exerted by the biological tissue surrounding the implant antenna will notably limit the antenna's radiation efficiency and overall worsen the efficiency of the wireless communication link between the implant and outside-body devices. Moreover, the electrical size of an antenna sets a fundamental limit to its attainable electromagnetic performance. Commonly antennas occupying a spherical volume such that $ka \leq 0.5$, where $k = 2\pi/\lambda$ is the free-space wavenumber and a is the radius of the sphere circumscribing the maximum dimension of the antenna, are classified as electrically small. They tend to suffer from ailments arising from the small size, including narrow impedance bandwidth and limited radiation efficiency and gain [9]. In addition to energy dissipation, the body tissue types are dispersive media with decreasing and increasing trends in relative permittivity and conductivity versus frequency, respectively. Consequently, using the centimeter or even millimeter wave frequencies for decreasing the antenna's electrical size loses its efficacy and sub-GHz band provides the best size-performance balance for intracranial implantable wireless systems from the perspective of the overall link efficiency [10].

In the sub-GHz band with a wavelength of more than 30 cm, creating electrically small implantable antennas with a size less than one centimeter is demanding. Stacked microstrip patch antennas with high-permittivity substrate and superstrate are an extensively studied class of antennas for this purpose. The sub-GHz antennas [11-16] achieved a volume as small as $\pi \times (4.7)^2 \times 1.27$ mm^3. However, the maximum implant depth in these studies was less than 5 mm. Moreover, the multi-layer structure constrains the flexibility of the structure and increases the implant thickness. Apart from this approach, low-frequency inductive coupling has been used for linking implanted and wearable units [17]. Due to the low path loss of the magnetic field in the human tissue, this method effectively helps to improve the overall link efficiency and for instance an inductively coupled antenna system [18] obtained the wireless link power efficiency of 66% with an implant depth of 15 mm. The limitation of the inductive coupling is its relatively large antenna size, the sensitivity to the antenna misalignments and the short wireless link distance that prevents a direct off-body communications link. In terms of the antenna impedance matching, most of the proposed implantable antennas have been developed for 50 Ω system impedance, which is common in conventional radio-frequency electronic systems. However, the implantable microsystems with built-in rectifier for

Manuscript received May, 27, 2020; revised July 17, 2020; accepted July 20, 2020. This work was supported in part by the Academy of Finland and the Finnish Cultural Foundation.

S. Ma, T. Björninen, L. Sydänheimo and L. Ukkonen are with the Faculty of Medicine and Health Technology, Tampere University, Tampere, Finland (e-mail: {shubin.ma, toni.bjorninen, lauri.sydanheimo, leena.ukkonen}@tuni.fi).

M. H. Voutilainen is with the Institute of Biotechnology, University of Helsinki, Helsinki, Finland.

Color versions of one or more of the figures in this communication are available online at http://ieeexplore.ieee.org.

Digital Object Identifier 10.1109/TAP.2020.3016459

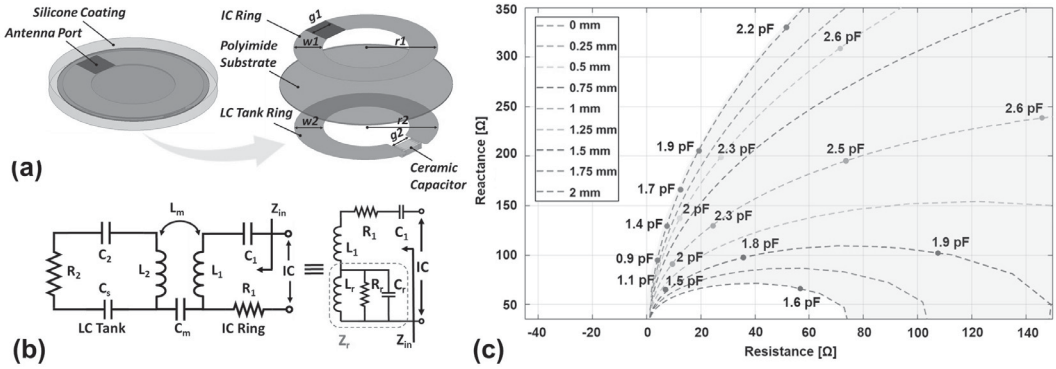

Fig. 1 Miniature far-field antenna formed by inductively coupled split rings. a, antenna structure and its geometrical parameters. b, Equivalent circuit model of the proposed antenna. c, Antenna input impedance with different $r_2 - r_1$ and C_s.

energy harvesting have inherent capacitive impedance with its value varying from different designs. Thus, antennas featuring a readily available impedance tunability to achieve good complex conjugate matching with these microsystems are favorable. Moreover, the electrically small antennas tend to have low resistance below 10 Ω. Thus, for these microsystems, antenna self-matching considering a non-50-Ω operating environment is a simpler and more viable approach. Inductively coupled structures have been proved to be an effective technique for antenna impedance matching. For example, inductively coupled coils or rings have been commonly used in near-field power transfer system to improve the system efficiency [19]. In the far field applications, inductively coupled loops have been utilized in RFID tag antenna development. For instance, the authors in [20] designed an inductively coupled coplanar loop antenna for wearable RFID tag; in [21], the authors proposed a wideband tag antenna with an inductively coupled meander split ring and the authors in [22] developed a patch antenna feed by an inductively coupled loop for metal-mount configuration.

In this paper, we demonstrate the development of a miniature far-field antenna composed solely of a pair of inductively coupled split rings for deep brain implants. The proposed antenna utilizes the inductive coupling between the two concentric rings and a lumped capacitor for antenna miniaturization and to obtain the inductive antenna input impedance that enables the conjugate impedance matching to capacitive microsystems. We will first describe the antenna configuration and conduct the parametric studies in the full wave electromagnetic solver to demonstrate the attainable antenna input impedance. With the anatomical human head model, we will show how to improve the antenna far-field performance by adjusting its placement inside the lossy tissue environment. Straight after, we will demonstrate the process of integrating the proposed antenna with an RFID microsystem. Then the prototyped antennas are tested in liquid phantom that simulates the tissue environment of the human head. Additionally, an in-vivo test in rat is carried out to verify the applicability of the proposed antenna in in-vivo animal studies.

II. Antenna Development

A. Antenna Configuration

The proposed antenna is developed based on a pair of coupled split rings. Fig. 1(a) shows its structure where the IC ring and LC tank ring are placed concentrically on top and bottom sides of the 50 μm thick polyamide (ε_r=2.25, tanδ=0.001 at 915 MHz) substrate, respectively. The antenna feed port is located at the terminals of the IC ring and a lumped capacitor is soldered to the terminals of the LC tank ring. The silicone coating (ε_r=4.4, tanδ=0.001 at 915 MHz) is used to protect the antenna from the exposure to the human tissues. The proposed antenna has 6 geometrical degrees of freedom including the ring outer radius $r_{1(2)}$, trace width $w_{1(2)}$, split gap width $g_{1(2)}$ with the subscript "1" and "2" denoting the IC ring and LC tank ring.

B. Antenna Input Impedance

Near the resonance frequency of the antenna, the inductive coupling between the two rings can be analyzed with the equivalent circuit shown in Fig. 1(b). Here the two rings are modeled as the series connection of the self-inductance $L_{1(2)}$, parasitic capacitance $C_{1(2)}$ and parasitic resistance $R_{1(2)}$ with the subscript "1" and "2" denoting the IC ring and LC tank ring, respectively. The capacitor at the LC tank ring terminals is modeled as the series lumped capacitor with the capacitance of C_s. The mutual inductance and mutual capacitance between the two rings are represented as L_m and C_m, respectively. According to [23], a mixed inductive and capacitive coupling of two resonators can be approximately equivalent to two coupled resonators that with a capacitive or inductive coupling only. Here we use the $L_m' = (k_m - k_e)L_m$ to represent the mixed coupling between the two rings with k_m and k_e being the inductive and capacitive coupling coefficients, respectively. The antenna input impedance is thus modelled using the reflected load theory [24] as,

$$Z_{in} = R_1 + j\omega L_1 + \frac{1}{j\omega C_1} + Z_r, \tag{1}$$

$$\text{where } Z_r = \frac{\omega^2 {L_m}'^2}{j\omega L_2 - \frac{j}{\omega}\left(\frac{1}{C_2} + \frac{1}{C_s}\right) + R_2}. \tag{2}$$

In eq. (1) and (2), except the capacitance of the lumped capacitor C_s, all the other parameters are determined by the geometrical dimensions of the two rings [25-28]. To facilitate the process of finding the relationship between the antenna geometry and the attainable antenna input impedance in the biological environment, we created an electromagnetic model of the antenna in the ANSYS High Frequency Structure Simulator (HFSS) and conducted parametric analysis where we varied the six dimensional parameters. In this initial analysis, the antenna was placed in the center of a tissue phantom (10 cm ×10 cm

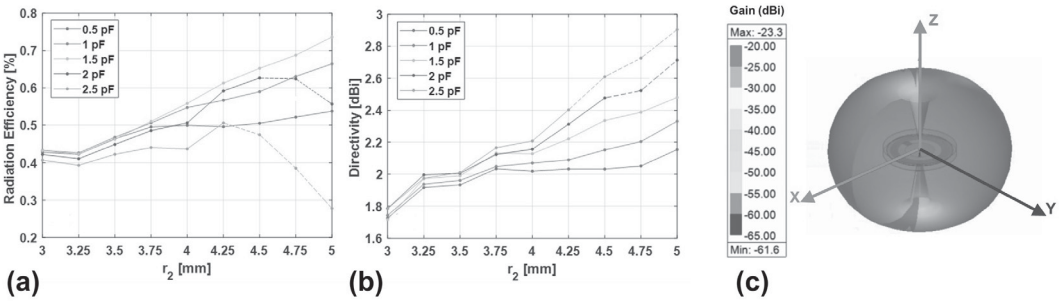

Fig. 2 Antenna radiation efficiency and far-field pattern in homogeneous tissue phantom. a, Simulated antenna radiation efficiency with different r_2 and C_s. b, Simulated antenna directivity with different r_2 and C_s. c, Simulated far-field radiation pattern with r_2 of 3 mm and the C_s of 1.9 pF at 915 MHz.

×10 cm) assigned with the frequency dependent dielectric properties (ε_r=45.74, σ=0.77 S/m at 915 MHz) suggested by U.S. FCC [29] for mimicking the intracranial environment.

Among the six geometrical parameters, the difference between the outer radius of the two rings and the capacitance of the lumped capacitor are found to have the dominant influence on the antenna input impedance. Keeping in mind the balance between the antenna miniaturization and the radiation efficiency, we fixed r_1 to 3 mm and gradually increased r_2 from 3 mm to 5 mm with a step of 0.25 mm. In each combination of r_1 and r_2, the capacitance of the lumped capacitor swept from 0.5 pF to 3 pF with a step of 0.1 pF. In this analysis, $w_{1(2)}$ and $g_{1(2)}$ were set to 1 mm to ease the prototype fabrication. Fig. 1(c) shows the results of the parametric analysis. In Fig. 1(c), each dashed line represents the range of the attainable antenna input impedance with certain value of the difference between r_1 and r_2 at 915 MHz. The increase in the difference between r_1 and r_2 decreases both the resistance and reactance of the antenna input impedance. For fixed values of r_1 and r_2, the capacitance of the lumped capacitor provides the flexibility for adjusting the antenna input impedance along the corresponding impedance line. For example, the dark blue line shows the range of the attainable antenna input impedance with r_2 equal to r_1. By increasing the capacitance of the lumped capacitor, the antenna input impedance increases along the dark blue line. Ideally, the shadowed area in Fig. 1(c) is the range of the attainable antenna input impedance at 915 MHz with difference combinations of r_1, r_2 and the capacitance of the capacitor. Here the wide tunable range of the impedance covers the typical values for achieving good complex conjugate impedance matching with most of the energy harvesting microsystems with a capacitive impedance.

C. Antenna Radiation Efficiency and Far-Field Pattern

Since the tuneable feature of the antenna impedance is realized by adjusting r_2 and C_s, it is worth studying how these parameters influence the antenna directivity and radiation efficiency. According to the results from the parametric analysis, with r_1 fixed to 3 mm, increase in r_2 improves the antenna radiation efficiency slightly. Fig. 2(a) compares the simulated antenna radiation efficiency in the tissue phantom with different r_2 and C_s. It is notable that the antenna input impedance becomes capacitive when r_2 is larger than 4.25 mm with C_s of 2.5 pF and r_2 larger than 4.5 mm with C_s of 2 pF. This explains the decrease of the dashed part of the purple and green lines. Since the capacitive antenna input impedance is out of our interest in this study, these dashed parts can be neglected.

Fig. 2(b) shows the relationship between r_2 and the antenna directivity. Similarly, a higher antenna directivity can be obtained with larger values of r_2. When r_2 is larger than 4 mm, the increase of C_s also has a noticeable positive impact on the antenna directivity.

Overall, the variation of r_2 and C_s have limited influence on antenna radiation efficiency and directivity, especially when r_2 and r_1 have similar values. This character ensures the safety to tune the antenna impedance without deteriorating the antenna gain.

Fig. 2(c) depicts the simulated far-field radiation pattern with r_2 of 3 mm and C_s of 1.9 pF at 915 MHz. In the homogeneous tissue phantom, the radiation pattern is omnidirectional with the main lobes in the direction parallel to the XOY plane and the minimum radiation in the positive and negative Z direction.

D. Antenna Implementation with RFID Microsystem

To evaluate the electromagnetic performance of the antenna in a more realistic numerical tissue phantom and to verify its performance in wireless measurements, we choose the NXP UCODE G2iL series RFID IC as the microsystem and adapted the antenna to form an implantable RFID tag (IC connected with the antenna). The selected IC has the turn-on power of 15.8 μW and the impedance of its RF input port is 12-j191 Ω at 915 MHz. This time, the HFSS anatomical male head model is adopted to mimic the intracranial environment. This model is composed of 15 individual tissue types and 58 separate tissue parts. The dielectric properties assigned to each tissue parts are obtained from the database provided by IT'IS foundation [30].

We initiated the antenna implementation by selecting the initial values of r_2 = 3 mm and the C_s = 1.9 pF. This selection is made according to Fig. 1(c) where the antenna input impedance with the selected r_2 and C_s is very close to the complex conjugate value of the IC impedance at 915 MHz. Then the antenna is placed horizontally in the cerebrospinal fluid layer in the anatomical model with an implant depth of 16 mm. In the simulation, the RFID IC was modelled with an equivalent circuit where capacitance and resistance of 0.91 pF and 2.85 kΩ, respectively, are connected in parallel [31]. For optimizing the combination of the r_2 and C_s that provides the best complex conjugate impedance matching between the antenna and the IC, we used the optimization tool in HFSS based on genetic algorithm. As a cost function for the numerical optimization algorithm, we used the power transfer efficiency τ given by

$$\tau = \frac{4\mathrm{Re}(Z_a)\mathrm{Re}(Z_{ic})}{|Z_a+Z_{ic}|^2}. \quad (3)$$

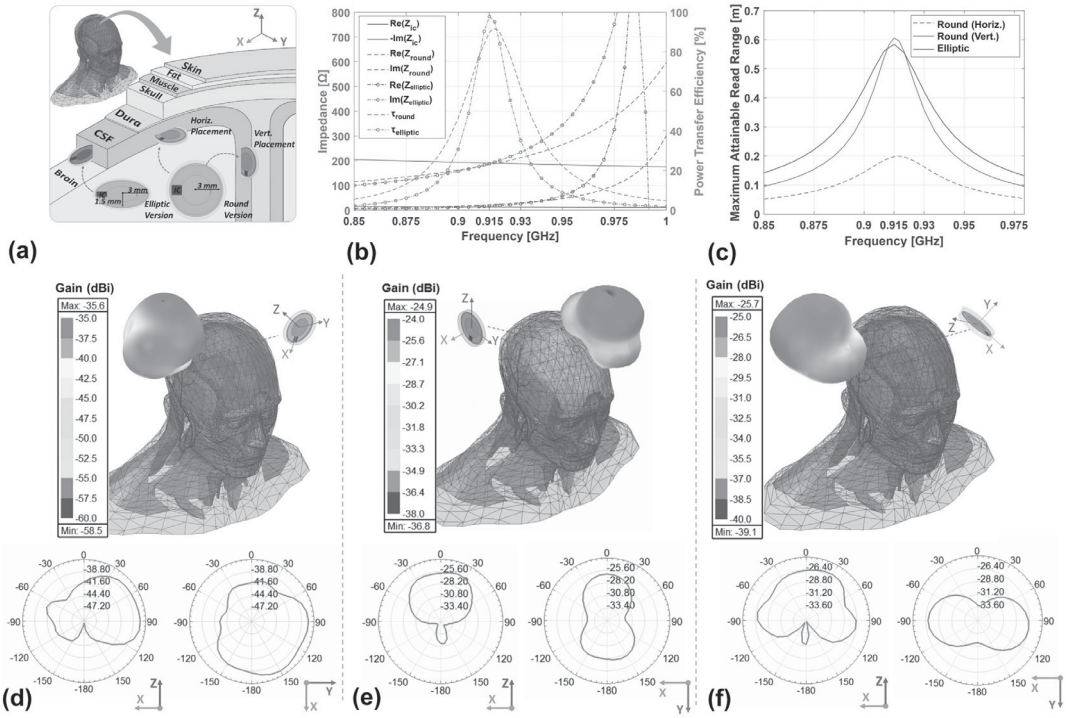

Fig. 3 Antenna implementation with RFID microsystem. a, RFID antennas with different placements in a simplified cross-sectional view of the anatomical head model. b, Comparison of the simulated antenna impedance and IC impedance. c, Comparison of the simulated maximum attainable read ranges of the antennas with different placements in the anatomical head model. d, Simulated radiation pattern of the round antenna with the horizontal placement in the anatomical head model. e, Simulated radiation pattern of the round antenna with the vertical placement in the anatomical head model. f, Simulated radiation pattern of the elliptic antenna with the vertical placement in the anatomical head model.

Here Z_a and Z_{ic} are the impedance of the antenna and the IC, respectively, and the value of τ indicates the fraction of power that is transferred from the antenna to the IC. The value $\tau = 1$ corresponds with the perfect power transfer that is achieved only with perfect complex conjugate impedance matching. As a result from the optimization process, we obtained the values $r_2 = 3$ mm and $C_s = 1.8$ pF. Fig. 3(b) compares the impedances of the IC (solid lines) and the obtained antenna (dash lines) in the anatomical model. A good complex conjugate impedance matching is achieved at 915 MHz with τ reaching 94 %.

Antenna gain with vertical and horizontal placements

In evaluation of the antenna gain, we found the antenna placement relative to the tissue boundaries significantly influenced the antenna radiation efficiency.

With a horizontal placement, as shown in Fig. 3(a), the corresponding antenna radiation efficiency and the maximum directivity are 0.01 % and 4.36 dBi, respectively. The corresponding maximum antenna gain is -35.6 dBi at 915 MHz. When the antenna is in vertical placement, where the antenna plane is perpendicular to the tissue boundaries, the antenna radiation efficiency improves to 0.13 %, which is more than 10 times higher than that in the horizontal placement. The maximum antenna gain reaches -24.9 dBi. The 2D and 3D radiation patterns in horizontal and vertical placements are illustrated in Fig. 3(d) and Fig. 3(e), respectively.

The change of the antenna placement leads to the rotation of the antenna main lobes (see Fig. 2(c)) and the incident angle of the radiated wave relative to the tissue boundaries. The reflection losses on the tissue boundaries is highly affected by this angle and the losses decrease to minimum when the main lobes are perpendicular to the boundaries [32]. Moreover, in the vertical placement, the main lobes of the antenna are pointing towards the tissues with a smaller thickness than that in the horizontal placement. The decreased tissue thickness leads to a lower tissue absorption loss. These two factors explain the higher radiation efficiency obtained in vertical placement.

It is also worth mentioning that the thickness of the CSF layer largely depends on the location of the head with a range from 1.3 mm to 8 mm [33-34]. With a radius of 3 mm, the thickness of the antenna in vertical placement reaches 6 mm and the only region that could host the antenna is near the longitudinal fissure. This location leads to a larger implant depth of 21 mm in the vertical placement. However, since the vertically placed antenna provides a higher radiation efficiency with an even larger depth than that in the horizontal placement, our prior conclusions remain intact. On the other hand, from the perspective of antenna applicability, it is necessary to further decrease the antenna size to release it from the limited implant sites on the head.

Elliptic version

To expand the antenna applicability, we developed an elliptic version based on the round one by assigning an aspect ratio of 0.5 to

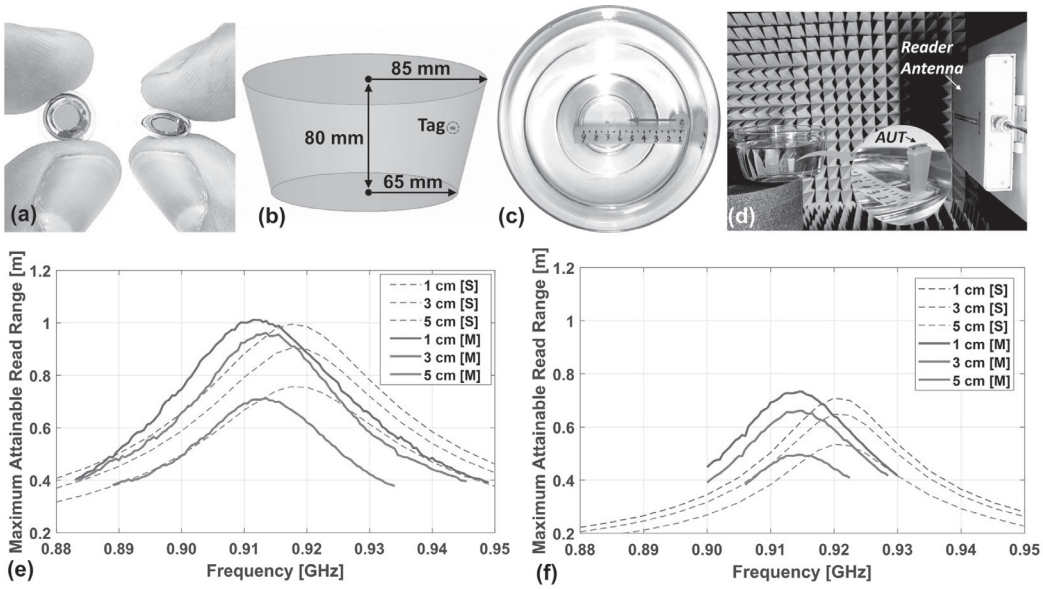

Fig. 4 Prototyped RFID tags and the wireless measurement with tissue mimicking liquid. a, Prototyped round tag (left) and elliptic tag (right). b, Homogenous liquid model with the tag in HFSS. c, Top view of the container filled with the tissue mimicking liquid with the elliptic tag placed on the stand. The stand is inserted into a sliding rail and can move horizontally (red arrow) in a controlled manner with the markers on the sliding rail. d, Measurement setup in the anechoic chamber. e, Comparison of the simulated and measured read ranges of the round tag with different horizontal depths in the liquid. f, Comparison of the simulated and measured read ranges of the elliptic tag with different horizontal depths in the liquid.

the two rings. By doing so, the vertical thickness of the elliptic version shown in Fig. 3(a) decreases to 3 mm. Since the relative size between the two rings maintains the same, we only need to adjust C_s to obtain the complex conjugate impedance matching to the IC. With the aid of the HFSS optimization tool, the optimal value of C_s to maximize τ is 3.9 pF. The impedance of the elliptic antenna is shown as the dot-dash lines in Fig. 3(b). The maximum τ is 98 % at 915 MHz. With an implant depth of 16 mm, the simulated radiation efficiency is 0.12 % and the maximum directivity is 3.4 dBi. The corresponding 2D and 3D radiation pattens are shown in Fig. 3(f) with a maximum value of -25.7 dBi. The antenna main lobe is pointing outwards the human head.

Read Range

In an RFID system, the read range of the tag (IC connected with the antenna) is the most convenient and intuitionistic indicator to evaluate the system performance. Due to the high sensitivity of the RFID readers (-70 to -80 dB), the maximum attainable read range of a tag is generally limited by the forward wireless link from the reader to the tag. The Friis' equation can be used to estimate the maximum attainable read range as

$$d_{tag}=\frac{\lambda}{4\pi}\sqrt{\frac{De_r\tau EIRP}{P_{ic0}}}. \quad (4)$$

In eq. (4), P_{ic0} is the turn-on power of the IC (-18 dBm), e_r and D are the radiation efficiency and directivity of the tag antenna, respectively and *EIRP* is the equivalent isotopically radiated power regulated by regional authorities (3.28 W in Europe and 4 W in the U.S.). We compare the estimated maximum attainable read ranges of IC with the developed antennas in Fig. 3(c). Due to the low radiation efficiency, the round version with an implant depth of 16 mm in horizontal placement has the shortest read range of 0.2 meter at 915 MHz. The elliptic version with 16 mm implant depth and round version with 21 mm implant depth in the vertical placement obtain approximately equal read range of 0.6 meter.

III. Prototyped Antennas and Wireless Measurement

A. Fabrication of the Antenna Prototypes

Fig. 4(a) shows the prototyped round (left) and elliptic (right) tags. The split rings of the antennas were patterned with 35 μm thick copper foil (σ = 58 MS/m) using the vinyl cutter (SummaCut D60, SUMMA NV, Belgium). The obtained copper rings were attached concentrically to the top and bottom sides of the 50 μm thick polyimide substrate (Kapton® 200HN, DuPont de Nemours, Inc., U.S.). The IC (UCODE G2iL, NXP Semiconductors, Netherlands) and the ceramic capacitor were soldered to the terminals of the IC ring and the LC tank ring, respectively. The 1 mm thick silicone coating (MED-2000, Avantor Inc., U.S.) was made to insulate the antenna from the tissue environment. This thickness is determined in balancing the overall antenna size and its insulation effect.

B. Wireless Measurement with Liquid Phantom

In the wireless measurement, we followed the FCC standard of the averaged brain properties (ε_r=45.74, σ=0.77 S/m at 915 MHz) and made the homogenous tissue mimicking liquid according to the recipe [35]. The prepared liquid was transferred into a plastic truncated cone container (lower radius: 6.5 cm, upper radius: 8.5 cm, height: 8 cm), which has a dimension comparable to that of the human head. Fig. 4(b) shows the container modelled in the HFSS. A plastic stand with the height of 2.5 cm was made to support the antenna in the liquid. To measure the antenna with different implant depths, we inserted the stand into a sliding rail. Fig. 4(c) shows the top view of the container

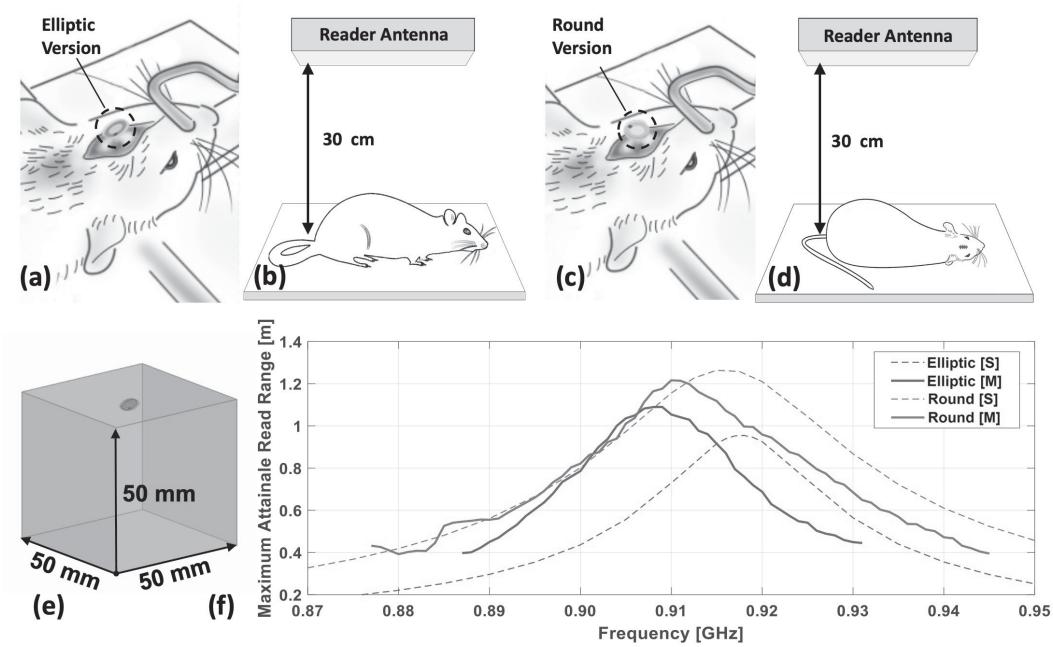

Fig. 5 In-vivo experiment of the prototyped RFID tags. a, The rat with the elliptic tag vertically implanted in the cranial cavity. b, Measurement setup of the rat with the implanted elliptic tag. c, The rat with the round tag horizontally implanted in the cranial cavity. d, Measurement setup of the rat with the implanted round tag. e. Homogeneous cubic phantom to mimic the rat's head in HFSS. f, Comparison of the simulated read ranges and measured ones of the two tags.

with the elliptic antenna placed on the stand. The stand can move horizontally in a controlled manner with the markers on the sliding rail. The markers in centimeter indicates the horizontal distance from the antenna to the container shell.

Fig. 4(d) shows the measurement setup in the anechoic chamber. We conducted the measurement with the Voyantic Tagformance® Pro RFID tester. Fig. 4(e) compares the simulated and measured read ranges of the round antenna. The measured results have a good agreement with the simulated ones with the read range of 1 m when the horizontal depth in the liquid is less than 3 cm. When the depth increases to 5 cm, the round antenna can still provide a read range of 0.7 m. Similarly, according to the result shown in Fig. 4(f), the elliptic antenna also has a good consistence between the measured and simulated read ranges. Due to its relatively lower radiation efficient compared with the round one, its read range drops to 0.7 m with a horizontal depth in the liquid less than 3 cm. With the 5 cm depth, the read range decreases to 0.5 m.

C. In-vivo Experiment of the Prototyped Antennas

To evaluate the applicability of the proposed antenna in in-vivo animal studies, we carried out the animal experiment in the accordance with the directive of the European Parliament and of the Council on the protection of animals used for scientific purposes (Directive 2010/63/EU of the European Parliament and of the Council). The experiment was approved by the National Animal Experiment Board of Finland (ESAVI/12830/2020).

A total of 2 adult male Wistar rats (weight: 250-270 g) were used in the experiment. The stereotaxic surgeries were performed under isoflurane anesthesia (4% during induction and 2.5% during maintenance). The rats were fixed on the stereotaxic frame with the skull exposed. The high-speed dental drill was used to make the hole on the rat skull. The elliptic and round tags were implanted vertically and horizontally underneath the skull of each rat, respectively. The implant depth for the elliptic and round ones was 6 mm and 3 mm, respectively. During the surgery, Lidocaine-adrenalin solution (10 mg/ml, Orion Pharma Oyj, Finland) was used to prevent bleeding. After the implantation, the burr hole was sealed with dental cement (Aqualox, Voco Cuxhaven GmbH, Germany) and the incisions were closed with suture.

We conducted the wireless measurement with the Voyantic Tagformance®. The measurement setup with the reader antenna is shown in Fig. 5(b, d). The reader antenna has a linear polarization with a gain of 8 dBi. The rats were fixed on a plastic table and the reader antenna was fixed with a vertical distance of 30 cm above the table.

Fig. 5(f) compares the measured and simulated read ranges of the two tags. For the elliptic tag, we measured the read range of the tag with the reader antenna orthogonal to the antenna's E plane, the maximum read range of 1.1 m is obtained. In the measurement with the round version, we placed the reader antenna in the maximum radiation direction of the implanted antenna by fixing the rat on the table with its right side down. According to the results shown in Fig. 5(f), the round tag has the maximum read range more than 1.2 m. In the simulation, we built a homogeneous cube (ε_r=45.74, σ=0.77 S/m at 915 MHz) with a side-length of 5 cm to mimic the rat's head. Fig. 5(e) shows the modeled phantom and the simulated results are shown in Fig. 5(f) with dashed lines. In comparison between the simulated and measured results, there are up to 0.1 m level shift and around 10 MHz peak frequency shift for the tested antennas. The reason of the shifts is mainly due to the computational inaccuracy of the homogenous phantom used to simulate the rat's head and the uncertainties (e.g. rat's blood and the cement in the implant spot) in the in-vivo experiment. Since the shifts are minor, we believe the

TABLE I
COMPARISON OF IMPLANTABLE ANTENNAS

Ref.	Year	Type	Frequency (MHz)	Dimension	Implant Depth	Dielectric Material	Maximum Gain	Stacking Layer	Short Pin	Features
[13]	2017	Patch	1900	$10.2 \times 4.2 \times 0.4$ mm^3	5 mm in head	Rogers 3010	-14.5 dBi	2	Yes	
[14]	2017	Patch	2450	$8.5 \times 8.5 \times 1.27$ mm^3	2 mm in skin	Rogers 3210	-17 dBi	2	No	CP
[11]	2018	Patch	915	$\pi \times (4.7)^2 \times 1.27$ mm^3	4 mm in skin	Rogers 3010	-32.8 dBi	2	Yes	CP
[12]	2018	Patch	2450	$10 \times 10 \times 0.4$ mm^3	4 mm in skin	Rogers 6010	-9 dBi	2	No	Wideband
[16]	2018	Patch	915, 2450	$8 \times 6 \times 0.5$ mm^3	4 mm in skin	Rogers 6010	-28.5 dBi	2	No	Dualband
[15]	2019	Patch	2450	$10 \times 10 \times 1$ mm^3	12 mm in CSF	Taconic RF-35	-25 dBi	3	No	
[36]	2014	PIFA	2450	$8 \times 4 \times 1.27$ mm^3	4 mm in skin	Rogers 3010	-10.7 dBi	2	Yes	
[37]	2015	PIFA	403	$12.5 \times 12.5 \times 1.27$ mm^3	18 mm in muscle	Rogers 3010	-32.49 dBi	2	Yes	
[38]	2019	PIFA	673	$10 \times 10 \times 3.2$ mm^3	50 mm in muscle	FR 4	-29.4 dBi	2	Yes	
[39]	2017	Loop	915	$\pi \times (12.5)^2 \times 3$ mm^3	11 mm in brain	Rogers 4003	N/A	No	No	
[40]	2019	Loop	403	$16 \times 16 \times 1$ mm^3	14 mm in CSF	FR 4	N/A	No	No	
[41]	2019	Loop	307 - 3500	$18 \times 18 \times 3$ mm^3	50 mm in stomach	Rogers 3010	-30 dBi	No	No	Wideband
This work	2020	Loop	915	$\pi \times (3 \times 1.5) \times 1$ mm^3	16 mm in CSF	Polyamide	-25.7 dBi	No	No	

simulation still provides the reference value in estimating the antenna performance.

A summary of state-of-the-art implantable antennas is shown in Table I. The multi-layer patch antenna and the planar inverted-F antenna (PIFA) are the most extensively studied antenna types for miniature implantable applications. High permittivity dielectric superstrate and substrate and short pin are common techniques to minimize the antenna footprint. The author of [11] decreased the size of a patch antenna to only 3% of the wavelength at the operation frequency with an applicable implant depth of 4 mm. In [36], the authors developed a PIFA based on a spiral radiation element and a folded ground. With such configuration, the antenna with a size less than one centimeter was obtained. In [39, 40], two miniature loop antennas were proposed and evaluated with the implant placed as deep as 14 mm in the brain tissue. In [41], a split ring loaded loop antenna was presented for capsule endoscopy with the implant placed 50 mm deep in the abdominal cavity. Through the above comparison, our proposed antenna shows its superiority in antenna footprint, implant depth and maximum antenna gain.

IV. CONCLUSION

We have reported an approach of utilizing solely coupled split rings to develop the miniature antenna for wireless deep intracranial implants. The antenna has a wide tunable range of the inductive impedance that covers the typical values for achieving good complex conjugate impedance matching with most of the energy harvesting microsystems. Based on the proposed approach, we developed two RFID tags operating at 915 MHz and having a volume as small as $\pi \times (3 \times 1.5) \times 1$ mm^3. In the simulation with the anatomical human head model, the developed tag has a maximum gain of -25.7 dBi and provides a read range of 0.6 m with an implant depth more than 16 mm in the CSF layer. The performance of the developed tags was verified through wireless tests in the tissue mimicking liquid where the tested tags provided the read range of more than 0.7 m with an immersed depth of 30 mm. In the in-vivo experiment, the prototyped tags have a read range of more than 1 m when implanted in the rat's cranial cavity. Considering its competitive performance in antenna miniaturization and radiation efficiency, we believe the proposed approach can play an important role in the development of implantable antennas for wireless intracranial sensors in brain care applications as well as in research in animal models.

REFERENCES

[1] A. Zhou *et al.*, "A wireless and artefact-free 128-channel neuromodulation device for closed-loop stimulation and recording in non-human primates," *Nat. Biomed. Eng.*, vol. 3, pp. 15–26, 2019.

[2] M. Kringelbach *et al.*, "Translational principles of deep brain stimulation," *Nat. Rev. Neurosci.*, vol. 8, pp. 623–635, 2007.

[3] P. Gutruf *et al.*, "Fully implantable optoelectronic systems for battery-free, multimodal operation in neuroscience research," *Nat. Electron.*, vol. 1, pp. 652–660, 2018.

[4] Z. Hao *et al.*, "Wireless, battery-free optoelectronic systems as subdermal implants for local tissue oximetry," *Sci. Adv.*, vol. 5, no.3, 2019.

[5] L. Y. Chen *et al.*, "Continuous wireless pressure monitoring and mapping with ultra-small passive sensors for health monitoring and critical care," *Nat. Commun.*, vol. 5, 2014.

[6] M. M. Ghanbari *et al.*, "An energy-efficient miniaturized intracranial pressure monitoring system," *IEEE J. Solid-State Circuits*, vol. 52, no. 3, pp. 720-734, 2017.

[7] Khan M. Waqas *et al.*, "Inductively powered pressure sensing system integrating a far-field data transmitter for monitoring of intracranial pressure," *IEEE Sensors J.*, vol. 17, no. 7, pp. 2191–2197, 2017.

[8] T. Binker *et al.*, "A new look at cerebrospinal fluid circulation," *Fluids and Barriers of the CNS*, vol. 11, 2014.

[9] C. A. Balanis, *Modern Antenna Handbook*, Hoboken, NJ, USA: Wiley, 2008.

[10] M. Zaeimbashi *et al.*, "NanoNeuroRFID: a wireless implantable device based on magnetoelectric antennas," *IEEE J. Electromagn., RF Microw. Med. Biol.*, vol.3, no. 3, pp. 206-215, 2019.

[11] C. Zhang *et al.*, "A wideband circularly polarized implantable antenna for 915 MHz ism-band biotelemetry devices," *IEEE Antennas Wireless Propag. Lett.*, vol.17, no. 8, pp. 1473-1477, 2018.

[12] S. Das and D. Mitra, "A compact wideband flexible implantable slot antenna design with enhanced gain," *IEEE Trans. Antennas and Propag.,* vol. 66, no. 8, pp. 4309-4314, 2018.

[13] Z. Chen *et al.*, "Maximum wireless power transfer to the implantable device in the radiative near field," *IEEE Antennas Wireless. Propag. Lett.*, vol. 16, pp. 1780-1783, 2017.

[14] X. Y. Liu *et al.*, "A miniaturized CSRR loaded wide-beamwidth circularly polarized implantable antenna for subcutaneous real-time glucose monitoring," *IEEE Antennas Wireless. Propag. Lett.*, vol. 16, pp. 577-580, 2017.

[15] B. Rana *et al.*, "An implantable antenna with broadside radiation for a brain–machine interface," *IEEE Sensors J.,* vol. 19, no. 20, pp. 9200-9205, 2019.

[16] S. A. A. Shah and H. Yoo, "Scalp-implantable antenna systems for intracranial pressure monitoring," *IEEE Trans. Antennas and Propag.*, vol. 66, no. 4, pp. 2170-2173, 2018.

[17] H. Kim *et al.*, "Review of near-field wireless power and communication for biomedical applications," *IEEE Access*, vol. 5, pp. 21264-21285, 2017.
[18] D. Jiang *et al.*, "An integrated passive phase-shift keying modulator for biomedical implants with power telemetry over a single inductive link," *IEEE Trans. Biomed. Circuits Syst*., vol. 11, no. 1, pp. 64-77, 2017.
[19] M. Kiani, U. Jow and M. Ghovanloo, "Design and optimization of a 3-coil inductive link for efficient wireless power transmission," *IEEE Trans. Biomed. Circuits Syst.*, vol. 5, no. 6, pp. 579-591, 2011.
[20] M. C. Tsai, C. W. Chiu, H. C. Wang, and T. F. Wu, "Inductively coupled loop antenna design for UHF RFID on-body applications," *Prog. Electromagn. Res.*, Vol. 143, 315-330, 2013.
[21] J. Wu, J. Li, X. Cui and L. Mao, "Circular loop antenna for UHF RFID tags with inductively coupled structure," *2011 Int. Conf. on Control, Autom. Syst. Eng. (CASE)*, Singapore, 2011, pp. 1-4, 2011.
[22] Mo, L. and Li, C., "Double loop inductive feed patch antenna design for antimetal UHF RFID tag," *Int. J. Antennas Propag.*, vol. 2019, pp.1-8, 2019.
[23] Hong, J., *Microstrip Filters For RF/Microwave Applications,* Second ed. Hoboken, NJ, USA: Wiley, 2011.
[24] K. Finkenzeller, *RFID-Handbook*, 2nd ed. Hoboken, NJ, USA: Wiley, 2003.
[25] S. S. Mohan *et al.*, "Simple accurate expressions for planar spiral inductances," *IEEE J. Solid-State Circuits*, vol. 34, pp. 1419–1424, 1999.
[26] L. W. Ritchey, "A survey and tutorial of dielectric materials used in the manufacture of printed circuit boards," *Proc. PCB Design Conf.,* pp. 1-10, 1999.
[27] R. Garg and I. J. Bahl, "Characteristics of coupled microstriplines," *IEEE Trans. Microw. Theory Tech.*, vol. 27, pp. 700–705, 1979.
[28] U. M. Jow and M. Ghovanloo, "Design and optimization of printed spiral coils for efficient transcutaneous inductive power transmission," *IEEE Trans. Biomed. Circuits Syst.*, vol. 1, no. 3, pp. 193–202, 2007.
[29] *Body Tissue Dielectric Parameters*, Federal Communications Commission. [Online]. Available: www.fcc.gov/general/body-tissue-dielectric-parameters
[30] *IT'IS Database for Thermal and Electromagnetic Parameters of Biological Tissues*, ver. 3.0., IT'IS Foundation, 2015. [Online]. Available: www.itis.ethz.ch/database
[31] T. Björninen *et al.*, "Development and validation of an equivalent circuit model for UHF RFID IC based on wireless tag measurements," *Proc. AMTA Symp.*, 2012.
[32] D. Nikolayev *et al.*, "Electromagnetic radiation efficiency of body-implanted devices," *Phys. Rev. Applied*, vol. 9, no. 2, pp. 24033-24045, 2018.
[33] V. O. Korhonen *et al.*, "Light propagation in NIR spectroscopy of the human brain," *IEEE J. Sel. Top. Quantum Electron.*, vol. 20, no. 2, pp. 289-298, 2014.
[34] F. B. Haeussinger *et al.*, "Simulation of near-infrared light absorption considering individual head and prefrontal cortex anatomy: implications for optical neuroimaging," *PLoS One*, vol. 6, 2011. Art. no. e26377.
[35] G. Hartsgrove *et al.*, "Simulated biological materials for electromagnetic radiation absorption studies," *Bioelectromagnetics*, vol. 8, pp. 29-36, 1987.
[36] C. Liu, Y. Guo, H. Sun and S. Xiao, "Design and safety considerations of an implantable rectenna for far-field wireless power transfer," *IEEE Trans. Antennas Propag*., vol. 62, no. 11, pp. 5798-5806, 2014.
[37] H. Li, Y. Guo, C. Liu, S. Xiao and L. Li, "A miniature-implantable antenna for medradio-band biomedical telemetry," *IEEE Antennas Wireless Propag. Lett.*, vol. 14, pp. 1176-1179, 2015.
[38] A. Abdi and H. Aliakbarian, "A miniaturized UHF-band rectenna for power transmission to deep-body implantable devices," *IEEE J. Transl. Eng. Health Med.*, vol. 7, pp. 1-11, 2019
[39] A. Sharma, E. Kampianakis and M. S. Reynolds, "A dual-band HF and UHF antenna system for implanted neural recording and stimulation devices," *IEEE Antennas Wireless Propag. Lett.*, vol. 16, pp. 493-496, 2017.
[40] M. Manoufali, K. Bialkowski, B. Mohammed, P. C. Mills and A. M. Abbosh, "Compact implantable antennas for cerebrospinal fluid monitoring," *IEEE Trans. Antennas Propag*., vol. 67, no. 8, pp. 4955-4967, 2019.
[41] Z. Jiang *et al.*, "Wideband loop antenna with split-ring resonators for wireless medical telemetry," *IEEE Antennas Wireless Propag. Lett.*, vol. 18, no. 7, pp. 1415-1419, 2019.

Shubin Ma received the B.E. degree in communication engineering from Xi'an University of Posts and Telecommunications, China, in 2011 and the M.Sc. (tech.) degree from Tampere University of Technology, Finland, in 2017.
He is currently pursuing the Ph.D. degree with the Faculty of Medicine and Health Technology at Tampere University. He has been a Visiting Scholar in Berkeley Wireless Research Center at UC Berkeley. His research interests include electromagnetic modelling, implantable and wearable antenna design, and implantable biomedical systems.

Toni Björninen received the M.Sc. and doctoral degrees in electrical engineering in 2009 and 2012, respectively, from Tampere University of Technology, Tampere, Finland.
He is currently Academy of Finland Research Fellow in Faculty of Medicine and Health Technology at Tampere University, Tampere, Finland. He has been a Visiting Postdoctoral Scholar in Berkeley Wireless Research Center at UC Berkeley and in Microwave and Antenna Institute in Electronic Engineering Department at Tsinghua University, Beijing. His research focuses on technology for wireless health including implantable and wearable antennas, wireless power transfer, sensors, and RFID-inspired wireless solutions.
Dr. Björninen is an author of 174 peer-reviewed scientific publications. He is Senior Member of IEEE and serves as Associate Editor in IEEE Journal of Radio Frequency Identification and Applied Computational Electromagnetics Society Journal. Previously, he has been a member of the editorial boards of IET Electronics Letters and International Journal of Antennas and Propagation.

Prof. Lauri Sydänheimo received the M.Sc. and Ph.D. degrees in electrical engineering from Tampere University of Technology, Tampere, Finland. He is currently a Professor with the Faculty of Medicine and Health Technology at Tampere University.
He has authored more than 200 publications in radio-frequency identification tag and reader antenna design and wireless system performance improvement. His current research interests include wireless data communication and wireless identification and sensing.

Prof. Merja H. Voutilainen received the M.Sc. and doctoral degrees in Pharmacology in 2004 and 2011, respectively, from University of Helsinki, Helsinki, Finland.
She is currently an adjunct professor in Pharmacology and Drug Development with the Institute of Biotechnology, University of Helsinki. Prof. Voutilainen leads the Regenerative Neuroscience research team that focuses on the preclinical research in ALS, Parkinson's disease and Huntington's disease.

Prof. Leena Ukkonen received M.Sc. and doctoral degrees in electrical engineering in 2003 and 2006, respectively, from Tampere University of Technology, Finland. Her Wireless Identification and Sensing Systems Research Lab at Tampere University, Faculty of Medicine and Health Technology concentrates on implantable and wearable biomedical sensors and wireless health technologies. Prof. Ukkonen has a wide research background and active international research collaboration networks in implantable sensors and design methods for wearable antennas and sensors. She has published over 360 peer-reviewed scientific articles. She is a member of IEEE and Associate Editor of IEEE Transactions on Antennas and Propagation.

PUBLICATION III

Robustness Evaluation of Split Ring Resonator Antenna System for Wireless Brain Care in Semi-Anatomical Ellipsoid Head Model

Shubin Ma, Lauri Sydänheimo, Toni Björninen and Leena Ukkonen

Journal of Applied Computational Electromagnetics Society, vol. 33, no. 9, pp. 966-972.

Robustness Evaluation of Split Ring Resonator Antenna System for Wireless Brain Care in Semi-Anatomical Ellipsoid Head Model

Shubin Ma, Leena Ukkonen, Lauri Sydänheimo, Toni Björninen

BioMediTech Institute and Faculty of Biomedical Sciences and Engineering
Tampere University of Technology
Tampere, Finland
{shubin.ma, leena.ukkonen, lauri.sydanheimo, toni.bjorninen}@tut.fi

Abstract ─ Robustness evaluation is a critical part to verify the applicability of wireless implantable devices. In this work, we present a semi-anatomical ellipsoid head model to evaluate the robustness of a split ring resonator inspired antenna system toward variable implant location, tissue layer thicknesses, and antenna orientation with respect to the human head. The system consists of a passive wearable part placed on the scalp and a cortical implant that carries a passive UHF RFID microsystem. According to our results, the antenna system is robust toward variability: it enables the remote powering of a −18 dBm RFID microsystem at distance between 0.5 and 1.1 meter at various locations and orientations with respect to the head and for skull thickness up to 1 cm.

Index Terms ─ Antennas, brain modelling, implantable biomedical devices, RFID, robustness.

I. INTRODUCTION

With more than 86 billion neurons and other supportive glial cells constituting the cerebrum, the brainstem and the cerebellum, the human brain forms the central nervous system that regulates all our daily physiological activities. Thus, any injury to the brain usually leads to serious deterioration of physical and mental capacity. In the pursue toward better life quality for those suffering from debilitating neurological conditions, researchers have recently found wireless brain care based on implantable sensors and stimulators a compelling approach to achieve a long term intracranial physiological monitoring, prosthesis controlling and treatment for neurological disorders [1-3].

Among the wireless modalities for the data transfer, modulated backscattering or RFID-inspired approaches are compelling as they offer low-power data communications that is pertinent to battery-free implants [4-6]. To establish effective far field communications with a cortical backscattering implant, we have recently proposed a spatially distributed split-ring resonator inspired antenna system composed of a small, thin and flexible implantable part that couples to a head-worn part acting as a performance booster [7]. Human body is an extremely complex operation environment for antennas, and thus computational electromagnetics and appropriate human body models are indispensable in the assessment of the electromagnetic performance of implantable and wearable antennas. In the aforementioned work, due to the difficulty of building a multiple-layer head phantom in practice, we used a simple homogenous block model to conduct the first feasibility evaluation of our antenna system and obtained a good agreement between the simulation and experimental results. That model included an average estimation for the dielectric properties of the human head, but due to its simplified geometry, it cannot be used to predict the impact of variation of the tissue layer thickness or radiation properties of the antenna system at different locations on the head or when its orientation with respect to the head changes. In practice, these are all crucial aspects, as the location of the implant varies according to the application and its exact orientation is hard to control during surgery. Thus, the antenna system must be robust toward these factors. It must also remain functional under anatomical variability since the tissue layer thicknesses are different for different individuals. Consequently, computational modelling of the human head with more details is pertinent to verify the applicability of the antenna system.

Currently, high-resolution medical imaging based computational models offer the most detailed structural information for computational modelling. However, for this reason they are not only computationally heavy, but reflect the anatomical details of a certain scanned individual with no possibility for adjusting the tissue layer thickness to assess the impact of anatomical variability. To overcome these limitations and to achieve holistic robustness evaluation of our system, we present modelling results obtained from a semi-anatomical human head model, which we have built by integrating a seven-layer ellipsoid with the anatomical head model of an adult male. Meanwhile, various electromagnetic CAD tools based on various numerical methods are available to provide extremely good accuracy [8]. In this journal, we chose Ansys HFSS 17.0 to conduct the simulation and analysis.

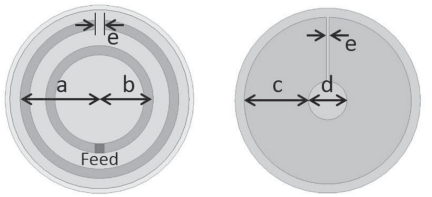

Geometrical parameter (mm)	a	b	c	d	e
	8.6	5.7	20.8	12.6	1.0

Fig. 1. Antenna system with its geometrical dimensions.

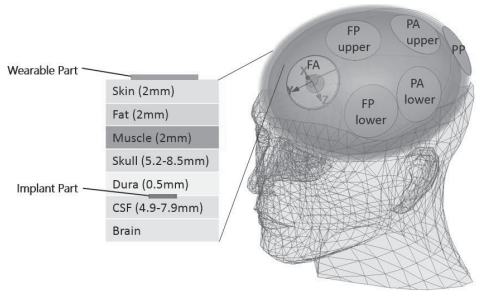

Fig. 2. Semi-anatomical human head model with the layered ellipsoid.

II. SIMULATION SETUP

A. Antenna System

The antenna system is based on the split ring resonator structure with an implantable and wearable parts. Fig. 1 shows the antenna structure and its geometrical dimensions. The implant part provides the self complex-conjugate matching with the IC that is connected to feed point in Fig. 1. The fully passive wearable part is for antenna gain improvement [7]. The cross-sectional view in Fig. 2 shows its implementation in intracranial environment. We assume the implant to be affixed to the dura, which is a tough fibrous membrane that forms the sack enclosing the subarachnoid space (SAS) and that wearable part is concentrically placed on the scalp. We use 35 μm thick copper as the conductor for the antenna system and the substrates for the wearable and implant parts are 2 mm thick EPDM (Ethylene-Propylene-Diene-Monomer) (ε_r=1.26, tanδ=0.007 at 915 MHz) and 50 μm thick flexible polyethylene (ε_r=2.25, tanδ=0.001 at 915 MHz), respectively. The coating material for the implant part is 1 mm thick silicone (ε_r=2.2, tanδ=0.007 at 915 MHz). The RFID microchip in the simulation is modelled by the parallel connection of the resistance and capacitance of 2.85 kΩ and 0.91 pF, respectively [9].

B. Antenna Performance Indicators

In the antenna development for passive RFID tags, the attainable read range (d_{tag}) between the tag and the off-body reader is one of the most important performance indicators. Friis' transmission equation can be used to estimate d_{tag} as

$$d_{tag}=\frac{\lambda}{4\pi}\sqrt{\frac{De_r\tau EIRP}{P_{ic0}}}, \qquad (1)$$

where the d_{tag} is in inverse proportion to RFID IC wake-up power (P_{ic0}) and proportional to antenna directivity (D), radiation efficiency (e_r), power transfer efficiency (τ), and the equivalent isotropically radiated power limitation ($EIRP$). The power transfer efficiency defined in (2) measures the portion of the power delivered from the antenna to the IC relative to the maximum power available from the antenna. It is given by

$$\tau=\frac{4\mathrm{Re}(Z_A)\mathrm{Re}(Z_c)}{|Z_A+Z_C|^2} \qquad (2)$$

where Z_A and Z_C are the antenna and IC impedances, respectively. In other words, $0<\tau\leq 1$ quantifies the goodness of the complex conjugate impedance matching between the antenna and the IC.

Among all the five variables shown in (1), except for P_{ic0} and $EIRP$, which are fixed by the IC design and the regional wireless communication regulatory committee, other parameters can be optimized to maximize d_{tag}. Therefore, in this work we will focus on the analysis of D, e_r and τ in the semi-anatomical human head model.

C. Semi-anatomical Head Model

We built the semi-anatomical human head model by integrating a seven-layer ellipsoid with the ANSYS anatomical human head model. The seven layers of the ellipsoid were constructed as ellipsoid shells with an adjustable thicknesses representing skin, fat, muscle, skull, dura, CSF (cerebrospinal fluid) and brain (grey matter). To model the relative permittivity and the electromagnetic energy dissipation in the biological matter, we used the four-term Cole-Cole relaxation model introduced in [10]. The loss model accounts for both loss sources: polarizability and ohmic loss due to conduction current. All the model parameters are available in [11] and Table 1 lists the dielectric

Table 1: Dielectric properties of human Tissues at 950 MHz.

Tissue	ε_r	σ (S/m)
Skin	41.405	0.867
Fat (not infiltrated)	5.462	0.051
Muscle	55.032	0.943
Skull (cancellous)	20.788	0.340
Dura	44.426	0.961
CSF	68.638	2.413
Brain (grey matter)	52.725	0.942

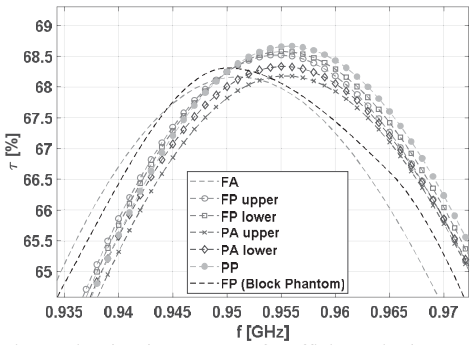

Fig. 3. Simulated power transfer efficiency in the semi-anatomical head model and the block phantom model.

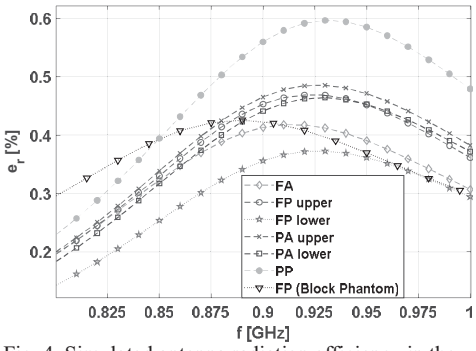

Fig. 4. Simulated antenna radiation efficiency in the semi-anatomical head model and the block phantom model.

properties of each tissue type at 950 MHz.

Fig. 2 illustrates the semi-anatomical head model and six different placements of the antenna system in four different regions: the frontal anterior (FA), frontal posterior (FP) with upper and lower positions, parietal anterior (PA) with upper and lower positons and parietal posterior (PP). At each location, we defined the nominal antenna orientation such that a line drawn through the middle of the split gap in the wearable part intersects the minor axis of the ellipsoid pointing along the person's height.

The thicknesses of skin, fat, and muscle tissue layers are almost independent of the positions on the head and thus we set a fixed value of 2 mm for each layer in this model [12]. The thickness of dura layer also varies over small range from 0.3 mm to 0.8 mm [13] and therefore we fixed the thickness of this layer to 0.5 mm. However, the thicknesses of the skull and the cerebrospinal fluid (CSF) layers vary greatly depending on the location. Hence, we measured these values over several cross-sectional slices of the anatomical head model to obtain averaged values. The thinner regions of the skull tend to coincide with wider SAS. Moreover, since we consider affixing the implant to the dura, the range for the skull thickness we present in Fig. 2 is the mean minimum thickness over the cross-sections, whereas the CSF layer thickness is the mean maximum SAS width. This selection was made, because we consider its benefit for both safety and wireless performance to maximize/minimize the distance between the implant and the cortex/wearable part.

Table 2: Tissue thickness in different location [mm]

Position / Tissue	FA	FP	PA	PP
Skin	2	2	2	2
Fat	2	2	2	2
Muscle	2	2	2	2
Skull	5.2	4.0	3.9	8.5
Dura	0.5	0.5	0.5	0.5
CSF	6.1	7.2	7.9	4.9

Table 2 lists the thickness of each tissue layer within the four regions we have considered in our model. In order to model the antenna at a specific region, we have assigned the corresponding layer thicknesses over the whole ellipsoid. However, since the separation between the implant and wearable part (and the material composition at this location) is dominant for the system's performance, we expect the thickness variations at other regions to have comparatively negligible impact on it.

III. RESULTS AND DISCUSSION

ANSYS HFSS uses the finite element method (FEM) to generate the electromagnetic field solutions. To obtain a high-level accuracy, the mesh size needs to be small enough. HFSS uses iterative process to refine the mesh by minimizing the change in the solution between consecutive iterations. In HFSS, the default parameter to evaluate the convergence of the solution of a problem with a single excitation port is the S-parameter magnitude. Typically, it converges before the far field parameters. Therefore, in this work, we monitored the expression cache of τ, D and e_r in each iteration to ensure the accuracy and reliability of the results. In the last iteration of the mesh refinement, all these parameters were changing less than 0.07%.

For comparison, we also modelled the antenna system in a seven-layer block phantom with a surface area of 30×30 cm^2. The layer thicknesses in the block phantom were identical to those in semi-anatomical model. Here the brain layer thickness was set to 7.5 cm so that the total thickness of the block was 25.2 cm. In our previous work, we have shown thorough experiments in liquid phantom [7] that the antenna system is robust toward moderately large rotational and translational misalignments between the wearable and implant parts [7] and thus we omit this analysis here.

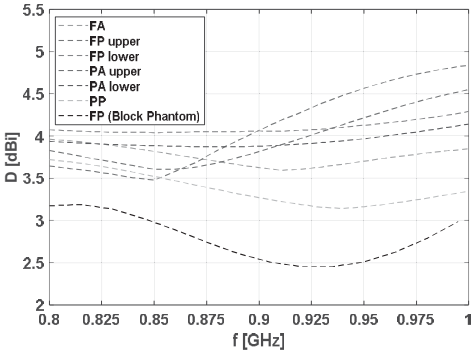

Fig. 5. Simulated antenna directivity in the semi-anatomical head model and the block phantom model.

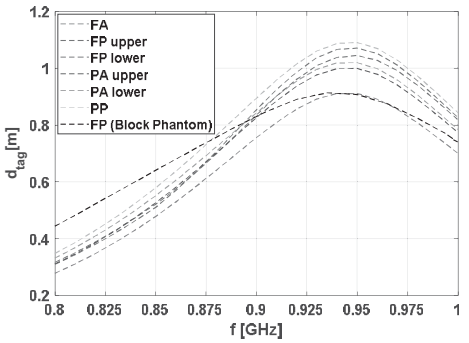

Fig. 6. Simulated maximum attainable read range in the semi-anatomical head model and the block phantom model.

A. Impact of Antenna Location

To facilitate the implementation of the wearable part on the curved surface of the ellipsoid, we flattened the contact surface between the two locally. However, since the curvature radius is large in comparison with the size of the wearable part, we expect this to introduce minimal impact on the results. In order to evaluate the impact of the antenna location on its electromagnetic performance judiciously, we first set the thickness for each layer of the head model to the values from the FP position. In this way, we can isolate the impact of the location (different curvature radii and impact of the anatomical part of the model) from the impact of variable tissue layer thicknesses. For comparison, we performed the same simulation in the layered block model with identical layer thicknesses.

Fig. 3 shows the simulated power transfer efficiency with different implant locations. The results verify that the implant position has negligible impact on τ. This is because only the dielectric properties of tissue types closest to the antenna are determinant for its impedance. For the same reason, the result from the block phantom, shown with the black dashed line, also matches closely with those from the semi-anatomical model. This implies that the simple block phantom model is adequate for initial antenna impedance tuning.

Fig. 4 shows the antenna radiation efficiency with different implant locations. The location causes a clear level shift in the radiation efficiency, but does not change its peak frequency. Generally, the highest efficiency occurs in PP region, with the peak value of 0.60% at 925 MHz. The lowest efficiency occurs in the FP region at the lower location with its maximum value of 0.38%. The result from the block phantom model lies close to the mean value of those from the semi-anatomical model, but there is a difference in the frequency of the peak value, which shifts to 880 MHz in the block model.

As shown in Fig. 5, the antenna directivity varies up to 1.5 dB between the different implant locations. In comparison, the block phantom model underestimates it over the whole frequency range. Overall, we conclude that although 1.5 dB maximum variation in D between the six locations is clearly noticeable, it is relatively smaller than that observed in the radiation efficiency (Fig. 4).

Fig. 6 shows the attainable read range computed from equation (1) with the simulated quantities from the

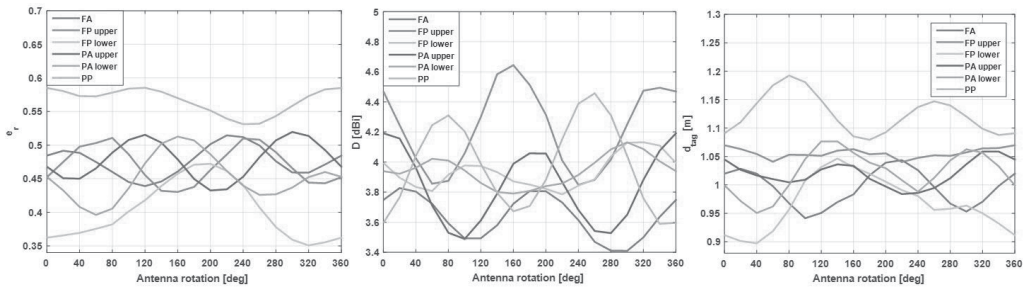

Fig. 7. Simulated results at six implant locations in the antenna rotation test

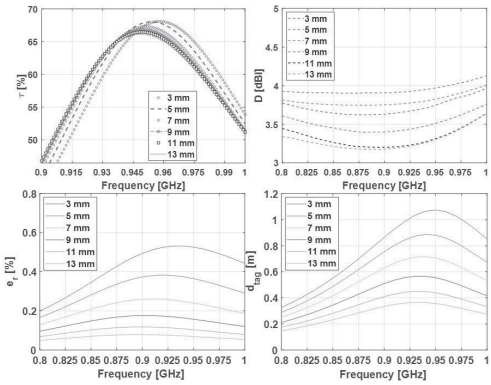

Fig. 8. Simulated results with the continuous change in the thickness of skull layer.

six locations and the block phantom. The peak value of d_{tag} varies from 0.9 m to 1.1 m around the frequency 930 MHz. Here the peak value of the result from the block phantom is close to the minimum of those from the semi-anatomical model.

In general, the implant location has relatively larger influence on D and e_r and very little impact on τ. Nonetheless, the antenna shows robustness toward the location in the semi-anatomical model: the peak value of attainable read range varies only ±10 cm around 1 meter with no shift in the center frequency of the peak value.

B. Impact of Antenna Orientation

Due to the structure limitation of the block phantom model, it cannot be expected to predict the correct relationship between the antenna orientation and its electromagnetic performance. This information is valuable for evaluating the antenna feasibility in the real implementation where the orientation of the implant part

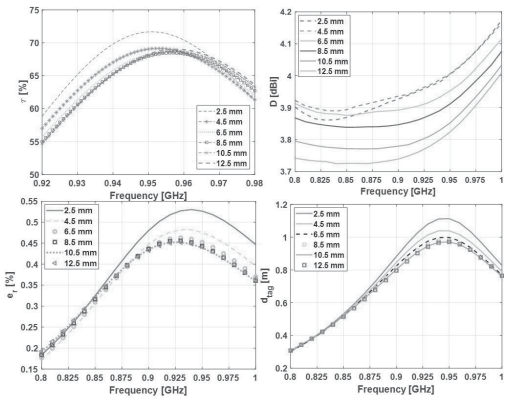

Fig. 9. Simulated results with the continuous change in the thickness of CSF layer.

is difficult to control. Therefore, we modelled the antenna system in the semi-anatomical model at the previously discussed six locations with a clockwise rotation around the x-axis with a step of 20 degrees at the frequency of 950 MHz. According to the simulated results shown in Fig. 7, the rotation of the antenna introduces a periodically varying fluctuating response in e_r and D versus the rotation angle, but overall the magnitude of the fluctuation remains below 10 %. Consequently, the attainable read range remains between 0.9 meter and 1.2 meters implying that the impact of the rotation is similar in magnitude as the impact of the location discussed above.

C. Impact of Variable CSF and Skull Thickness

To assess the impact of anatomical variability, we changed the thickness of the two most variable tissue layers; skull and CSF stepwise over intervals that cover the ranges shown in Fig. 2 and discussed in Section II.C. First, we set all the layer thickness to the values from the PA lower location (see Table II) and then increased the thickness of the skull from 3 mm to 13 mm with a step of 2 mm. According to the results shown in Fig. 8, D, e_r and d_{tag} decrease notably with the increase in the skull thickness. When the thickness is above 1 cm, the attainable read range drops below 0.5 m. The reason behind this is that the increase in the separation between the implant and wearable part weakens the electromagnetic coupling between the two.

A similar test was conducted for the CSF layer by changing its thickness from 2.5 mm to 12.5 mm with a step of 2 mm while the other layer thicknesses were fixed. Fig. 9 presents the simulated results. The decreasing trend in D with increasing layer thickness is similar to that observed in the case of the skull. However, overall the change is smaller. Likewise, the change in e_r versus the layer thickness shows similar character as in the case of skull thickness. However, here the separation (and therefore the coupling) between the implant and wearable parts remains constant and correspondingly the change in e_r is smaller and contributed to the increase in the amount of the high-conductivity CSF in the proximity of the antenna which increases the ohmic loss. Overall, the attainable read range remained at approximately 1 meter as the CSF layer thickness reached 12.5 mm.

VI. CONCLUSION

We evaluated the robustness of a spatially distributed implantable antenna system carrying an RFID microsystem toward several sources of variability that are likely to occur in practice. To achieve this, we used a semi-anatomical human head model based on a layered ellipsoid to mimic the human head environment with freely adjustable tissue layer thickness. The antenna system provided approximately consistent performance

at six different locations covering most of antenna placements on the head and insensitivity toward antenna orientation with respect to the head. Moreover, the attainable read range of the implanted RFID remained above 0.5 m with the thickness of the skull reaching 1 cm. These results ensure the feasibility of our antenna system as a wireless platform in brain care applications further.

Our ongoing and future work focuses on integrating physiological sensors into the evaluated antenna system and development of a wearable part that provides circular polarization.

ACKNOWLEDGMENT

This research was funded by Academy of Finland, Jane and Aatos Erkko Foundation.

REFERENCES

[1] Ryan M. Neely, David K. Piech, Samantha R. Santacruz, Michel M. Maharbiz and Jose M. Carmena, "Recent advances in neural dust: toward a neural interface platform," *Current Opin. Neurobiol.*, vol. 50, pp. 64–71, 2018.

[2] M. W. A. Khan, L. Sydänheimo, L. Ukkonen and T. Björninen, "Inductively powered pressure sensing system integrating a far-field data transmitter for monitoring of intracranial pressure," *IEEE Sensors J.*, vol. 17, no. 7, pp. 2191–2197, 2017.

[3] M. J. Cook, T. J. O'Brien, S. F. Berkovic et al., "Prediction of seizure likelihood with a long-term, implanted seizure advisory system in patients with drug-resistant epilepsy: A first-in-man study," *Lancet Neurol.*, vol. 12, no. 6, pp. 563–571, 2013.

[4] E. Kampianakis, A. Sharma, J. Arenas and M. S. Reynolds, "A dual-band wireless power transfer and backscatter communication approach for implantable neuroprosthetic devices," *2017 IEEE International Conference on RFID (RFID)*, Phoenix, AZ, 2017, pp. 67-72.

[5] C. W. L. Lee, A. Kiourti and J. L. Volakis, "Miniaturized fully passive brain implant for wireless neuropotential acquisition," *IEEE Antennas and Wireless Propagation Letters*, vol. 16, pp. 645-648, 2017.

[6] H. N. Schwerdt, F. A. Miranda and J. Chae, "Wireless fully passive multichannel recording of neuropotentials using photo-activated RF backscattering methods," *IEEE Transactions on Microwave Theory and Techniques*, vol. 63, no. 9, pp. 2965-2970, 2015.

[7] Shubin Ma, L. Ukkonen, L. Sydänheimo and T. Björninen, "Split ring resonator antenna system with implantable and wearable parts for far field readable backscattering implants," Proc. IEEE AP Soc. Intl. Symp. on Antennas and Propag., 2017, San Diego, CA, USA, pp. 1689–1690.

[8] Vandenbosch, G. A. E., "State-of-the-art in antenna software benchmarking: Are we there yet?" IEEE Antenna and Propagation Magazine, vol. 56, No. 4, August 2014.

[9] T. Björninen, L. Sydänheimo and L. Ukkonen, "Development and validation of an equivalent circuit model for UHF RFID IC based on wireless tag measurements," *AMTA Symp.*, 2012, Bellevue, WA, USA, pp. 6.

[10] S Gabriel, R W Lau and C Gabriel, "The dielectric properties of biological tissues: III. Parametric models for the dielectric spectrum of tissues," *Phys. Med. Biol.*, vol. 41, no. 11, pp. 2271–2293, 1996.

[11] IT'IS Foundation, Tissue Properties [Online]. Available: https://www.itis.ethz.ch/virtual-population/tissue-properties/downloads

[12] A. Drossos, V. Santomaa and N. Kuster, "The dependence of electromagnetic energy absorption upon human head tissue composition in the frequency range of 300-3000 MHz," *IEEE Trans. Microwave Theory Techn.*, vol. 48, no. 11, pp. 1988–1995, 2000.

[13] A. Bashkatov, E. Genina, Y. Sinichkin, V. Kochubey, N. Lakodina and V. Tuchin, "Glucose and mannitol diffusion in human dura Mater," *Biophysical J.*, vol. 85, no. 5, pp. 3310–3318, 2003

Shubin Ma received the B.E. degree in communication engineering from Xi'an University of Posts and Telecommunications, China, in 2011 and the M.Sc. (tech.) degree from Tampere University of Technology, Finland, in 2017.

He is currently pursuing the Ph.D. degree with the BioMediTech Institute and Faculty of Biomedical Science and Engineering at Tampere University of Technology. His research interests include electromagnetic modelling, antenna designs, and implantable biomedical systems.

Lauri Sydänheimo received the M.Sc. and Ph.D. degrees in electrical engineering from the Tampere University of Technology (TUT), Tampere, Finland. He is currently a Professor with the Faculty of Biomedical Sciences and Engineering, TUT.

He has authored more than 200 publications in radio-frequency identification tag and reader antenna design and wireless system performance improvement. His current research interests include wireless data communication and wireless identification and sensing.

Leena Ukkonen received the M.Sc. and Ph.D. degrees in electrical engineering from the Tampere University of Technology (TUT), Tampere, Finland, in 2003 and 2006, respectively.

She is currently a Professor and Academy Research Fellow with the Faculty of Biomedical Science and Engineering, TUT, Tampere, where she is leading the Wireless Identification and Sensing Systems Research Group.

Toni Björninen received the M.Sc. and doctoral degrees in Electrical Engineering in 2009 and 2012, respectively, from Tampere University of Technology (TUT), Tampere, Finland.

He is currently an Academy of Finland Research Fellow in BioMediTech Institute and Faculty of Biomedical Sciences and Engineering in TUT. He has been a Visiting Postdoctoral Scholar in Berkeley Wireless Research Center in UC Berkeley and in Microwave and Antenna Institute in Electronic Engineering Dept., Tsinghua University, Beijing. His research focuses on technology for wireless health including implantable and wearable antennas and sensors, and RFID-inspired wireless solutions.

Dr. Björninen is an author of more than 140 peer-reviewed scientific publications. He is a Senior Member of IEEE and serves as an Associate Editor in IET Electronics Letters and IEEE Journal of Radio Frequency Identification.

PUBLICATION IV

Inductively Coupled Split Ring Resonator as Small RFID Pressure Sensor for Biomedical Applications

Shubin Ma, Lauri Sydänheimo, Leena Ukkonen and Toni Björninen

2020 IEEE International Symposium on Antennas and Propagation and USNC-URSI Radio Science Meeting, Montréal, Québec, Canada, 2020.

PUBLICATION VI

Comparison of Human Head Phantoms with Different Complexities for Implantable Antenna Development

Shubin Ma, Toni Björninen, Lauri Sydänheimo and Leena Ukkonen

2018 International Applied Computational Electromagnetics Society Symposium - China (ACES), Beijing, China, 2018, pp. 1-2, doi: 10.23919/ACESS.2018.8669363.

Comparison of Human Head Phantoms with Different Complexities for Implantable Antenna Development

Shubin Ma, Leena Ukkonen, Lauri Sydänheimo, Toni Björninen
BioMediTech Institute and Faculty of Biomedical Sciences and Engineering
Tampere University of Technology
Tampere, Finland
{shubin.ma, leena.ukkonen, lauri.sydanheimo, toni.bjorninen}@tut.fi

***Abstract*— Human body phantom with electrical properties is widely used in electromagnetics solvers to model the lossy human tissue environment. The selection of the phantoms affects the computational efficiency and results accuracy. In this work, we evaluated four human head phantoms with an intracranial implantable antenna. Results of phantom complexity and antenna parameters are compared to provide the reference in phantom selection for implantable antenna development.**

Keywords*— implantable antenna, multilayer head phantom, anatomical head phantom.

I. Introduction

Implantable wireless devices play a significant role in the future telemedicine and remote vital-sign monitoring system, as they substitute the cable for in-to-out body wireless communication links. However, the inhomogeneous human tissues with high permittivity and notable conductivity bring the unpredictable degradation to the radio link in the proximity of it. The full-wave EM (electromagnetic) simulator is an effective tool to investigate this human tissue impact on EM performance of the implantable devices. In the simulator, human body phantom with tissue electrical properties is widely used to mimic the lossy tissue environment. In the literature, different approaches to constructing the phantom have been proposed, from the simple geometric shape based to the complex medical images based ones. With the increase of the phantom complexity, more details of the tissue geometrical information can be retained, but the consumption of computational resource raises in the EM simulator. Therefore, block phantom constructed based on the predominant human tissues are widely used to improve the computational efficiency. The main concern of using these simplified models is their lack of capability to reflect sufficient tissue characteristics from the perspective of EM wave propagation. This work aims to compare the reliability of a layered ellipsoid semi-anatomical human head model with the medical image based anatomical head model and a layered block model. The through-body radio link is established with a spatially distributed UHF RFID antenna developed from our previous work [1]. Fig.1 shows the head models and the implantable antenna with its geometrical dimensions.

II. Simulation Setup

A. Antenna System

The antenna system involved in the human model evaluation consists of a wearable and an implant parts. The implant part is assumed to be in contact with the CSF (cerebrospinal fluid) and that wearable part is concentrically placed on the scalp. The substrates for the wearable and implant parts are 2 mm thick EPDM (Ethylene-Propylene-Diene-Monomer) (ε_r=1.26, tanδ=0.007 at 915 MHz) and 50 μm thick flexible polyethylene (ε_r=2.25, tanδ=0.001 at 915 MHz), respectively. The coating material for the implant part is the 1 mm thick silicone (ε_r=2.2, tanδ=0.007 at 915 MHz). The RFID microchip in the simulation is modelled by the parallel connection of the resistance and capacitance of 2.85 kΩ and 0.91 pF, respectively. The antenna impedance is optimized to be complex-conjugate matched with the microchip in the CSF environment.

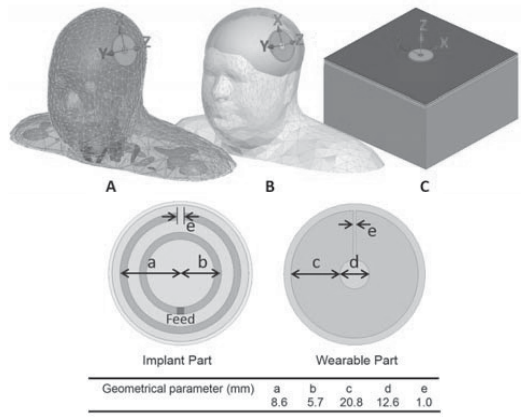

Geometrical parameter (mm)	a	b	c	d	e
	8.6	5.7	20.8	12.6	1.0

Fig. 1. Human head models and the implantable antenna with its geometrical dimensions

B. Antenna Performance Indicators

The attainable read range (d_{tag}) given in (1) is the main indicator to compare the system performance in different head models.

$$d_{tag}=\frac{\lambda}{4\pi}\sqrt{\frac{De_r\tau EIRP}{P_{ic0}}},\quad \text{where } \tau=\frac{4\mathrm{Re}(Z_A)\mathrm{Re}(Z_C)}{|Z_A+Z_C|^2} \tag{1}$$

The d_{tag} is in inverse proportion to RFID IC wake-up power (P_{ic0}) and proportional to antenna directivity (D), radiation efficiency (e_r), power transfer efficiency (τ), and the equivalent isotropically radiated power limitation ($EIRP$). The τ measures the portion of the power delivered from the antenna to the IC relative to the maximum power available from the antenna. In

other words, the factor $0<\tau\leq1$ quantifies the goodness of the complex conjugate impedance matching between the antenna and the IC. Obviously, the D, e_r and τ directly influence the d_{tag} and thus these antenna parameters will be respectively evaluated in the simulation.

C. Human Head Models

The anatomical head model shown in Fig.1 (A) is derived from the open source cryosection image based VHP-female model [2]. This head model has 15 individual tissues and 58 separate tissue parts. The semi-anatomical model illustrated in Fig.1 (B) is built by integrating a seven-layer ellipsoid to replace the cranial cavity of the VHP model. Its layered structure was constructed as ellipsoid shells with an adjustable thickness representing skin, fat, muscle, skull, CSF (cerebrospinal fluid) and brain (grey matter). The thickness of each layer is assigned with the corresponding tissue thickness measured from the implant location of the VHP model. The total distance between the antenna implant part and wearable part is 14 mm. Fig.1 (C) depicts the block model with a dimension of 30 mm × 30 mm × 20 mm. It has the identical 6-layer structure as that of the ellipsoid one but all the layers are in a flat form. The electrical properties assigned to each tissue in these models are obtained from IT'IS foundation. Additionally, to investigate the impact of the subsidiary tissues on the antenna EM performance, we reduced the VHP model to a simplified version with only six major tissue types: skin, fat, muscle, skull, CSF and brain.

III. Results and Discussion

We used finite element method based EM solver ANSYS HFSS v17 to compare the performance of each head model. The PC performed the simulations is equipped with Intel i7 X990 at 3.47 GHz with 24 GB of RAM. We monitored the convergence of the solution in each model in terms of the change in the parameters shown in Fig. 2 versus the mesh iterations. At the sixth iteration, the change in τ, e_r, and D had reduced to the maximum of 0.01%, 0.14% and 0.13%, respectively in all models and we considered these sufficient criteria for convergence. Table 1 lists the number of solved elements and the simulation time (mesh creation and solving 15 frequency points) in the different models. The time consumed in the VHP model with full tissue types is more than six times as that in the ellipsoid and block model. It is also noticeable that the simplification of the VHP model prominently reduces the model complexity and the time consumption.

Fig. 2 shows the simulated τ, e_r, D and d_{tag} in the four head models. The VHP model with full tissue types is considered as the reference model in aid of evaluating the other three models. All the antenna far field parameters are calculated in the positive Z direction as denoted in Fig.1. According to Fig. 2(A), both the ellipsoid and block models have a detuning of the peak frequency from 925 MHz to 942MHz. Conversely, the simplified VHP model has a negligible impact on τ. In terms of the e_r, as shown in Fig.2 (B), the block model has the worst performance with not only a peak frequency shift but also a clear 50% level underestimation, whereas, the ellipsoid model accurately estimates the peak frequency with less than 10% overestimation of the efficiency level. In the comparison of D shown in Fig.2 (C), the block model again fails to reflect its variation versus the frequency and a 1.5 dB level shift can be observed. The ellipsoid model, on the other hand, successfully characterizes the variation of D along with the frequency and level underestimation is less than 0.5 dB. Finally, d_{tag} simulated in the four models are shown in Fig.2 (D). Here the block model shows fair agreement with the others, but it should be noted that this agreement is only because of its poor predictions of e_r and D compensating each other in the computation of d_{tag}. The ellipsoid model shows a minor frequency detuning and level shift in d_{tag} compared with the VHP model, but provides a notable factor of 86% reduction in the simulation time. Simplified VHP model provides minimal deviation from VHP model and reduction by a factor of 63% in simulation time.

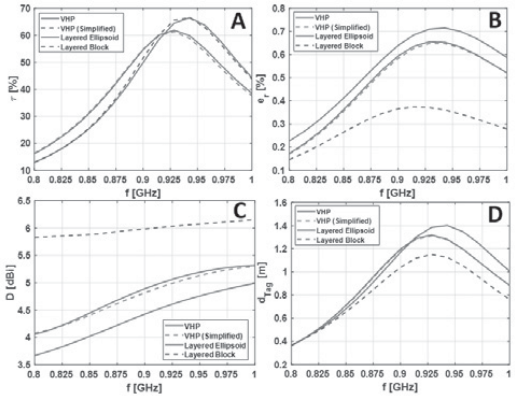

Fig. 2. Comparison of simulated τ, e_r, D and d_{tag} of the four models.

IV. Conclusion

We compared four human head models for simulating an antenna system composed of an intracranial implant and head-worn parts. Our results show that antenna impedance can be estimated with a layered block model, but it fails to predict the antenna radiation field appropriately. A layered ellipsoid model predicts very similar impedance and estimates the far field parameters sufficiently well without increasing the simulation time. The two anatomical models: VHP and VHP (simplified) predict virtually the same antenna parameters that are also very close to those obtained from the ellipsoid model. Overall, the results support using the ellipsoid model for initial antenna optimization and robustness studies where the layer thicknesses are variable and the VHP (simplified) for final verifications.

TABLE I
Solved Elements and Time Consumption of Each Model

Model	Solved Elements	Time (min)
VHP	343,007	221
VHP (Simplified)	192,605	80
Layered Ellipsoid	130,497	29
Layered Block	143,958	33

References

[1] S. Ma *et al*., "Split ring resonator antenna system with implantable and wearable parts for far field readable backscattering implants," in Proc. IEEE AP-S Symp., 9–15 July 2017, San Diego, CA, USA, pp. 1689–1690.

[2] J. Yanamadala *et al*., "Multi-purpose VHP-female version 3.0 cross-platform computational human model," 2016 10th EuCAP, Davos, 2016, pp. 1-5

PUBLICATION VII

Dual-Layer Circularly Polarized Split Ring Resonator Inspired Antenna for Wearable UHF RFID Tag

Shubin Ma, Leena Ukkonen, Lauri Sydänheimo
and Toni Björninen

2018 IEEE International Symposium on Antennas and Propagation & USNC/URSI National Radio Science Meeting, Boston, MA, 2018, pp. 683-684,
doi: 10.1109/APUSNCURSINRSM.2018.8609075.

Dual-Layer Circularly Polarized Split Ring Resonator Inspired Antenna for Wearable UHF RFID Tag

Shubin Ma, Leena Ukkonen, Lauri Sydänheimo, Toni Björninen
BioMediTech Institute and Faculty of Biomedical Sciences and Engineering
Tampere University of Technology
Tampere, Finland
{shubin.ma, leena.ukkonen, lauri.sydanheimo, toni.bjorninen}@tut.fi

***Abstract*—We present a circularly polarized antenna for wearable passive UHF RFID tag. The antenna consists of two layers without a physical connection. The upper layer is for achieving circular polarization by two orthogonal meandering dipoles connected to a split ring. The lower layer is a split ring resonator structure to achieve complex conjugate impedance matching with the RFID IC. The antenna has the maximum dimension of $\pi \times 22^2 \times 3$ mm^3 and it provided a 3-dB axial-ratio bandwidth of 23 MHz (905-928 MHz) in the simulation. The estimated maximum attainable read range of the tag exceeds two metres.**

Keywords—Circular polarization; crossed dipole; radio frequency identification; wearable antenna.

I. Introduction

The enormous growth of the wireless body area network (WBAN) has catalyzed the development of wearable devices. Meanwhile, the RFID technology enables the wearable devices to be lightweight, battery-less and cost-effective by energy self-harvesting through the electromagnetic wave received by the wearable antenna. For this reason, its antenna system has the substantial role in the overall RFID system performance.

Antenna polarization is one of the factors significantly influences the RFID system performance. In most RFID systems, the reader antennas with a circular polarization (CP) are used in communication with the common dipole or microstrip based linearly polarized RFID tags. Nevertheless, the circularly polarized tag antenna is still preferred due to the fact that they will improve the polarization match with the reader antenna and thus enhance the attainable read range. Needless to say, the circularly polarized tag antenna will largely increase the polarization flexibility when a linearly polarized reader antenna is used.

In our previous work [1], we proposed a spatially distributed split ring resonator (SRR) inspired UHF RFID antenna system, where the SRR was verified to provide the convenience for complex conjugate impedance matching between the antenna and the RFID IC, additionally a fully passive concentrically-placed gain-enhancing split ring was introduced to improve the antenna performance. In our wireless measurements, we observed that the antenna system had a linear polarization in the direction perpendicular to the direction of the gain-enhance ring split. Furthermore, the rotation of the gain-enhance ring will lead to the change of the polarization direction. Inspired by this relationship between the antenna polarization and the topology of the gain-enhancing ring, in this work, we apply the CP to the aforementioned antenna system by connecting the gain-enhancing ring to two orthogonal meandering dipoles.

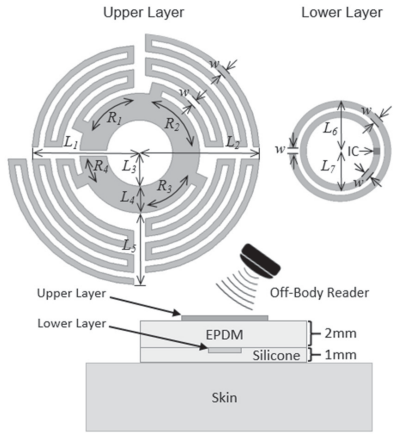

Fig. 1. Geometry of the proposed tag antenna and the cross-sectional view of its wearable implementation.

II. Antenna Geometry and Development

Fig. 1 shows the geometry and the cross-sectional view of the tag antenna in the wearable configuration. This antenna has two spatially concentrically distributed layers, which are respectively built on the upper and lower surfaces of the 2 mm thick EPDM (Ethylene-Propylene-Diene-Monomer) with a dielectric constant of 1.26 and a loss tangent of 0.001 at 915 MHz. To protect the antenna away from the direct contact with human tissue, the lower layer of the antenna is coated with 1 mm thick silicone with a dielectric constant of 2.2 and a loss tangent of 0.007 at 915 MHz.

The upper layer of the tag antenna is fully passive with two orthogonal meandering dipoles having different length and connection points to a split ring. To obtain a good CP, the length and the connection points were chosen so that the two dipoles could resonate at the same frequency but with a 90° phase

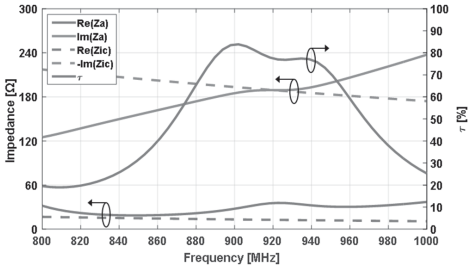

Fig. 2. Simulated power transfer efficiency and the impedance of the antenna and IC.

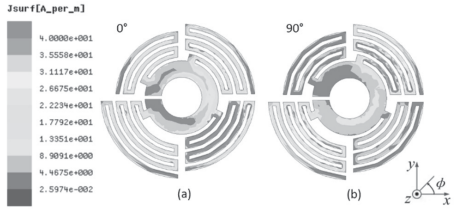

Fig. 3. Simulated current distribution of the upper layer from the antenna at 915 MHz with two phase angles (a) 0° and (b) 90°.

difference between each other [2]. The lower layer is developed based on the SRR structure to achieve the antenna impedance matching with the RFID IC by connecting the IC to the split of its inner ring. Since the SRR structure has the inductive impedance under its self-resonance frequency, the complex conjugate impedance matching with an IC typically with a capacitive impedance can be obtained without additional matching components. This tag antenna is developed to incorporate the NXP UCODE G2iL series RFID IC with a wake-up power threshold of 15.8 μW and its impedance at 915 MHz is 12 + j190 Ω. The optimized antenna geometrical parameters are derived from the Ansoft High-Frequency Structure Simulator (HFSS) as follows: R_1 = 75°, R_2 = 85°, R_3 = 75°, R_4 = 25°, L_1 = 18 mm, L_2 = 20 mm, L_3 = 5.5 mm, L_4 = 4.5 mm, L_5 = 12 mm, L_6 = 8 mm, L_7 = 6.3 mm, w = 1 mm.

III. Simulated Results

The antenna was simulated in the full-wave EM field solver - HFSS V15.0 where a skin box with the volume 300 × 300 × 20 mm^3 was made to mimic the human tissue environment and the IC was simulated as a parallel connection of capacitance and resistance of 0.91 pF and 2.85 kΩ. Fig. 2 shows the simulated impedance of the antenna and IC. The power transfer efficiency τ is to measure the complex conjugate impedance matching between the antenna and the IC. It is given by

$$\tau = \frac{4\mathrm{Re}(Z_A)\mathrm{Re}(Z_c)}{|Z_A+Z_C|^2} \quad (1)$$

where Z_A is the antenna impedance and Z_C is IC impedance. A good matching is obtained in the UHF band and τ reaches 80%

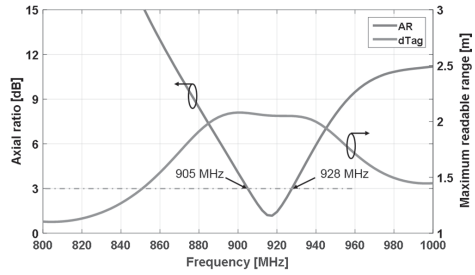

Fig. 4. Simulated axial ratio and the maximum readable range.

at 915 MHz. Fig. 3 shows the simulated current distribution of the upper layer from the antenna at 915 MHz. The currents are mainly distributed on the dipole along φ = 135° at a phase of 0° and when the phase changes to 90°, the currents concentrate mostly on the dipole along φ = 45°. This arrangement excites the LHCP in the region outside human tissue and as shown with the blue line in Fig. 4, the axial ratio (AR) reaches 1.1 dB at 915 MHz. The attainable read range d_{tag} defined in (2) is the most important parameter to evaluate the performance of RFID system,

$$d_{tag} = \frac{\lambda}{4\pi}\sqrt{\frac{De_r\tau EIRP}{P_{ic0}}} \quad (2)$$

where D is the antenna directivity, e_r is the radiation efficiency, P_{ic0} is the RFID IC wake-up power threshold and we assume that the reader antenna is polarization matched with the tag. With the $EIRP$ limited to 3.28 W and the simulated D = 3.1 dBi and e_r = 2.2% at 915 MHz, the d_{tag} can be estimated as depicted with the red line in Fig. 4. Overall, the proposed antenna is capable to provide 2 metres read range in the wearable configuration.

IV. Conclusion

A dual-layer wearable CP RFID tag antenna has been proposed in this paper. A novel approach has been used to obtain the CP configuration with a very small tag footprint. The dual layer structure where the IC embedded in silicone improves the tag durability and robustness especially in harsh environments. According to the simulation results, the tag antenna has good CP performance with a 23 MHz (905-928 MHz) 3-dB AR bandwidth in the UHF band, meanwhile the maximum read range reaches 2 metres. As a next step, we will test the tag in a wearable configuration and proceed to investigate an implantable configuration where the lower layer is implanted in human tissue for biomedical sensor applications.

References

[1] S. Ma *et al*., "Split ring resonator antenna system with implantable and wearable parts for far field readable backscattering implants," in Proc. IEEE AP-S Symp., 9–15 July 2017, San Diego, CA, USA, pp. 1689–1690.

[2] M. F. Bolster, "A newtype of circular polarizer using crossed dipoles," IEEE Trans. Microw. Theory Techn., vol. 9, no. 5, pp. 385–388, Sep. 1961.